Electric Traction Machine Design for Heavy Hybrid Vehicles

Rasmus Andersson

LUND UNIVERSITY

Licentiate Thesis
Div. Industrial Electrical Engineering and Automation
Department of Biomedical Engineering

2014

Div. Industrial Electrical Engineering and Automation
Department of Biomedical Engineering
Faculty of Engineering
Lund University
Box 118
221 00 LUND
SWEDEN

http://www.iea.lth.se

ISBN: 978-91-88934-66-6
CODEN: LUTEDX/(TEIE-1074)/1-121/(2014)

Printed in Sweden by Tryckeriet i E-huset
Lund University
Lund 2015

The more you learn, the more you realize how little you know about it

Abstract

The capability of a hybrid electric vehicle (HEV) to reduce the overall fuel consumption is proven in many different cases during the recent years. This is especially true in driving situations facing multiple retardations and take offs, such as city driving. A number of typical examples in the heavy vehicle segment are city buses, together with distribution- and refuse trucks. A difficulty with introducing a hybridised drivetrain, in particularly affecting the truck applications, is related to the commercial aspect. The increased investment cost must not be higher than the potential savings in fuel. One way to reduce the investment cost is to reduce the component size and thereby material cost in the bill of material. The objective in this thesis is to do so, with focus on the electric traction machine.

The thesis covers the electromagnetic design process in a 2D finite element environment, the prototype build as well as experimental evaluation of a permanent magnet synchronous machine (PMSM) for hybrid electric commercial heavy vehicle applications. The goals for the machine design are to fulfil given mechanical, thermal and electrical specifications, including a wide constant power range and an overload capability, all to be realized in the strictly limited space in the vehicle.

The specifications of requirements are set through a number of pre studies looking at different drive cycles and parallel hybrid concepts. These are mainly evaluated from a packaging point of view but also in terms of recuperating energy during vehicle decelerations. The result is used as input for the electric machine design work. The power levels are determined using an existing Simulink model of a parallel hybrid electric

vehicle. Different drive cycles and vehicle weights are used in order to provide a set of requirements suitable to a range of different heavy vehicles such as busses and trucks.

The machine design process is also implementing other aspects affecting the machine characteristics. This includes mechanical integrity of the rotor and thermal dependent behaviour. A cooling concept is chosen based on a desire to utilize already existing coolants in a drive train, specifically the transmission oil. The final machine design is also considering manufacturability in terms of choosing design parameters that potentially could ease the machine manufacturing.

The outcome is an oil cooled, 6-pole, 80/180 kW (cont./peak) PMSM with distributed windings and V-shaped magnet arrangement utilizing reluctance torque. The traction machine is connected to the existing drive train with a 6:1 gear ratio, to the gearbox power take off (PTO) port. This allows for a rotational speed in the electric machine, higher than that of the internal combustion engine (ICE). The base speed of the electric traction machine is 6000 rpm and the maximum speed is 15000 rpm. According to the well-known relation between power, speed and torque ($P = \omega \cdot T$), high rotational speeds makes it possible to reduce the torque demand and thereby the electric machine size. The resulting machine dimensions are 224 mm in active length and 200 mm in outer stator diameter, fitted in a 400 mm long, 220 mm outer diameter housing.

The prototype is built and experimentally verified. The machine build is briefly covered and the result of the manufacturability effort is studied at the machine manufacturer. When comparing the simulation result with measurements a good correlation is observed.

The main results can be divided in two:

I) The knowledge and skills in electrical machine design achieved by the author during the work. The main contribution is the parameterization and optimization of the magnetic, mechanical and thermal design. Lots of effort is also put in the analysis of deviations between expected and measured properties.

II) The actual traction machine design, a prototype that meets the design requirements and hence is suitable for propulsion of a hybrid electric heavy commercial road vehicle.

Acknowledgements

Lots of persons deserve my gratitude for making this thesis possible. First of all I would sincerely like to thank my main supervisor, Prof. Mats Alaküla for always being able to provide a way forward from every tricky situation. Despite a busy schedule there is always time for some encouragement, or a new angle of approach which makes it easy to draw parallels to the headmaster of Hogwarts, Prof. Albus Dumbledore.

For the everyday questions regarding everything related to the world of electric machines, my co-supervisor, Dr. Avo Reinap has been invaluable. Not to speak of the countless times he has helped guiding me through the thicket of "red text" in Matlab. Equally valuable, but in the mechanical field, have my other co-supervisor, Dr. Anders Hedman at Volvo GTT been. Also here, red text needs to be mentioned, however in this case related to the meticulous proofreading. In the initial work, Johan Hellsing also held a position as co-supervisor, which he did with honour.

If it not would have been for the Swedish Hybrid Centre (SHC), my work as a PhD student would most likely never have started. The same goes for Helena Berg, who encouraged me to grasp the opportunity to return to the school bench. And of course Vovlo GTT and my managers at the business function in Gothenburg, for being my employer and for letting me work in my own bubble in the middle of all the time-critical industrialization projects. Special thanks also to my colleagues in Gothenburg where my sounding board for stupid questions, Andreas Gillström and my "PhD friend" Hanna Bryngelsson deserves to be specially mentioned.

Anders Göransson at Sibbhultsverken AB for keeping the momentum in the project, Jan Folkhammar at Bevi AB for the week as a trainee when building the prototype, Lars Kvarnsjö at Vacuumschmeltze for the input to the thermal dependence model and Daniel Olsson at SP for the support during the machine testing, many thanks to all of you.

The department and all colleagues in Lund should also be acknowledged. Especially Yury Loayza-Vargas, as my partner in crime when blowing up the frequency converter, Getachew Darge as the ever helping hand when working in the labs and Fran Márquez-Fernández for always being able to explain that last piece of the puzzle, should be mentioned. Besides all you folks who have made the lunches so enjoyable and full of interesting discussions and laughter, thank you all!

An ever so important part in making it possible for me to complete this thesis is the fact that I have been provided with what can only be described as the best student accommodation ever heard of. Not only that there is food on the table and clean sheets in the bed when I arrive, but also that I often have had to persuade them *not* to pick me up at school in the end of a working day in Lund. For all of this and for everything else, Staffan and Britt, you have my warmest and most heartfelt thanks.

My mum Lena, dad Dan, brother Johannes and sister Elise, many thanks for all the encouragement and for listening interestingly although I not always have managed to explain what I am talking about.

And last but not the least, the two most important persons in my life. Caroline, thank you for sharing all my joy and all my sorrows and for always being there for me when I really need you. And Alicia, thank you for being you!

Göteborg, 9th of November 2014
Rasmus Andersson

Contents

Chapter 1

Introduction

1.1 Background

Experiences from the automotive industry during recent years prove the possibility to gain fuel efficiency as well as an improved environmental friendly reputation by implementing hybrid electric drive trains. This is valid for passenger cars as well as commercial vehicles such as busses and trucks. A drawback with the hybrid electric vehicle (HEV) is an increased investment cost due to the additional and often costly components. Especially commercial carrier companies that have to keep their business profitable finds the fuel efficiency as well as the investment cost crucial. Therefore, one of the challenges in commercial vehicular technology is to be able to provide good fuel efficiency for a reasonable capital expenditure. In order to do so by offering HEV technology, the system cost needs to be reduced. One way of reducing the cost is to reduce the bill of material, a part of which is the electrical traction machine. For any electrical machine (EM), the size of it is almost proportional to the torque. As power is the product of torque and angular speed ($P=T\cdot\omega$), a way to reduce the torque without reducing the power is to increase the speed.

1.2 Objectives

Purpose

The main purpose with the present work is to build knowledge in electric machine design and to learn how to use important tools useful in an EM design process. One such tool is a Matlab and FEMM[1] based design

[1] http://www.femm.info

tool [1] developed at the department of Industrial Electrical Engineering and Automation (IEA) at Lund Institute of Technology (LTH). In the work presented in this thesis, this design tool is further developed and verified against measurements to increase the capabilities of the tool. The purpose is also to gain a basic knowledge in the adjacent areas such as electric machine control with field weakening algorithms and torque control. Also the mechanical interface towards the rest of the drive train is included. Basic knowledge in mechanical power transfer through gear trains is needed to understand the other components in a powertrain.

The results related to machine control and field weakening are implemented in the test rig when the prototype machine is verified, but are not reported in this theses. The ambition with this thesis is to focus on the machine design related aspects of the work.

Finally the goal is also to present an electric machine design that can be used for electric traction in heavy hybrid road vehicles in a strictly limited geometrical space.

Method

A number of university courses are completed in order to increase the knowledge in the adjacent components in general and in electric machine design in particular. Electric machine design courses based on analytical expressions as well as finite element analysis (FEA) are completed. Basic knowledge in thermal dynamics and strength of materials is obtained via basic courses and further improved via self-studies and practical experiences.

The experiences obtained from the design process, prototyping and measurements are implemented in the design tool. Simulations are performed in Matlab/Simulink as well as in FEA software. The design tool uses Matlab and Lua script to control the FEA software and scan design variables in the design process. The manufacturability of the suggested machine design is evaluated in order to facilitate manufacturing, both for the prototype and with a possible future serial production in mind. The electric machine design is optimized to fulfil the specifications and requirements.

Electric machine control is implemented based on work previously done at IEA at LTH. Torque speed curves are obtained by following the maximum torque per amp (MTPA) curve. The control goes into field weakening

(FW) when maximum current is reached. When reaching the vicinity of maximum rotational speed, the current is controlled along the minimum flux per torque (MFPT) curve. This is implemented with look up tables. Based on the rotational speed, dc voltage and torque request, the current references are returned and supplied to the frequency converter vector current controller.

The suggested design is manufactured and tested to verify the simulation result. The result is also used for feedback to the simulation tool.

1.3 Contributions

The main contributions of this thesis, besides the personal development and experience gained by the author, are:

- The compilation of aspects important to consider in an electric machine design process. This includes:
    - Electromagnetic aspects related to e.g. the shape of the stator and rotor, the selection of material and the introduction of skewing.
    - Thermal aspects in terms of cooling strategy and the thermal influence on the machine performance.
    - Mechanical strength evaluation of the rotor in order to cope with the centrifugal forces, both within normal operating range and in over speeding events.
    - Evaluating the manufacturability of the design in order to facilitate when building the electric machine.

  In addition to this, aspects important to consider when working on a traction machine for heavy vehicles is also covered. This implies in particular the limited geometrical space and the interaction with the existing heavy vehicle drive train.

- A documented complete sequence of specification – design – manufacturing – testing of a traction machine intended for a heavy vehicle application. The prototype is used as a reference machine in a project called: "ExSAM drive for a Commercial Vehicle Hybrid Transmission", financed by the Swedish Energy Agency (Energimyndigheten)[2].

[2] http://www.energimyndigheten.se/Forskning/Projektdatabas
FFI Project number: P32750-1

- Further evaluation of an alternative test method, so called "dynamic testing", to the traditional bench testing, when characterizing electric machines, by using it for the testing of the machine in focus in this thesis.

- Further development and verification of the design tool used at the department at Lund University. This includes a thermal dependence of the permanent magnets and an analytical approach to investigate the mechanical strength of the suggested rotor design.

- Improved insight in powertrain mechanics at the department in Lund by the work done to identify the most suitable location for the electric traction machine in an existing heavy vehicle drive train.

- Improved knowledge of electric machine design adapted to heavy vehicle applications at the AB Volvo business function in Gothenburg.

- Supervising two students in their Master of Science thesis work on using the electric traction machine for synchronizing of the gearbox when shifting gears.

Publications

Parts of the content covered in this thesis work are also covered in the following publication:

- Andersson, R., Reinap, A., Alaküla, M. (2012), "Design and Evaluation of Electrical Machine for Parallel Hybrid Drive for Heavy Vehicles". *20th International Conference on Electrical Machines (ICEM2012)*, Marseille, France, Sept. 2-5, 2012, pp. 2622-2628.

In addition to the design work presented in this thesis, the author has also designed another traction machine with the same specifications, housing size, gear ratio etc, but a totally different content. This is done as a continuation in the project[2] in which this thesis is a part of. This design is an axially segmented three phase machine with laminated stator windings designed to be directly air cooled. The design work and experiences from that machine is for consistency reasons intentionally left out of this thesis. The following publications are related to the alternative machine design:

- Andersson, R., Högmark, C., Reinap, A., Alaküla, M. (2012), "Modular Three-phase Machines with Laminated Winding for Hybrid Vehicle Applications". *International Electric Drives Production Conference and Exhibition (EDPC2012)*, Nuremberg, Germany, Oct. 16-17, 2012.

- Högmark, C., Andersson, R., Reinap, A., Alaküla, M. (2012), "Electrical Machines with Laminated Winding for Hybrid Vehicle Applications". *International Electric Drives Production Conference and Exhibition (EDPC2012)*, Nuremberg, Germany, Oct. 16-17, 2012.

- Reinap, A., Marquez-Fernandez, F.J., Andersson, R., Högmark, C., Alaküla, M., Göransson, A. (2014), "Heat transfer analysis of a traction machine with directly cooled laminated windings". *4th International Electric Drives Production Conference and Exhibition (EDPC2014)*, Nuremberg, Germany, 30 Sept. – 1 Oct., 2014. (Awarded best conference paper.)

1.4 Outline

Chapter 1 is used to introduce the project and to list its objectives. The Method with which is achieved is also included

Chapter 2 covers the input used to determine the specifications of requirements of the electric machine. Some different hybrid system concepts are explained. A brief introduction is done on the electric machine and gearbox as the two main subsystems in the concept. The pre studies performed to settle the specifications of requirements are explained and finally the resulting list of requirements is summarized.

The development process of the electric machine design is presented in Chapter 3. Electromagnetic simulations as well as mechanical and thermal aspects are used when generating the machine design. The machine characteristic from the simulation environment is also presented.

Chapter 4 covers the prototype manufacturing, explaining briefly the building process and reflects a bit regarding the design choices done to facilitate manufacturing.

The measurements performed on the prototype so far are explained in Chapter 5. This includes no load tests on the induced voltage at room

temperature as well as at higher operating temperatures. The no load torque is also measured to determine no load losses. Measurements when loaded are performed with dynamic loading and the result is compared with the simulation results. Some result is also obtained from the machine being mounted in a system test rig. These results are limited due to problems with the test rig. Finally the experiences gained during the testing are concluded.

Conclusions from the project together with some reflections and a list of future work summarize the thesis in Chapter 6.

Chapter 2

Machine specifications and requirements

The following chapter covers the pre studies done to give input to the electric machine design work. The overall goal is a lightweight but powerful machine that can operate over a wide speed range. The outcome from the chapter is a machine specification used as input in the machine design process.

2.1 General specifications

The general specifications used as input to the project are listed here. Many of these specifications are not requirements as much as things to bear in mind when setting the project scope.

- The geometrical limitations are those stated by the powertrain compartment in a truck or bus. Although no absolute volumes are provided, the general specification is stated as “it is of no use if it does not fit”.

- The electric machine is to be used in a parallel hybrid drive train.

- Electric power required by the machine is in the range of at least 70 kW continuous and 120 kW in peak. These numbers are based on the first generation Volvo hybrid vehicles rather than studies of future needs. The definition of peak power is also rather vague.

- Machine control is to be done with a conventional three phase frequency converter.

- An available energy storage system sets the voltage level for the machine. Nominal voltage in the system is 600Vdc but may vary from 530-725Vdc depending on the state of charge and the traction power. This means designing the machine for 530V since the lower voltage level means higher currents for a set power level.

- Considerations must be done to mechanically handle over speeds in case of for example faulty gear shifts. This is valid for those concepts where the machine is mounted in connection to the gearbox. The requirement for clutch discs is to be able to handle 50% over speed. This is defined as burst speed.

- Cooling is to be implemented in integration with other components in the drivetrain. This to minimize the complexity of the hybrid electric system. Examples on cooling media that can be used are the WEG (water/ethylene/glycol) mixture used for the frequency converter or the oil used for cooling and lubrication in the gearbox.

- If the electric machine is to be connected through a gear, only one gear step is allowed. Hence the gear ratio is to be fixed and will not be able to be changed when in operation. This will minimize the complexity of the hybrid electric system.

2.2 Subsystem description

Before the system description and pre studies are presented, the two main components are introduced. The following sub chapter gives a short introduction to the EM and the gearbox as two main components in a HEV driveline. The third component, being the ICE is excluded in this thesis.

Electric machine

The electric machine terminology used in the thesis is defined according to Figure 2.1. An electric machine can be divided into the active parts containing the magnetically active components and the components needed to mechanically keeping the machine together. The active parts are the rotor and stator together with the components contained therein, such as the permanent magnets and the conductors in the slots. Non active

components are typically the housing, shaft, bearings, resolver and the end winding part of the conductors. When doing electromagnetic simulations, only the active parts are considered.

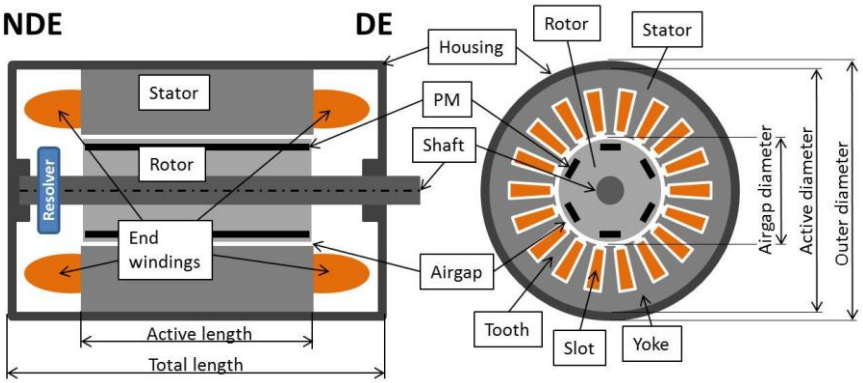

Figure 2.1 Principle sketch of a Permanent Magnet Synchronous Machine with 6 poles and 18 slots

Electric machines can look very different in terms of size and shapes. Depending on the intended application, machines with the same power ratings can be short-and-wide or long-and-slender. A short-and-wide machine typically produces high torque but is limited in top speed due to a higher peripheral speed. A rule of thumb from the machine manufacturer[3] is to start considering and keeping track of the mechanical stresses in the rotor when the peripheral speed exceeds 80-85 m/s. Higher rotational speeds can be achieved as long as the rotor is designed with sufficient mechanical integrity. Machines with large diameters typically also have a higher moment of inertia. The long-and-slender machines can operate at higher speeds but typically produces less torque per volume. The vast number of different machine topologies makes it hard to do just comparisons. One way to compare different machines is to look at the shear stress, or force per airgap area, σ [2], [3]. By studying the shear stress for different EM, the properties of machines with various sizes and shapes can be compared. If two different looking machines have similar shear stress, they can be said to be comparable to each other. The shear stress is defined as the force applied from the rotor related to the stator due to the developed torque, T. This is shown in equation (1) where r_A is the airgap radius and l_R is the rotor (hence active) length of the machine.

[3] Folkhammar, Jan (Bevi AB).

$$\sigma = \frac{F}{A} = \frac{T}{r_A} \cdot \frac{1}{2\pi \cdot r_A \cdot l_R} = \frac{T}{2\pi \cdot l_R \cdot r_A^2} \quad (1)$$

Control of an electric ac machine with a dc/ac frequency converter is generally done with some form of field oriented vector control in a synchronously rotating reference frame. The three phase ac quantities are expressed as rotating vectors defined in a stator stationary reference frame (α,β) aligned with the stator. The nomenclature used in this thesis denotes a reference frame aligned with the rotor (x,y) and a reference frame aligned with a flux vector (d,q), where d- refers to "direct axis" and q- to "quadrature axis". When using a reference frame that rotates synchronously with a flux vector, the rotating vectors can be expressed as dc quantities in the rotating reference frame. In this thesis the modelling and control is done in a rotating reference frame defined so that the *x*-, or d-, axle is aligned with the permanent magnetic north pole in the permanently magnetized rotor. The *y*-axis is placed orthogonal to the permanent magnet flux. Note that as the orientation is aligned with the PM rotor flux both rotor orientation (x,y) and PM flux orientation (d,q) is fulfilled. Thus both the (x,y) and (d,q) nomenclature can be used. 360° is defined as the distance between two magnetic north poles. This means that for a multi-pole machine, one mechanical lap of 360 mechanical degrees will consist of multiple electrical laps. More details regarding the transformation from three phase ac quantities to two phases in the rotor aligned, rotating reference can be found in, e.g., [4], Ch. 2.2.

AMT gearbox

The gearbox used in the project is an Automated Manual Transmission (AMT) intended for commercial vehicles. The gearbox has three base gears, two split gears and two range gears which together result in twelve gears. The input shaft is connected to a countershaft via either high split (HS) or low split (LS) and the base gears connect the countershaft to a main shaft. The range gear is a planetary gearing that drivingly connects the main shaft to the output shaft, either with speed reduction (low range, LR) or directly (high range, HR). The interface to the combustion engine is defined according to a standard interface called SAE#1 (from the Society of Automotive Engineers) which among other things states the diameter. A companion flange is used to connect the output shaft to the prop shaft. The PTO or Power Take Off is a mechanical output that makes it possible to attach mechanical loads, e.g. a hydraulic pump to the gearbox. A principle sketch of the gearbox is presented in Figure 2.2 where the input shaft, countershaft, main shaft and output shaft are

presented. The two split gears, the three base gears and the range gear are marked as well.

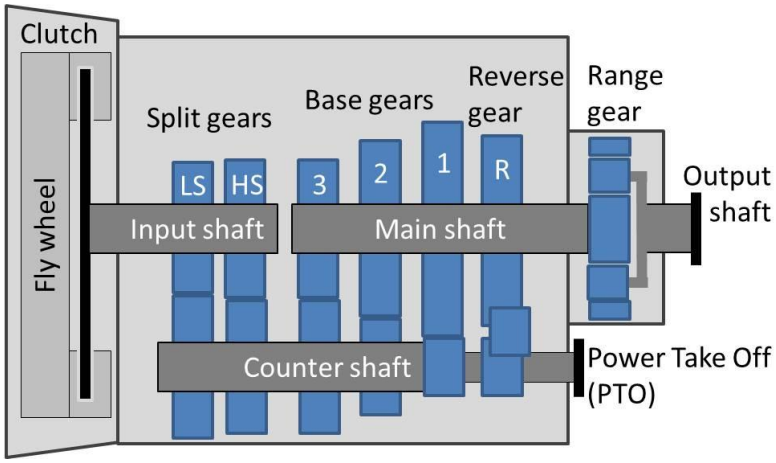

Figure 2.2 Principle sketch of a 12 speed AMT gearbox intended for commercial vehicles

2.3 System description

The system in which the EM is intended to be installed is a parallel hybrid electric commercial vehicle such as a bus or a truck. The parallel architecture means that the vehicle can be propelled by EM, the ICE or by the two components together. Since the EM is operating in close connection to the conventional driveline components, consideration needs to be taken to those components when doing the design work. The EM can be connected to the conventional driveline at a number of different positions related to the gearbox. The following sub chapters give an introduction to some different possible connection points for the EM. Excluded are the options where the EM is mounted before the clutch since this would not allow operation with the EM only. Finally one of the concepts is suggested for further investigations.

Pre gearbox mounted EM

When mounted between the ICE and the gearbox, the geometrical position introduces limitations in size. The outer diameter is limited by a desire to keep the SAE#1 interface intact towards the gearbox and clutch housing. The inner diameter is limited by a desire to fit the clutch actuator. The total length is limited by restrictions in the overall powertrain length. Finally,

unless a planetary gear is fitted between the EM shaft and the gearbox shaft, the rotational speed is limited to match the ICE rotational speed. Introducing such a planetary gear would both increase the complexity in the system and also increase the length, alternatively further limit the inner diameter. A principle sketch of the EM mounted between the ICE and the gearbox is presented Figure 2.3.

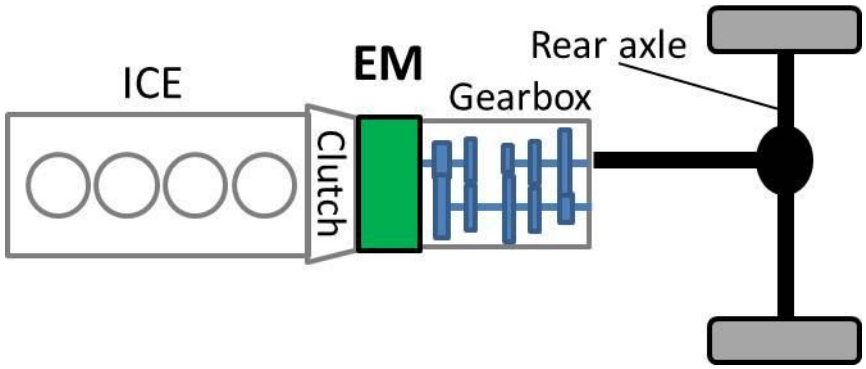

Figure 2.3 Principle sketch of a parallel hybrid electric drive train with the EM mounted between the ICE and the gearbox

Post gearbox mounted EM

The EM can also be mounted downstream from the gearbox. This includes for example being attached to the prop shaft close to the gearbox, at the universal joint or close to the wheels. To match the ICE torque contribution which is increased in the gearbox, the EM will have to be able to deliver a rather high torque. One way to reduce the EM torque would be to introduce a (fixed) gear drive in the connection between the EM and the rest of the drive train. This allows for a more suitable EM speed range, where higher base speed implies lower torque and hence size for a given power rating. The concepts not possible to connect with a gear drive will suffer from either a high torque demand or from the need to implement multiple machines. Both cases will drive cost. Three different possible post gearbox positions are shown in Figure 2.4. The prop shaft connected and universal joint connected EM are shown with a gear drive while the close-to-wheel mounted machines are considered direct drives. As can be worked out by looking in Figure 2.4, this concept is presumably increasing the flexibility of the electric machine in terms of length and diameter.

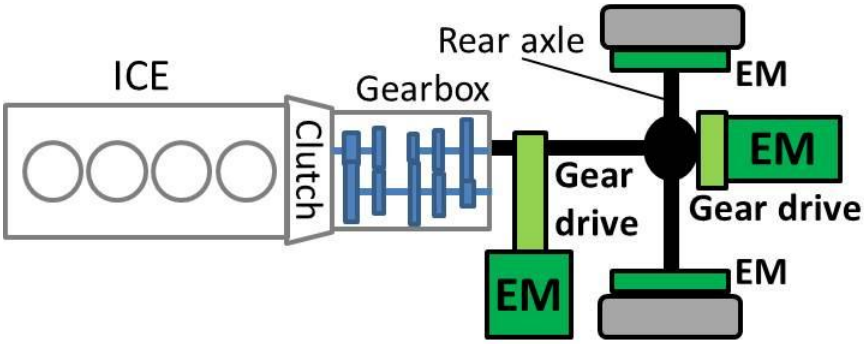

Figure 2.4 Principle sketch of a parallel hybrid electric drive train with Ems mounted at a number of positions downstream from the gearbox

Irrespective of a gear drive connection or not, all the post gearbox concepts require a speed range that can cover the entire vehicle speed range, from standstill to top speed. This could be disadvantageous when recuperating energy during decelerations. As soon as the rotational speed drops below base speed, the available recuperated energy is reduced. This is further explained in Figure 2.5 where the *x*-axis indicates the time for a deceleration to standstill and the *y*-axis displays power. The area in the left graph shows available energy (W_{brake}) during a deceleration with no downshift. In the right graph a gearshift is included. As can be seen in the simplified graphs, it might be possible to recuperate more energy (W_{brake1} + W_{brake2}) with than without the gear shift, despite that the lost energy during the gear shift (W_{shift}) is accounted for. This obviously means that the time for shifting a gear should be minimized.

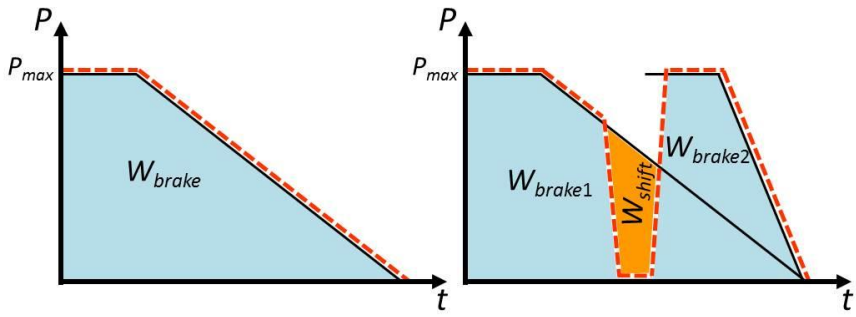

Figure 2.5 Principle sketch of recoverable energy (W_{brake}) without (left) and with (right) a gearshift during deceleration

On/In gearbox mounted EM

A third option is to connect the EM to the PTO in the gearbox hence connected to the countershaft. In this way the EM utilizes some of the available gear steps in the gearbox and still has the flexibility in terms of rotational speed and geometrical space as that of a post gearbox mounted EM. It is possible to implement a dedicated gear drive to shift up the speed of the EM, thus making it possible to use a smaller, more power dense EM with lower torque rating. Being transferred through some of the gears in the gearbox, the EM torque and top speed can be varied over the drive cycle. This opens for a possibility to somewhat optimize the operation points to fit with the efficiency map. A principle sketch of a PTO mounted EM is seen in Figure 2.6 where the EM is connected via a fixed gear drive.

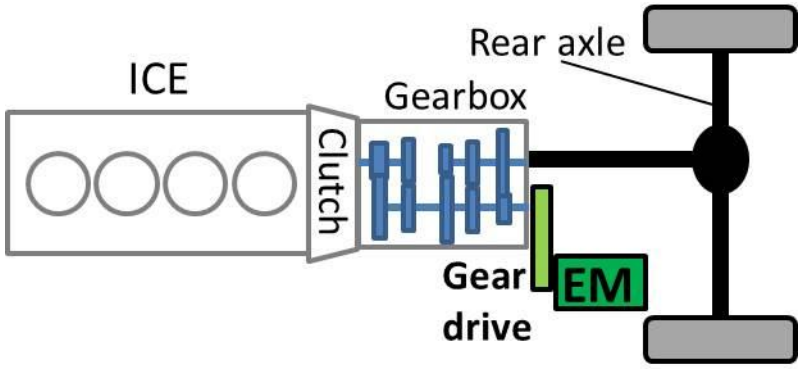

Figure 2.6 Principle sketch of a parallel hybrid electric drive train with a PTO mounted EM

Hybrid system selection

The conclusion from studying the different options is to go ahead with the PTO mounted EM. This is considered to provide a flexible solution in terms of size and rotational speed for the EM. It is also possible to use the advantages of the available gearbox.

2.4 PTO gear analysis and result

A pre study is carried out to determine the approximate size and properties required by an EM connected to the hybrid driveline via the gearbox PTO according to Figure 2.6. The purpose of the study is to investigate the concept in terms of giving an indication of the size and shape of the PTO mounted machine together with an approximate gear ratio of the PTO gear

(denoted "Gear drive" in Figure 2.6). The study is performed by assuming a vast number of different machine sizes and PTO gear ratios and is mainly done by simulations in Matlab.

Simulation prerequisites

Before simulation is started, some assumptions are established together with some restrictions. These are used to limit the number of possible alternative outcomes from the study.

Assumptions

A fixed desired EM power and torque contribution is assumed as seen at the low speed side of the PTO gear. These are kept constant throughout the simulations. The power is set according to the specifications in section 2.1. The torque level is settled by a desire of being able to crank the ICE. The top speed is settled to match that of the ICE. The idea is that the EM torque and speed seen from the ICE are equal irrespectively of the PTO gear ratio. This means that a machine connected via a large gear ratio can have a lower torque rating, but have to be able to rotate faster than a machine connected via a small PTO gear ratio. It is also desired that the EM shall be able to deliver full power throughout the whole vehicle speed range, with exception of speeds below base speed in the 1st gear.

The shear stress (explained earlier in equation (1)) is assumed to be equal for all electric machines in the investigation. Ch. 9, pp. 18 in [2] states that up to 70 kN/m² is possible while [3] pp. 24, mentions numbers in the range 10-100 kN/m² depending on the machine type and size. In consultations with the supervisors 40 kN/m² is selected for the pre study.

The fixed PTO gear ratio between the EM and the countershaft is varied from 1:1 to 5:1 in order to investigate different resulting machines. This is done with an assumption that a too high EM top speed would require special high speed bearings. The configurations with larger PTO gear ratios are not disregarded, but considered less viable hence not included in the first evaluations in the pre study.

The outer diameter of the stator yoke is varied from 200 mm to 400 mm. Corresponding airgap radii (r_A) are determined based on the stator yoke radius (r_S) so that it varies linearly from 50% to 70% of r_S for the machine with the smallest and largest diameter respectively. This is implemented according to (2) where a reference radius r_{Sref} equal to the smallest stator yoke radius is introduced. The rotor thickness is assumed to be constant

for all airgap radii hence the inner radius is determined by the airgap radius.

$$r_A = r_S \cdot \left(0.3 + 0.2 \cdot \frac{r_S}{r_{Sref}}\right) \quad (2)$$

$$l_R = \frac{T}{\sigma \cdot 2\pi \cdot r_A^2} \quad (3)$$

The assumed torque, shear stress and rotor radii are used to solve equation (1) in chapter 2.1 for the rotor length (l_R). This is done in equation (3). As can be seen a larger diameter means a shorter machine. Simple geometry is used to determine the rotor and stator volumes. The volume and an assumed average density are used to obtain the rotor moment of inertia J_{EM}. The moment of inertia from the countershaft J_{CS} is assumed to be known. The EM torque and the moment of inertia are used to estimate the rotor acceleration capability during gearshifts according to equation (4). The rotor acceleration capability with the counter shaft inertia attached, is interesting to study since it can open for using the EM to synchronize the gearbox during gear shifts. To take the torque reduction above base speed into consideration, only half the available torque is used in these calculations. The PTO gear ratio between the EM and the countershaft is denoted *k*.

$$\frac{d\omega_r}{dt} = \frac{T/2}{J_{EM} + J_{CS}/k^2} \quad (4)$$

The entire motor weight is also used to mutually compare the cost by assuming a correlation between the expenditure of material and the machine cost. For simplicity and since this is intended as a coarse estimation only, the manufacturing cost is neglected. Consequently, the smallest machine is considered being the cheapest and hence a better choice.

Restrictions

The acceleration capability described earlier in equation (4) is used as input to limit the number of suitable EM configurations. According to the discussions around Figure 2.5 the time it takes to shift gear is to be minimized. This is favourable for the drivability as well as for the energy

recuperation during decelerations. A time limit for the speed increment is implemented and those machines not fulfilling the acceleration times are disregarded. The restriction based on the requirements on the existing synchronization brakes, is set to 1200 rpm in less than 0.4 s, hence slightly over 300 rad/s.

Length restrictions related to the radius is implemented. According to the assumption that all machines have the same shear stress, length and radius can be varied without affecting the torque capability. In order not to get a too long and slender machine, the maximum allowed length is limited to 3 times the airgap radius during the pre-study.

The EM base speed is investigated in terms of being able to deliver full power on all gears. Since the gear shifts are initiated by the needs of the ICE, the EM speed might be rather low after an up shift. In order to be able to deliver full power in those cases, the base speed must be sufficiently low. For a set power, this can be achieved by increasing the EM torque. Therefore, the torque requirement is increased compared to the assumption originally presented.

Simulation results

The assumptions and restrictions are implemented in Matlab with the result plotted as surfaces representing a vast number of machines with different stator yoke radius and PTO gear ratio to the gearbox. The common factor for all machines is a constant power and a constant shear stress or force per airgap surface, defined as in equation (1) in chapter 2.1. In the following graphs the stator yoke radius is varied along the *x*-axis and PTO gear ratio along the *y*-axis. The result is shown on the *z*-axis.

Figure 2.7 presents how the motor volume depends on stator yoke radius and PTO gear ratio. As can be seen, the volume increases with lower gear ratio and also with smaller r_S. This graph is also used to do a coarse estimation of the motor cost with the simple assumption that a larger machine uses more material and hence costs more. The least expensive machine according to this approach would be the one in the uppermost corner hence with a large radius and connected via a high PTO gear ratio.

Figure 2.8 displays the rotor acceleration capability for the different machines. As can be seen increased inertia due to larger r_S along the *x*-axis results in a reduction in acceleration. The PTO gear dependence along the *y*-axis comes from the countershaft inertia which although being constant

is transferred through different gear ratio, thereby affecting differently according to the relation described in equation (4).

In Figure 2.9 where the active length is plotted, the length versus airgap radius restriction (introduced previously) is included as a shaded surface. Since the restriction states that all machines with a length longer than 3 times the airgap radius are too long, all configurations above the shaded surface in Figure 2.9 are disregarded. Hence the low radius, low PTO-gear machines are disregarded.

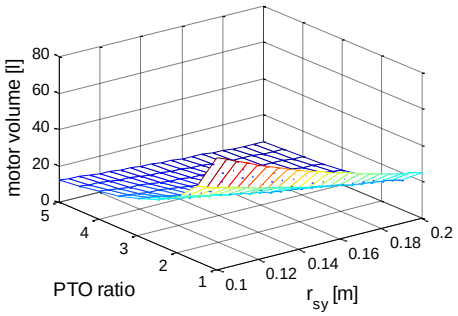

Figure 2.7 Resulting motor volumes as a function of stator yoke radius and PTO gear ratio

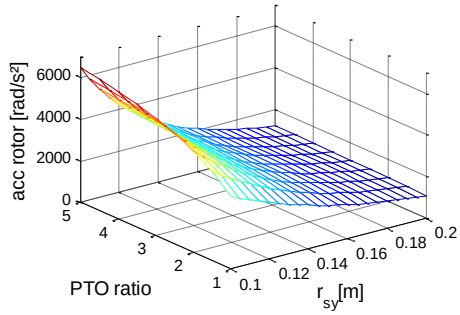

Figure 2.8 Rotor acceleration as functions of stator yoke radius and PTO gear ratio

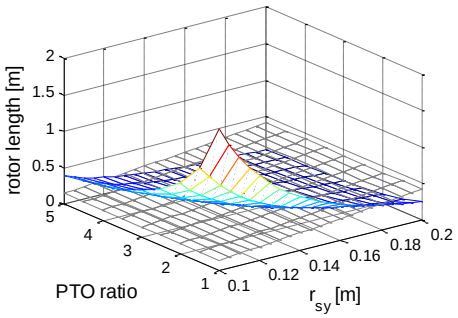

Figure 2.9 Rotor length as a function of stator yoke radius and PTO gear ratio including upper length versus radius restriction

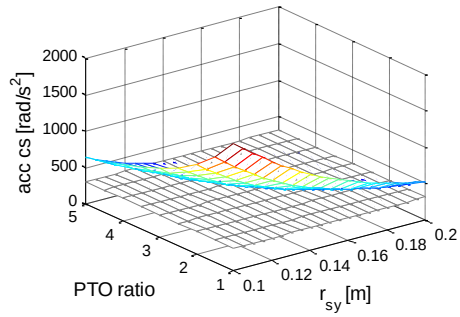

Figure 2.10 Countershaft acceleration capability during gearshifts as function of stator yoke radius and PTO gear ratio including acceleration restriction

The acceleration capability restriction is included in Figure 2.10 showing the countershaft acceleration during gear shifts. Since the restriction states that the acceleration must be sufficiently fast, all configurations slower than, hence below the limit are disregarded. Consequently, large radius, large PTO gear machines are disregarded.

The available configurations after sorting out the designs not fulfilling the restrictions is presented in Figure 2.11.When taking the volume as a cost indicator into consideration, the most advantageous machine configuration is with a high PTO gear ratio. The difference implied by the stator radius is less conclusive at higher gear ratio. The machine design weighted as most suitable is used for some further evaluation.

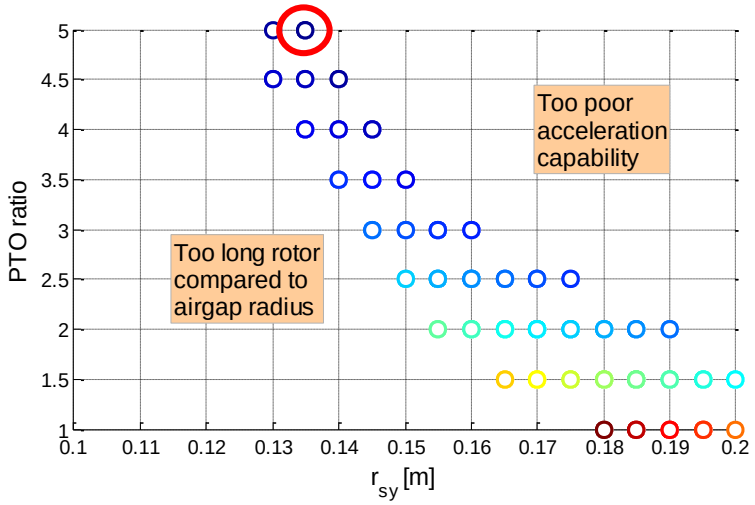

Figure 2.11 Available configurations with consideration to the restrictions with the most suitable machine design encircled

Based on the assumptions and restrictions mentioned previously, one machine design is chosen for further evaluation. The machine in question is encircled in Figure 2.11 and the torque and power curves of the machine are plotted in Figure 2.12. Figure 2.13 presents the result at the output shaft as a number of EM torque-speed maps together with torque speed maps from a 7 litre ICE. The different curves are to be interpreted as the torque speed curves transferred via different gears in the gearbox. Since the EM is mounted at the countershaft, the EM torque contribution is shifted through the base gears only, hence there are three torque-speed lines compared to the six ICE torque-speed lines.

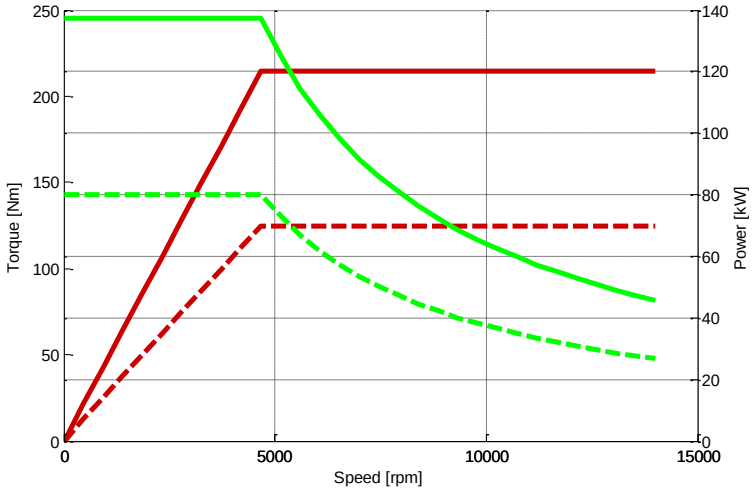

Figure 2.12 Peak and continuous torque and power of the most suitable EM according to the assumptions and restrictions made in the PTO gear analysis

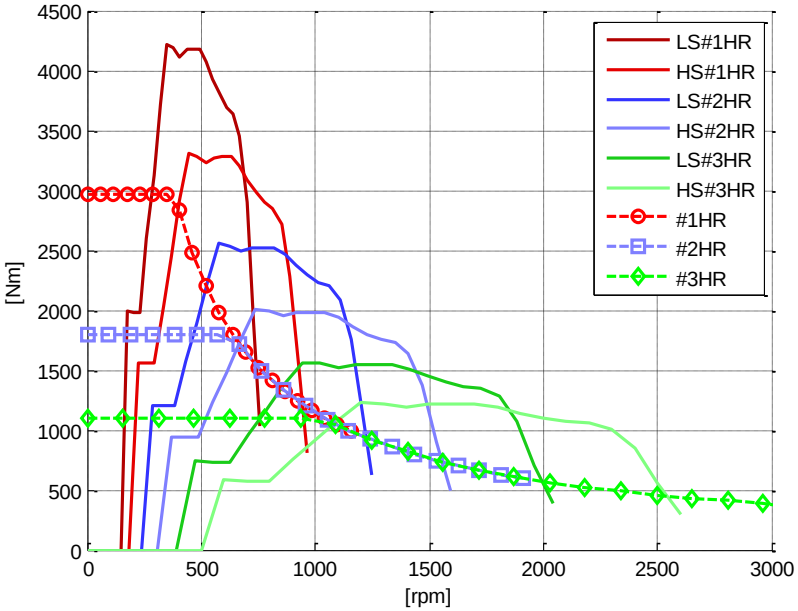

Figure 2.13 Torque at the output shaft with high range

The base gear shift is normally initiated by the ICE so that full ICE torque can be delivered to the wheels. This means shifting gear in order to get the highest possible torque at all possible rotational speeds. The consequence for the EM is that it has to be adapted to being able to follow the ICE gear shifts. Looking in Figure 2.13 it can be seen that the transitions from one ICE curve to the next (where a gearshift most likely will occur) takes place above the EM base speed. Hence the EM in Figure 2.13 can operate as desired and deliver full power with no power dips throughout the entire speed range as stated in the underlying assumptions previously stated.

Looking at the EM top speed when comparing to when a gearshift is initiated by the ICE curves in Figure 2.13 it can be seen that it is possible to increase the PTO gear ratio without reaching EM over speed. This is not implemented in the pre study, but considered further in the main project.

2.5 Hybrid simulation model

A hybrid vehicle model in Matlab/Simulink environment is used to investigate the power requirements for an electrical machine in a parallel hybrid transmission topology. The model is developed for educational purposes at the department of Industrial Electrical Engineering and Automation and is described further in [5] and [6]. The average electric power requirement for a 22.5 tonne vehicle in a city bus drive cycle is according the simulation model around 40 kW. For a 40 tonne vehicle the average power is around 60 kW. The intermittent peak power is in the range of two to three times as high. To provide a margin and also allow for a possibility to implement electrified auxiliary loads, a continuous power of 80 kW is chosen. This choice is also made with considerations to the input stated in section 2.1. The simulation result also indicates that the fuel efficiency generally benefits from high intermittent power. Therefore the target for the peak power is to reach around 180 kW.

2.6 Additional specifications imposed by the concept choice

Important limitations to bear in mind are those related to mounting the machine in the intended application. Especially important is the possibility to fit the machine in the available space in the vehicle. In order to gain as much benefits as possible, the machine should also be adopted to the intended installation in other ways. A too small machine does not utilize the geometrical space in an optimal way. Potential limitations in mechanical strength at the connection points as well as surrounding factors

such as available dc-voltage, intended ac-converter and practicable cooling possibilities also need to be considered.

Packaging specifications

The suggested connection point for the machine is as discussed in previous chapters (On/In gearbox mounted EM) at the countershaft, connected via a PTO-mounted gear drive. In order to obtain a compact design for the EM and gearbox, the machine is mounted side by side to the gearbox. This sets the geometrical dimensions for the installation to those defined by the gearbox length together with the distance between the side of the gearbox and the frame. This gives a maximum machine length of 400 mm from the connection point in the PTO mounted gear along the gearbox to the clutch housing. The maximum machine width, limited by the frame is 220 mm which defines the outer diameter (OD). A principle sketch of the intended location can be seen in Figure 2.14.

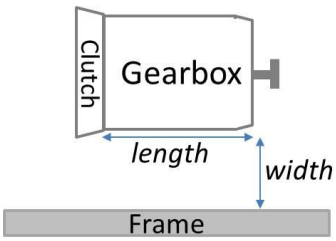

Figure 2.14 Geometrical limitations at the intended EM location

Torque specifications

The counter shaft extension towards the PTO (see Figure 2.2) is originally intended to handle power to PTO mounted auxiliary loads such as hydraulic pumps etc. This implements a limitation in torque from the EM. In order to be sure not to damage the splines in the connection, the torque from the EM should not exceed approximately 1500 Nm. This is considered at the low speed side of the PTO gear step hence the EM torque should not exceed 1500 Nm divided by the gear ratio in the PTO gear drive.

Cooling specifications

With the EM mounted in close vicinity to the gearbox it is desirable to integrate the cooling with the gearbox. An attractive solution is to implement oil cooling using gearbox oil with the gearbox oil sump as a common oil reservoir. The possibility to implement direct cooling rather

than indirect cooling makes oil a competitive choice despite a lower specific heat than water [7]. Direct cooling means that the coolant is applied directly onto the active parts such as the stator yoke or the end windings. Indirect cooling typically has cooling channels in the housing. Moreover, conventional liquid cooling in vehicle applications is usually implemented with WEG, which has a specific heat lower than that of pure water.

2.7 Summary of specification of requirements

This section concludes the findings into specification of requirements for the electric machine. Chapter 2.4 states that a rather large PTO gear ratio is advantageous from an EM size point of view.

A gear ratio of 6:1 is chosen, which is slightly higher than what is covered in the pre study. This is based on the discussions around Figure 2.13 that it would be possible to increase the gear ratio slightly more in order to match the EM speed with the ICE.

The torque limitations stated earlier in section 2.6 together with the gear ratio gives a maximum EM torque of 1500/6=250 Nm. The maximum rotational speed is also set by the gear ratio in order to fit the ICE speed. Assuming 2500 rpm as ICE top speed results in an EM speed of 2500·6=15000 rpm.

The limited provided space and a high peak power demand require a high power density machine. To meet this demand a permanent magnet synchronous machine (PMSM) topology is chosen. The constant power speed range (CPSR) due to the power and torque requirements can be achieved due to rotor reluctance or stator reactance, suppressing the permanent magnet (PM) excitation. For the given diametrical space constraint and the desired peak power, there is a risk for saturating the stator back. Hence a major part of the effort is to focus on fulfilling the peak power demands. All requirements from the different pre studies and assumptions are summarized in Table 1.

Table 1 Machine specifications and requirements

Machine type	PMSM
Continuous power	80 kW
Peak power	180 kW
Peak torque	250 Nm
Top speed	15000 rpm
Maximum available length	400 mm
Maximum available width (OD)	220 mm
Number of phases	3
dc voltage range	530-725 Vdc
Coolant medium	Gearbox oil
PTO gear ratio	6:1

Chapter 3

Machine Design

The machine design work is carried out as a parametric scan of design parameters that define a machine layout for electromagnetic and thermal 2D FEA. The constraints and the design variables of interest are changed consequently in order to converge to a suboptimal solution. With the limited active stator diameter and high peak power demand stated in the previous chapter, magnetic saturation is expected to occur in the stator back and teeth. Consequently, the dynamic overloading in terms of peak torque, peak power and magnetic saturation is prioritized over the nominal operation and efficiency. Some focus is also directed towards obtaining low torque ripple in order to avoid unnecessary noise and vibrations in the gear drive. Similarly, the arrangement between the stator electromagnet and the rotor permanent and reluctance magnet are formed in order to meet the CPSR, nominal to peak power and torque ratio, as well as thermal requirements. Consideration is also made to try to facilitate manufacturing throughout the design work.

3.1 Design tools

A design tool [1] developed at the department at Lund University is utilized for the design work. The design tool is also described and refined in [8]. The design process is controlled from a Matlab program creating a Lua script[4] that controls the FEA software FEMM. Running from Matlab makes it possible to automatically scan different load points and rotor positions as well as different design parameters. It also allows for

[4] http://www.lua.org

implementing analytical checks that can sort out designs not suitable before starting the FEA simulations. This leads to a reduction of the computational effort and time for a simulation batch. Each design making it to the FEA simulations is saved as a text file that is loaded and post processed in Matlab. The result is a vast number of different machine designs that are analysed to find the one most suitable for the application. The process is described as a flowchart in Figure 3.1.

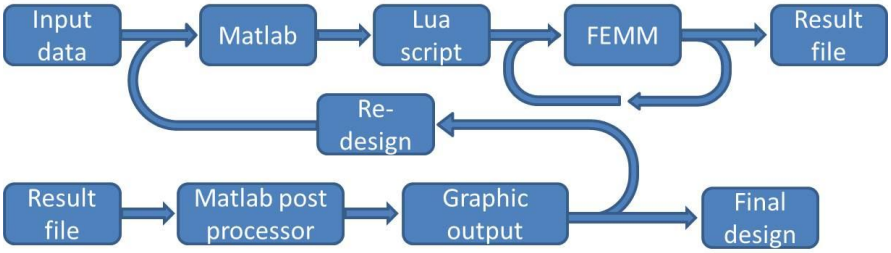

Figure 3.1 Flowchart of the design tools functional process

The input to Matlab is partly different design parameters such as slot width or yoke thickness and partly the different loading points. A reasonable continuous current density is settled based on thermal FE-calculations. The loading points are typically defined as a current matrix with a number of multiples of the continuous current density expressed as (x,y) coordinates in the rotational reference frame. These load points are used to create a diagram as shown to the left in Figure 3.2. In this specific case the current matrix consists of sixteen different loading points distributed from 0 to 3 times continuous current in y-direction (i_{sy}) and 0 to -3 times continuous current in x-direction (i_{sx}). The line and corresponding numbering defines (#1) the max torque per amp curve, (#2) the field weakening curve and (#3) min flux per torque curve according to [9] and [10]. Included in the load map is also the stator flux linkage modulus ellipses in whose epicentre the MFPT line ends. A typical result in the torque speed diagram can be seen to the right in Figure 3.2.

A number of different simulations at different rotor positions are performed for every load point. This makes it possible to evaluate for example flux as function of rotor position and torque ripple. The design tool takes advantage of symmetrical similarities to minimize the computational effort.

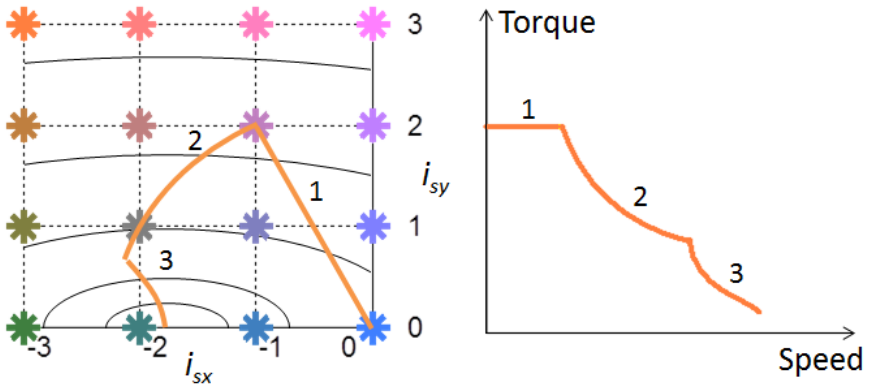

Figure 3.2 Typical current density matrix used as input into the design tool with (1) MTPA-, (2) FW- and (3) MFPT-lines (left) and the corresponding torque speed diagram (right)

3.2 Electromagnetic design

Different machine parameters are swept and the result is evaluated. Some parameters are set as input in order to limit the number of possible designs. These are presented below, followed by the design parameters of the rotor and stator. Finally the design is reviewed with aspect to manufacturing. The machine parameters investigated are exemplified in Figure 3.3 to aid the explanations in the following section.

Electromagnetic design inputs

The available geometrical space limiting the OD to 220 mm is used as input for stator diameter. Assuming a 10 mm thick housing results in 200 mm active diameter. This is lower than the suggested diameter from the pre study and is rather established with the first specification in section 2.1 in mind. Active length is settled later in the process after discussions with the machine manufacturer regarding required end winding length.

Based on a number of pre FE-calculations showing that a too high pole number would result in increased flux leakage between the poles, the number of poles in the machine is set to 6. This also keeps the maximum fundamental frequency sufficiently low to allow the use of a standard drive for the given power level. With a top speed of 15000 rpm, the highest fundamental electric frequency is 750 Hz.

The over speed demand is taken into account when choosing internal permanent magnets (IPM) rather than surface mounted. This also facilitates the desire to implement over loading capabilities [11].

The slot fill factor, indicating how large part of the slot that actually contains copper is set to 40%. This is based on previous experiences when building machines at the department and is also confirmed later on when discussing the winding procedure with the machine manufacturer.

Rotor design

The outer rotor radius, or airgap radius is set in order to provide sufficiently large stator slots but also to limit flux leakage between poles. A large airgap radius means more space between the magnets hence less flux leakage. On the other hand it also reduces the volume available for the stator, hence the possibility to have large slots. The airgap radius also affects the solid strength of the rotor as a larger radius gives higher peripheral speed and therefore higher centrifugal forces.

The inner radius influences the rotor flux paths in terms of saturation and cross-saturation. Smaller radius results in bigger flux paths and less cross saturation effects [12]. A smaller radius can on the other hand increase the machine weight.

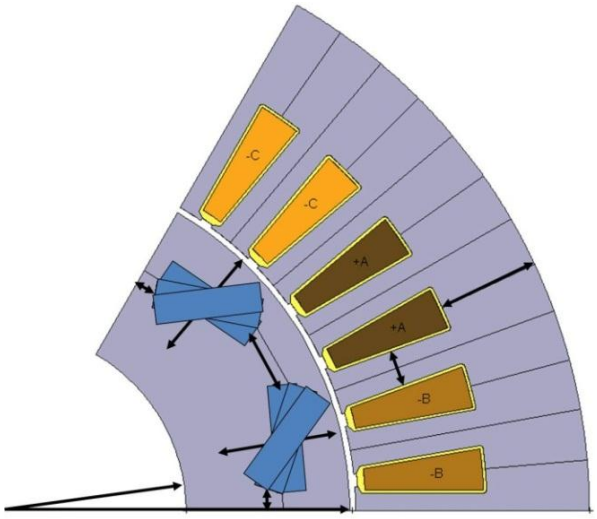

Figure 3.3 Examples of design parameters affecting the machine characteristics

The PM position and angle is altered with consideration to cross saturation effects, saliency and reluctance torque. In combination with the stator teeth it also influences the amount of cogging in the machine. The size, mutual PM distance within a pole and distance between poles influence the flux linking with the stator and hence the electromagnetic torque.

Air cavities are introduced to create flux barriers between poles and to emphasize the saliency or difference between *x*-inductance (L_{sx}) and *y*-inductance (L_{sy}). The manufacturability when inserting the magnets and the solid strength is also considered when designing the flux barriers. The difference in flux leakage with and without flux barriers can be seen in Figure 3.4. In the prototype, the air pockets are filled with epoxy.

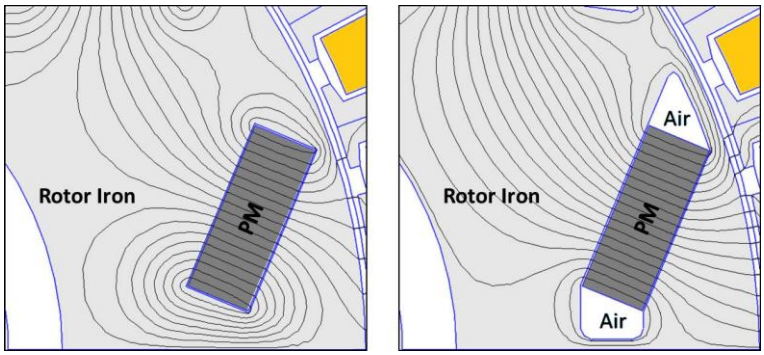

Figure 3.4 Flux leakage without (left) and with (right) flux barriers in terms of air pockets around the magnets

The PM material is selected to give a sufficiently large safety margin to overheating. Remanence and coercivity is also considered to give a large magnetic strength and sufficient torque rating. Due to the higher ratings of transverse field die pressed (TP) magnets compared to axial field die pressed (AP) magnets [13] pp. 879-880, TP is selected despite a higher cost. This is motivated by that the cost difference is driven by the manufacturing procedure and that manufacturing related cost is more likely to go down in the future. Since the PM raw material cost is high the consideration is to utilize the available material as much as possible.

Stator design

The stator yoke thickness is investigated in terms of achieving the desired overload capability as well as keeping a reasonable current level in the slots. Since the torque is almost proportional to the slot current, deeper slots that can contain more current results in higher torque for a set slot

width and current density. As can be seen in Figure 3.3, deeper slots with a set airgap radius can be achieved by reducing the yoke thickness. This will on the other hand reduce the width of the flux path which influences negatively on the over load capability. A thinner stator yoke means higher flux density and is therefore more easily saturated. The consequence of saturation is that the torque no longer increases linearly with the current. It will also reduce the peak power at higher speeds as the epicentre of the stator flux linkage modulus ellipses (introduced in Figure 3.2) moves to the right. This means that the MFPT-curve is reached at lower speeds and hence limits the torque and therefore also the power. The yoke thickness together with the airgap radius will also affect the length of the teeth.

The tooth width will also affect the flux path as well as available area for the conductors in the stator slots. Wider teeth mean lower flux density which affects the location of the stator flux linkage modulus ellipses epicentre on the negative *x*-axis. In combination with the length of the teeth (set by the yoke thickness) the mechanical integrity of the teeth needs to be considered. A rule of thumb according to the machine manufacturer[5] is to have a 6:1 relation between tooth length and width. Narrow slots might be beneficial for dissipating heat from the windings as it means a shorter distance from the hotspot to the stator core. The influence of the yoke and tooth width on the machine performance can be seen in Figure 3.5 where four different designs and how the result is affected are presented. As can be seen large slots results in high torque, but suffers from reduced peak power above base speed. The two designs that seem to be able to fulfil the requirements are either long-slender or short-thick slots. They give large enough flux paths to provide the required power. The slots are also large enough to produce the desired torque.

The corner between the teeth and yoke can be rounded with a radius. This allows for a slightly higher fill factor and facilitates when winding the machine. It is also beneficial for the mechanical strength of the teeth as a radius reduces the mechanical stress on the transition. The drawback is a slightly smaller slot area for a given yoke thickness and tooth width.

By varying the slot opening and shape of the tooth tip in combination with the PM position, the cogging can be reduced. The purpose with the tooth tip is also to keep the slot wedge and eventually the windings in position. Flux leakage from the PM not linking with the windings is also affected by the tooth tips and slot openings.

[5] Folkhammar, Jan (Bevi AB).

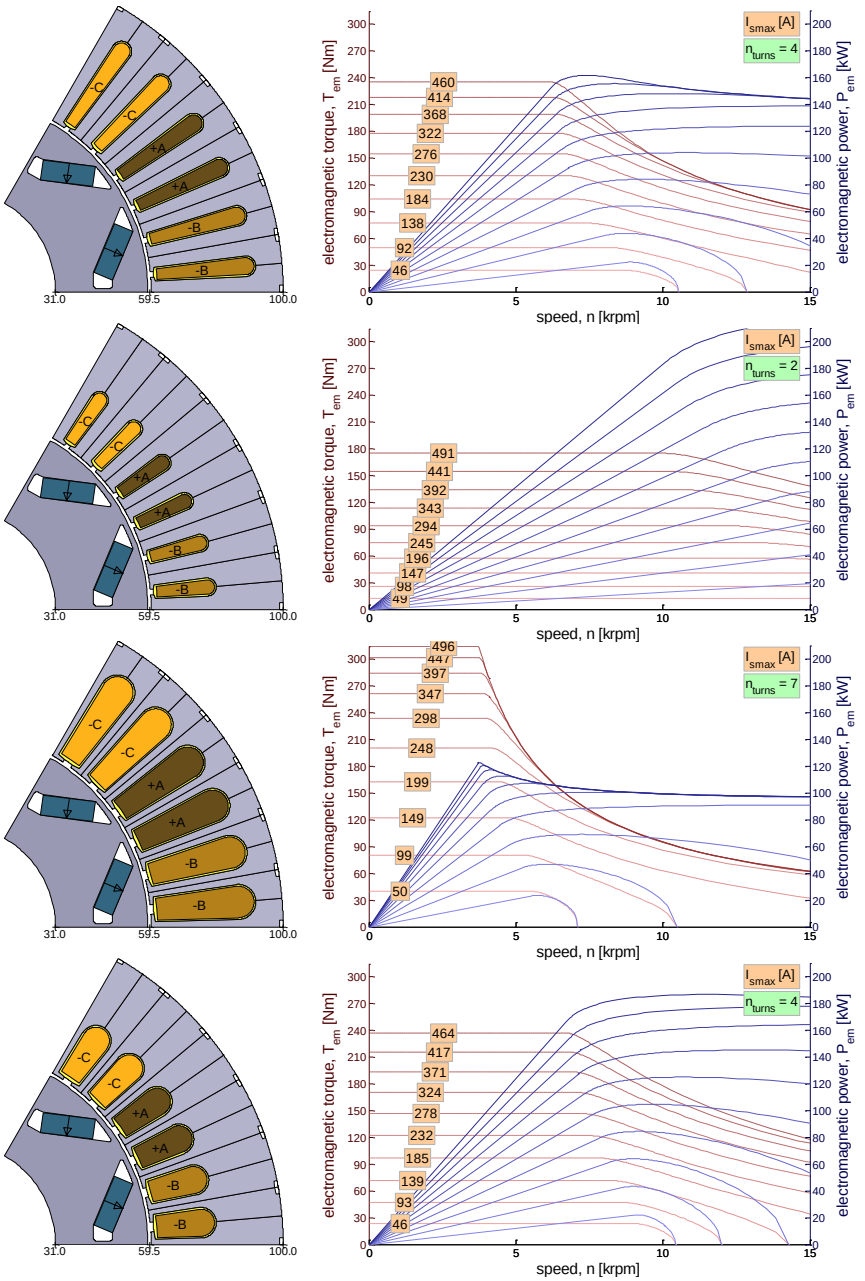

Figure 3.5 Four machine designs with similar rotor geometry but different slot configurations and corresponding torque-speed and power-speed curves

The number of slots per pole and phase is chosen to give a smooth wave form in the induced voltage. This is achieved with fractional pitch windings [2] and in order to utilize the available space around the machine, distributed in multiple slots. Distributed windings will also keep the hot spot temperature lower as the amount of current in each slot is lower for a constant current density. Integer slots versus double layer windings are considered as it affects the slot fill factor. There might also be a slightly higher risk for phase to phase faults when two phases share the same slot.

The number of stator turns; hence the number of turns completed by the coil in each slot is introduced when post processing the simulation results. With a fixed current density in the slots, multiple turns means that the current is divided into multiple conductors and therefore is lower compared to if a single turn is used. A higher number of turns means higher flux linkage hence induced voltage. A higher flux linkage should also mean higher torque. However, for a fixed current density in the slots, the current in the coil is reduced in the same amount as the increase of flux linkage. The result is therefore a torque that is fairly unaffected of the number of stator turns. The assumed current density and number of turns is also affecting the rating of the power electronics as this sets the current in the system. The number of turns, n_{turns} in each of the four examples in Figure 3.5 is included in the figure. The reason for why the designs with large slot areas have higher number of turns is that the current density is constant in all simulations. This means that the number of turns is used to adjust the current to a reasonable level.

Finally a design is chosen based on the findings from the design process described above. The suggested design and corresponding torque-speed and power-speed curves from the first round of simulations is presented in Figure 3.6. As can be seen the slots are rather long and slender, hence similar proportions as the uppermost alternative in Figure 3.5, giving a reasonably constant peak power above base speed. The slots are also wide enough to provide sufficient peak torque.

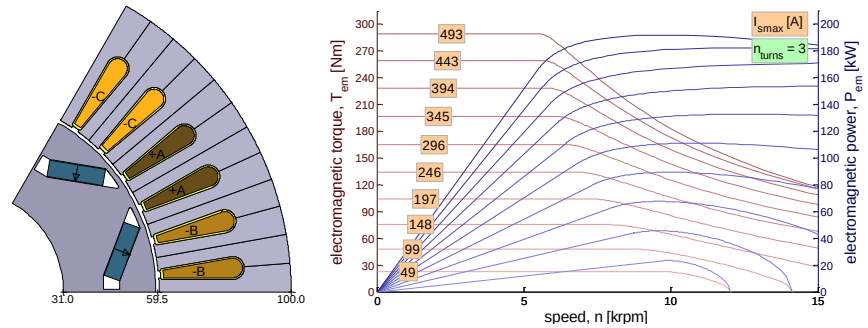

Figure 3.6 Proposed design prior design for manufacturability

Design for manufacturability

The suggested design (Figure 3.6) is reviewed together with the machine manufacturer. Based on the feedback, some design modifications are done.

In order to facilitate the insertion of the windings into the slots the slot openings are made wider. In connection to this the slots need to be wider as well to keep the tooth tips sufficiently large to encase the windings. This affects the tooth width and in order not to affect the flux paths too much, tapered teeth are introduced. Hence the tooth is made slightly wider around the base compared to closer to the tip. The magnet width and position is shifted somewhat to maintain a low cogging torque also with the re-designed tooth tips. The total amount of PM material is kept constant by increasing the magnet thickness correspondingly.

An airgap is introduced around the magnets. This is needed due to tolerances in laser cutting (for the prototype) or punching (for serial production) and in the PM manufacturing. A small distance is also needed just in order to insert the magnets in its pockets. The iron bridges between the PM cavities and the airgap (d_a in Figure 3.8) are made slightly thicker than originally intended. This is to obtain a safety factor for when to grind the outer diameter of the rotor after stacking the laminations in the rotor.

The assumed active length is somewhat reduced in order to fit the end windings within the 400 mm total machine length. The magnets are made squared (16 mm x 16 mm x 6 mm) to prevent potential faults when mounting them into the rotor. The width and therefore also the length is set from the FE-simulations. Should the magnets be rectangular with a small difference in length and width, it can be hard to detect the direction in which the magnets should be inserted. Too short magnets can be more

difficult to mount and too long magnets reduce the number of discrete lengths that can be achieved if the machine should be redesigned to another length. Since the magnets are 16 mm long, the active length is a multiple of 16 mm. The resulting active length is 224 mm.

The resulting machine design and corresponding torque-speed and power-speed curves from the re-design are presented in Figure 3.7. As can be seen when comparing to the original design suggestion (Figure 3.6), the slots are shorter and thicker. This means that the slot area is roughly the same and hence the same torque level can be reached. When comparing to the different cases in Figure 3.5 it can be seen that the re-design looks more like the alternative at the bottom of the picture.

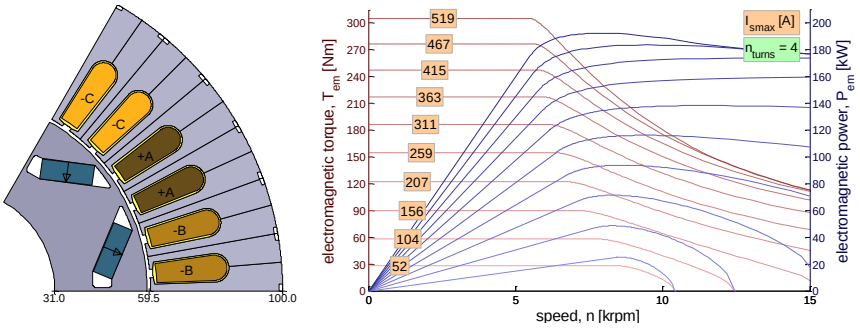

Figure 3.7 Proposed design after design for manufacturability

3.3 Mechanic stress analysis

A simple analytical check of the mechanical strength is developed and implemented in the design tool. By performing the analysis and exclude mechanically weak structures before proceeding to FEA, the computational effort is potentially reduced. Before building the prototype, the resonance frequency of the long and slender rotor is also investigated. The mechanical analyses are described in the following section.

Mechanical integrity analysis of the rotor

The magnets and the part of the rotor core located outside the magnets will be subjected to centrifugal forces when the EM is in operation. These centrifugal forces will mainly be supported by the stiff and radially oriented iron bridge between the cavities of two neighbouring magnets. From an electromagnetic perspective the bridge should preferably be infinitely thin to avoid flux leakage, but in reality the bridge width must be

sufficiently large to handle the centrifugal forces. The area A_{fe} of the part of the rotor located outside the magnets is estimated to derive a weight m_{fe} which is used as input in the analysis together with the PM size A_{pm} and weight m_{pm}. This is clarified further in Figure 3.8 were the iron bridge is marked together with the distances of interest. In order to keep a safety factor in the analysis, the assumptions made when estimating the iron mass are consistently conservative. This goes for estimating the area A_{fe} as well as using the density of iron rather than silicon steel.

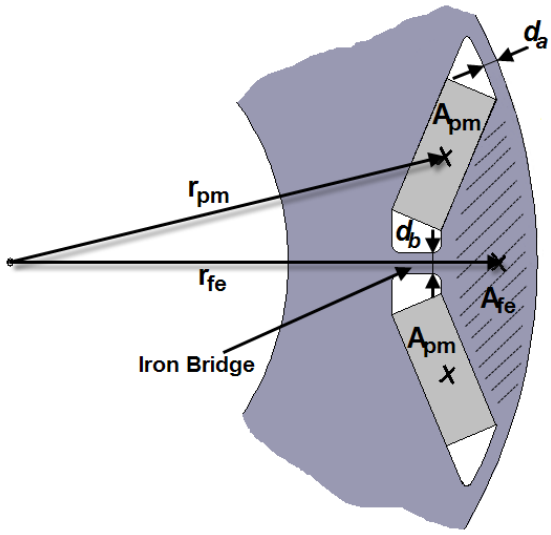

Figure 3.8 Distances of interest for calculating the mechanical integrity of the rotor

The centrifugal force F_{IB} supported by the iron bridge in Figure 3.8 due to the rotational speed ω is determined with (5). The resulting mechanical stress σ_{IB} in the iron bridge is calculated with (6), where A_{IB} is the area over which the force is applied. The contribution from the tangentially oriented bridges at the outer periphery of the rotor is expected to be small compared to the centre bridge. Therefore these are neglected from the tensile strength calculations. The neglected extra support is instead considered as a safety margin and the width d_a is rather determined by manufacturability as already described. The radii r_{fe} and r_{pm} used in (5) and the iron bridge width d_b used in (6) are defined according to Figure 3.8 and h_m is the active length of the machine.

$$F_{IB} = m_{fe} \cdot r_{fe} \cdot \omega^2 + 2 \cdot m_{pm} \cdot r_{pm} \cdot \omega^2 \quad (5)$$

$$\sigma_{IB} = \frac{F_{IB}}{A_{IB}} = \frac{F_{IB}}{d_b \cdot h_m} \quad (6)$$

Here, the safety against a single overspeeding event of the EM is considered. It is required to avoid bursting as well as significant permanent deformation of the rotor. Under elastic, reversible conditions, there will be stress concentration at the inner and outer ends of the central iron bridge, cf. the geometrical form factor K_t in [14], Ch. 33. With increased centrifugal forces, the peak stress will eventually reach the yield strength σ_{yield} of the steel lamination material. When the yield strength has been reached, the stress is not increased any further until large non-reversible deformations occur. Thereby, the effect of stress concentration is reduced. In the limit case, the entire cross section of the central iron bridge would be subjected to a mechanical stress equal to the yield strength. So, by using σ_{yield} for σ_{IB} in (6), (5) and (6) are solved for the rotational speed. This is done in (7) where ω_{max} is the rotational speed at which the yield point is reached. All designs where ω_{max} is lower than the required burst speed (hence the EM top speed plus 50% over speed) are disregarded.

$$\omega_{max} = \sqrt{\frac{\sigma_{yield} \cdot d_b \cdot h_m}{m_{fe} \cdot r_{fe} + 2 \cdot m_{pm} \cdot r_{pm}}} \quad (7)$$

Besides the previously mentioned measures for getting a safety factor in the analysis, worst case in tolerances from cutting or stamping the laminations is considered. This by correspondingly reduce the width of the iron bridge d_b. A simplification in the analysis is to exclude the epoxy resin with which the cavities around the magnets are filled at the end of the assembly. Although the possible bonding effects should add some mechanical strength, the impact of ageing due to thermal cycling is hard to estimate. The potential benefit of the epoxy resin is instead considered as an addition to the safety factor.

The fatigue stress from repeating operations up to the EM top speed is briefly investigated using the theory behind Haigh diagrams [14] pp. 288-297. The outcome is that the overspeeding requirement is tougher; hence if the rotor can handle that, the fatigue stress is covered as well.

Mechanical resonance frequency analysis

To avoid unexpected problems with mechanical resonance in the slender rotor, the natural or critical frequency ω_{crit} is investigated. For a given distance between the bearings l_b, Young's modulus for steel E_{fe}, the area moment of inertia for the shaft I, the estimated rotor mass m_r, and the relative distance from each bearing to the centre of gravity (CoG) λ_α and λ_β respectively, the natural frequency can be calculated with (8) [15] pp. 341-342. This gives the natural frequency for when the mass is concentrated at CoG. The fact that the natural frequency is slightly higher for a distributed mass such as the case with a rotor is used to make the calculation conservative. Figure 3.9 clarifies the distances used in the equation.

$$\omega_{crit} = \sqrt{\frac{3 \cdot E_{fe} \cdot I}{m_r \cdot {\lambda_\alpha}^2 \cdot {\lambda_\beta}^2 \cdot {l_b}^3}} \tag{8}$$

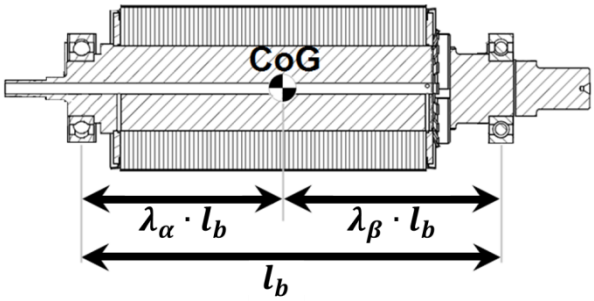

Figure 3.9 Distance between the bearings and to the centre of gravity

Assuming a worst case where the CoG is half-way down the rotor shaft (hence λ_α and λ_β both equal to 0.5) and the bearings mounted on each end of the machine (hence l_b equal to 400 mm), the natural frequency is in excess of 30000 rpm, hence outside the speed range defined previously in Table 1 on page 24.

3.4 Thermal design

The following section covers the thermal aspects in the machine design process. Finite element (FE) simulations are performed to investigate the temperature distribution in the machine. The temperature dependence and how it affects the simulation result is also investigated. Finally, two

different methods on how to implement oil cooling are presented. The first method is based on oil spray on the end windings and the second one introduces cooling channels in the stator back. Both methods are utilizing the possibility to implement direct cooling introduced by oil as coolant.

Thermal simulations

The thermal properties of the machine are investigated in 2D FE environment using an extension of the design tool used for the electromagnetic design. The simulations are based on setting a fixed boundary temperature (T_{set}) at the stator envelope surface. The underlying assumption is that the coolant can keep the boundary temperature constant disregarding the heat generated in the machine. This means that the coolant temperature has to be lower than that of the boundary temperature in the simulation. Heat in the windings is generated based on the current density and resistivity. The resistivity is calculated for the maximum temperature, hence is considered conservative.

The stator losses in the teeth and yoke are based on the flux density in the different regions at a given frequency. Losses in the rotor as well as mechanical losses are disregarded in the simulations. Consequently a safety factor is needed to make sure that the machine can handle the accruing temperatures. The assumptions done concerning the thermal FEA are defined as in Figure 3.10 and summarized in Table 2. The rather low thermal conductivity in the slot is to compensate for the fill factor and that there are slot insulation and epoxy resin present. This is based on previous experience in the department.

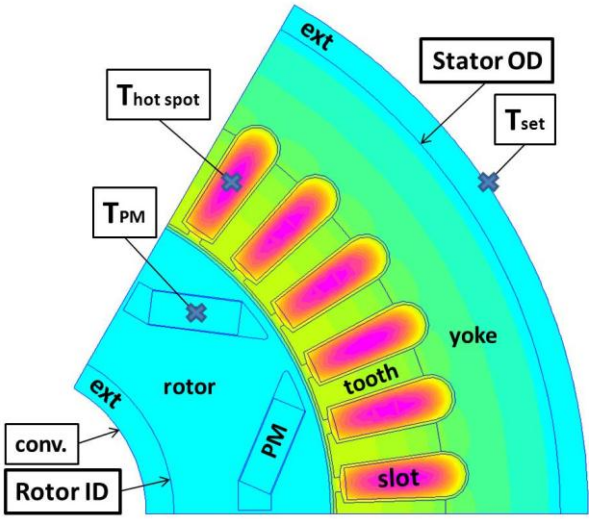

Figure 3.10 Thermal FEA elements and boundaries

Table 2 Thermal FEA definitions as defined in Figure 3.10

Materials	Thermal Conductivity [W/(m·K)]	Heat generation [kW/m³]
Yoke (Fe)	36	130
Tooth (Fe)	36	340
Slot (Cu & insulation)	0.3	840
Rotor (Fe)	36	-
PM (NdFeB)	10	-
Ext (-)	50	-
Insulation[I] (-)	0.12	-
Air[I] (-)	0.03	-
Boundaries	Convection coefficient [W/(m²·K)]	Fixed temperature [°C]
Conv.	15	-
T_{set}	-	100

[I] Not included in Figure 3.10

Investigated parameters are the PM temperature and hot spot temperatures, included as T_{PM} and $T_{hot\ spot}$ in Figure 3.10 above. The hot spot temperature is interesting both in terms of absolute temperature and also as the temperature difference to the set envelope surface temperature. The

absolute temperature is important for dimensioning the temperature class in the winding. The temperature difference is interesting since it indicates whether the coolant temperature can be increased. This could be advantageous from a system point of view.

The PM temperature influences the remanence and coercivity and hence the machine performance. The PM data used so far in the electromagnetic FEA is valid for room temperature. A temperature dependent reduction in the magnet remanence and coercivity is added in the design tool. This makes it possible to run simulations with different (higher) PM temperatures in the electromagnetic FEA. The temperature from the thermal FEA is used as an indication on the temperature range in the machine.

Temperature dependence

The PM temperature influence on the remanence and coercivity and the resulting reduction in magnetic flux linkage and EM performance is studied. A brief study of the temperature influence in the stator iron is also performed.

PM temperature dependence

The data sheet of the magnets has information of the field strength in terms of the remanence B_r and coercivity H_c at room temperature (20°C). The relation between the remanence and coercivity can be expressed in BH-curves as shown in Figure 3.11. The coercivity is divided into intrinsic H_{cI} and normal H_{cB} field strength. The intrinsic coercivity expresses the field strength internally in the magnets and is hardly affected by external fields before reaching demagnetization. Once demagnetization is reached the magnet is permanently damaged. The normal coercivity gives, along with the remanence information on how the magnet behaves in a magnetic circuit, such as an electric machine. The operating point when exposed to external field follows the normal curve in Figure 3.11. The relation $B=\mu \cdot H$ between B_r and H_{cB} is defined by the permeability, $\mu=\mu_r \cdot \mu_0$. Here, μ_r and μ_0 are the relative permeability of the magnet material and the permeability of free space, respectively. The relation between B_r and H_{cB} means that μ can be seen as the slope of the normal BH-curves in Figure 3.11.

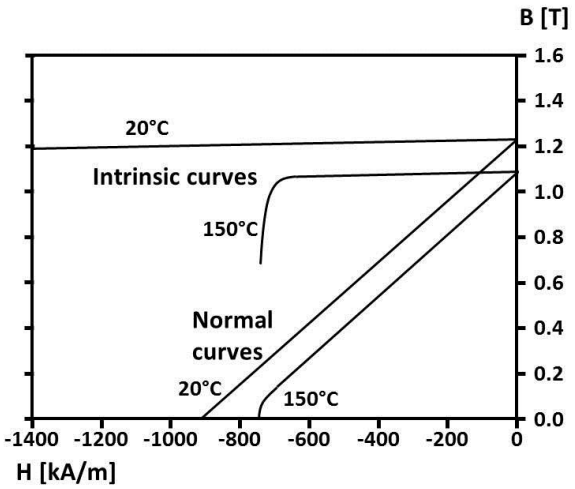

Figure 3.11 Principle magnet characteristics with intrinsic and normal BH-curves for 20°C and 150°C

The remanence and coercivity are affected by temperature. This can be described by the reversible temperature coefficients *RTC* for the magnet grade. The *RTC* is the relative change in magnitude as function of PM temperature increase ΔT above room temperature (20°C) and is expressed in [%/°C]. $RTC(H_{cJ})$ defines the sensitivity of demagnetization with increasing temperature. Demagnetization occurs when the operating point passes the knee point in the BH-curve. As the temperature increases, the knee moves closer to origin. How much is determined by $RTC(H_{cJ})$. In Figure 3.11 the knee can be seen at approximately -750kA/m in the 150°C curves. $RTC(B_r)$ defines the change in remanence. Since the permeability μ hardly is affected by the temperature increase, the slope can be considered constant regardless of (normal) operating temperature. This means that in the normal operating range, $RTC(B_r)$ can be applied on B_r as well as H_{cB} according to (9) and (10). Typical values for $RTC(B_r)$ and $RTC(H_{cJ})$ are -0.11%/°C and -0.60%/°C, respectively [3], pp. 42.

$$B_r = B_r(20°C) \cdot \left(1 + \frac{RTC(B_r) \cdot \Delta T}{100\%}\right) \tag{9}$$

$$H_{cB} = H_{cB}(20°C) \cdot \left(1 - \frac{RTC(B_r) \cdot \Delta T}{100\%}\right) \tag{10}$$

The influence of increased PM temperature ΔT in the machine model is investigated by modifying the remanence and the coercivity according to (9) and (10), respectively. The value for $RTC(B_r)$ for the magnet grade used in the prototype is obtained from the magnet supplier[6]. The modified remanence and coercivity are used as input when defining the magnet material in the simulation model.

The resulting reduction in flux linkage is presented in Figure 3.12. As can be seen the flux linkage is reduced with around 10% at 100°C compared to room temperature. The influence on the machine performance is presented later in section 3.7.

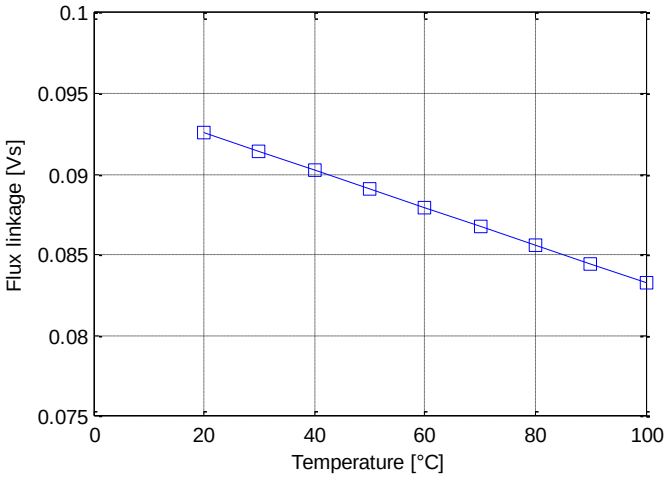

Figure 3.12 Stator flux linkage (rms) as a function of magnet temperature

Iron core temperature dependence

The temperature dependence of the electric steel is also considered. According to [16]-[18], the relative permeability of iron (μ_{fe}) increases slightly with increased temperature at low field strength. This is investigated analytically based on the simplification presented in Figure 3.13. The relation between the induced current and the magnetic flux density (B) in the iron (fe), airgap (d) and magnets (pm) can be calculated according to (11) where the permeability and permanent magnet flux is

[6] Vacodym 863 TP
http://www.vacuumschmelze.com/en/products/permanent-magnets-assemblies/permanent-magnets/nd-fe-b/vacodym.html

denoted with μ and B_{0pm} respectively. Using the assumption introduced in (12), the total flux in the magnetic circuit is calculated according to (13). By assuming zero current together with relevant numbers on all parameters in (13) and changing the relative permeability of iron it can be concluded that a duplication of the permeability results in less than 1% difference in the resulting flux density.

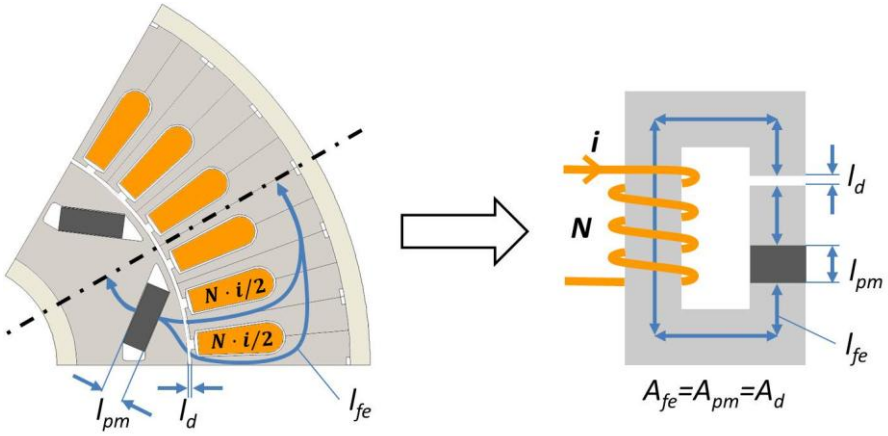

Figure 3.13 Simplification of the magnetic circuit in the electric machine with definitions of the lengths (l_{fe}, l_d and l_{pm}) and areas (A_{fe}, A_d and A_{pm}) for the flux paths together with the current (i) and number of turns (N) in the coil

$$N \cdot i = H_{fe} \cdot l_{fe} + H_d \cdot l_d + H_{pm} \cdot l_{pm} = \\ = \frac{B_{fe}}{\mu_0 \cdot \mu_{fe}} \cdot l_{fe} + \frac{B_d}{\mu_0} \cdot l_d + \frac{B_{pm} - B_{0pm}}{\mu_0 \cdot \mu_{pm}} \cdot l_{pm} \quad (11)$$

$$A_{fe} = A_d = A_{pm} \Rightarrow B_{fe} = B_d = B_{pm} = B \quad (12)$$

$$B = \frac{\mu_0 \cdot N \cdot i + \frac{B_{0pm} \cdot l_{pm}}{\mu_{pm}}}{\frac{l_{fe}}{\mu_{fe}} + l_d + \frac{l_{pm}}{\mu_{pm}}} \quad (13)$$

The analytical result is also backed up with FE simulations, where an exaggeratedly modified permeability still only gives a marginal difference in the result. The conclusion from investigating the temperature dependence of the iron permeability is that the influence is so small so the effects can be neglected when investigating the machine performance.

Oil spray on end windings

The first cooling concept is implemented as oil spray on the end windings. Running at high current density makes the copper losses dominating. Improved cooling ducts in the stator housing are still suffering from thermal resistance implied by the thermal barriers between the windings inside the slots and the actual cooling ducts. The heat generated in the copper windings is first conducted through the varnish/epoxy/air mixture in the slot. Then through the slot insulation to the laminated stack and pass the interface towards the housing before reaching the cooling ducts. All together this results in a long way for the heat flow to pass. With oil spray on the end windings the main advantage is that the coolant is applied directly onto the copper windings. The varnish/epoxy/air mixture in the slots results in poor thermal transmittance perpendicular to the wires. In axial direction the heat is conducted with high thermal conductivity along the copper wires. This makes cooling on the end winding effective since it induces a heat flow from the center of the machine to the end windings. Furthermore, distributed windings mean rather large end windings hence a good opportunity to achieve good cooling.

Cooling on the end windings are implemented based on previous design work in the department [8]. Oil is led into the shaft and directed via radial channels on each side of the rotor to the end windings. As the rotor rotates, the oil is distributed around the inside of the end windings. The concept is demonstrated in Figure 3.14. Since the thermal simulations are done in a 2D FE environment it is difficult to fully cover the 3D effects introduced by the end winding oil spray. A coarse approximation on the heat dissipation capability can be done by estimating the surface area of the end windings and the thermal properties of the oil-air mixture together with different oil flow rates. This is however not included in this thesis and it is therefore important to keep a confidence interval when selecting material for the prototyping. Sufficient heat dissipation is instead expected based on preliminary test results at the department and backed up by [19] pp. 102 and [20]. Similar solutions are well known in gearboxes, e.g. as in [21].

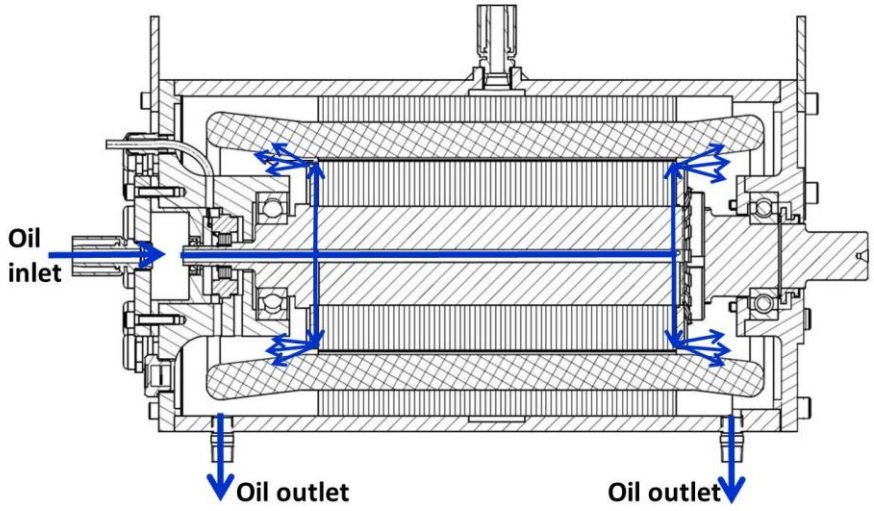

Figure 3.14 Oil cooling implementation on the end windings

Oil channels in the stator back

A secondary cooling concept is implemented in the stator back. During the manufacturing of the stator laminates (by stamping or laser cutting) slots are made in the outer periphery, exemplified in Figure 3.15. These outer slots form channels running in axial direction along the envelope surface. In order to minimize the influence on the magnetic flux paths, the oil channel slots are located directly outside the stator teeth. With 36 teeth this results in 36 oil channels around the periphery. Simulations are done with a number of different depths and widths as defined in Figure 3.15 to investigate the influence of the oil channel slots on the electromagnetic performance. As long as the channel depth is kept reasonably small (below approximately ¼th of the yoke thickness) the difference in the simulation result is barely noticeable. The difference is actually so small that it just as well can be caused by a different mesh size in the different simulations. The geometrical properties are instead set with respect to thermal and manufacturing aspects.

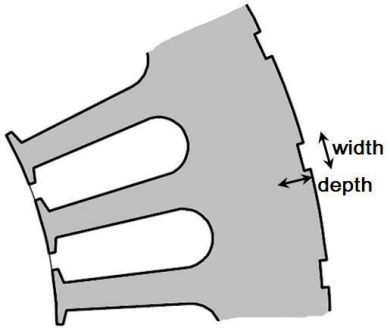

Figure 3.15 Oil channel slots implemented in the stator back

The maximum width of the oil channels is limited by the manufacturing. The contact surface between the housing and the stator back has to be sufficiently large to prevent the stator from rotating inside its housing. In a prototype this risk can be removed by introducing a wedge between the stator and housing. This is however not suitable for serial production since it would introduce a potential reliability risk if forgotten during the assembly. The limit according to the prototype manufacturer[7] is approximately 25% of the total periphery, hence around 4 mm with 200 mm OD and 36 channels.

Generally when implementing forced cooling in channels turbulent flow is desired. Although the pressure increases, the thermal convection is improved compared to that of laminar flow. In order to optimize the system efficiency both heat transfer and pressure drop need to be considered. The break point for laminar flow is when the dimensionless Reynolds number (Re_D) is below ≈2300. From ≈2300 up to ≈5000-10000, the flow is in a transition state and at sufficiently high Reynolds number the flow becomes turbulent [22]. The Reynolds number is calculated according to (14) where u_m is the mean velocity in the channels, v is the kinematic viscosity and D_h is the hydraulic diameter, defined in (15) as given in [22] Ch. 8-8. Width and depth in (15) are defined in Figure 3.15.

$$Re_D = \frac{u_m \cdot D_h}{v} \tag{14}$$

$$D_h = \frac{4 \cdot width \cdot depth}{2 \cdot (width + depth)} = \frac{2 \cdot width \cdot depth}{width + depth} \tag{15}$$

[7] Edström, Lennart (Bevi AB).

Oil typically has a relatively high viscosity and as seen in (14) the viscosity is inversely proportional to the Reynolds number. Consequently this means that either a high velocity or a large channel area is required to obtain turbulent flow. By doing a quick analysis with an oil flow of 15-20 litres per minute it is concluded that the Reynolds number ends up far below the threshold between laminar and transition case. The outcome is that turbulent flow not will be achieved in the oil channels. With this knowledge the Nusselts number, *Nu* hence the ratio between the convective and conductive heat transfer coefficients is used to determine the width-depth ratio. Since the Nusselts number increases with a larger width-depth ratio and a higher Nusselts number results in better heat transfer, a small depth is chosen, cf. [22] Ch. 8-8. The depth is set to 1 mm, limited by the fact that a too thin oil channel will prevent the oil from passing through. The width is as stated above limited by keeping a sufficiently large contact area between the stator back and the motor housing. The rather rough wall structure composed by the stacked laminations could possibly also improve the heat transfer from the stator back to the oil. The cost will be an increased pressure drop along the channel.

A circumferential groove in the housing halfway down the active length distributes the oil into the axial channels. This means that the coldest oil is applied in the middle of the machine were highest temperature is expected. As the oil percolates towards both ends of the machine, the temperature is expected to be evenly distributed in both axial ends. The oil eventually leaves the stator to the end winding accommodation and finally leaves the motor through the same outlets as the end winding oil. The concept is demonstrated in Figure 3.16. Since the oil viscosity is temperature dependent, the back pressure seen in the channels will differ with temperature leading to a self-regulating system with higher flow rate when the temperature increases. This self-regulating system is however not investigated further in this thesis.

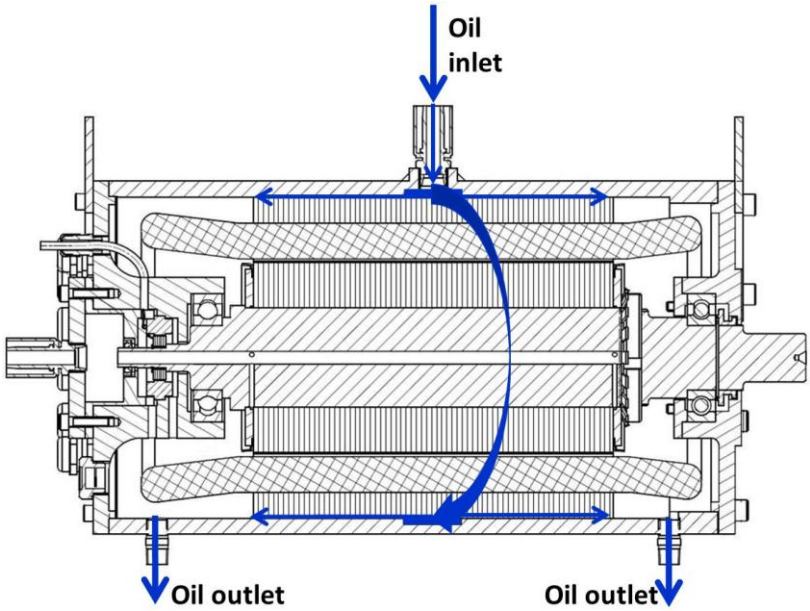

Figure 3.16 Oil cooling implementation in the stator back

A simple analytical study is performed to investigate of the heat removed through the oil channels in the stator back. The heat transfer coefficient h [W/m²·K] is calculated for fully developed flow according to (16) where the Nusselts number Nu is set by the width/depth ratio, λ is the thermal conductivity of the oil [W/m·K] and D_h is defined earlier in (15). By assuming a uniform wall temperature ϑ_W and an average oil or bulk temperature ϑ_B the heat flux q [W/m²] is calculated according to (17). The final assumption is that the heat is transferred through the three surfaces towards the stator laminations but not via the outer wall towards the housing. This gives a total cooling area according to (18) where N_C is the number of channels. Finally, the amount of power Q removed through the oil is calculated with (19). All input and results are presented in Table 3.

$$h = \frac{Nu \cdot \lambda}{D_h} \tag{16}$$

$$q = h \cdot (\vartheta_B - \vartheta_W) \tag{17}$$

$$A_{cool} = active\ length \cdot (width + 2 \cdot depth) \cdot N_C \quad (18)$$

$$Q = q \cdot A_{cool} \quad (19)$$

Table 3 Results from the analytical investigation regarding heat dissipation through oil channels in the stator back

Description	Name	Value	Unit
Nusselts number[I]	Nu	4.44	-
Thermal conductivity of oil[II]	λ	0.13	W/(m·K)
Bulk/Oil temperature[III]	ϑ_B	80	°C
Wall temperature[III]	ϑ_W	100	°C
Depth	-	1e-3	m
Width	-	4e-3	m
Heat transfer coefficient[IV]	h	416	W/(m²·K)
Heat flux[IV]	q	-8300	W/m^2
Active length	-	224e-3	m
Number of oil channels	N_C	36	-
Cooling channel wall area	A_{cool}	48e-3	m^2
Total heat dissipation[IV]	$\boldsymbol{Q}$	**-360**	**W**

[I][22] pp. 129 [II]Castrol Syntrans@80°C [III]Assumption [IV]Calculated

The result from the analytical investigation is intended to indicate the magnitude rather than giving an exact answer. The assumed constant wall temperature is for example a rather blunt estimation. The alternative in the analytical analysis is to assume a constant heat flux along the cooling channel while the reality really is somewhere in between. On the conservative side is that the entrance region, where a higher Nusselts number results in higher heat dissipation is disregarded in the calculations. The fourth cooling channel wall, towards the housing, is most likely also contributing somewhat to the heat removal. Although being considered with care it is observed that the heat dissipation through the oil channels can cover part of the expected iron losses presented later in Figure 3.34.

3.5 End winding selection

The end winding selection is made with focus on minimizing the extruding end winding length. A number of different end winding configurations are reviewed and in consultation with previous experience from the machine manufacturer two configurations are chosen and test wound. The left hand

side of Figure 3.17 shows integer slot winding 1-6 and the right hand side shows double layer winding 1-7, 2-6. Principle sketches of these two configurations can be seen in Figure 3.18 and Figure 3.19. The double layer winding configuration means that two different phases are sharing the same slot at some slots (number 2, 4, 6, 8 etc. in the figures). This makes it necessary to increase the amount of insulation in these slots since two different phases need better mutual isolation than two turns in the same phase. The outcome is a potentially lower fill factor since a larger part of the slot will contain non conducting material. The test windings result in a slightly smaller end winding length for the integer slot winding. This, together with the potentially higher fill factor are the motivating factors for choosing the integer slot configuration.

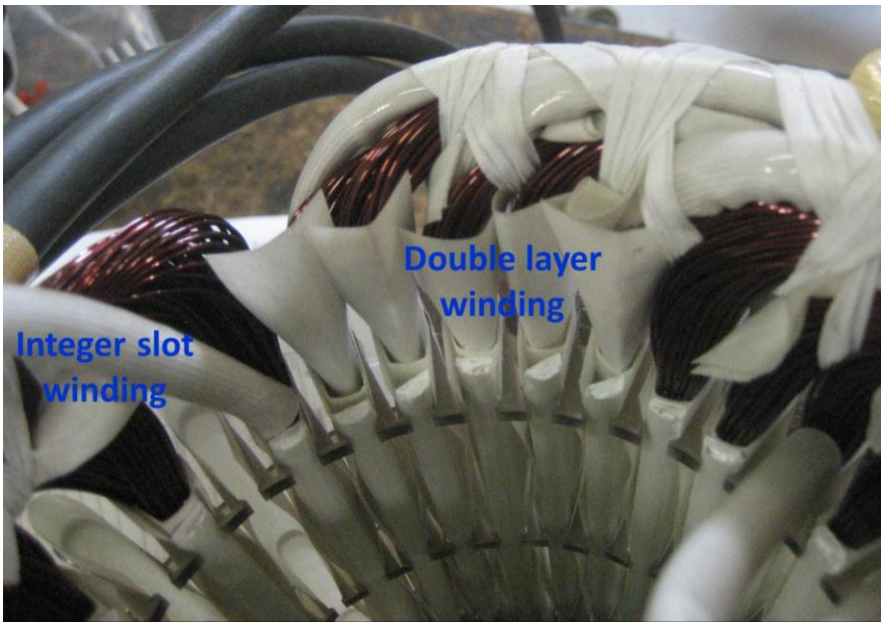

Figure 3.17 Machine dummy wound with both integer slot winding and double layer winding used for evaluating extruding end winding length

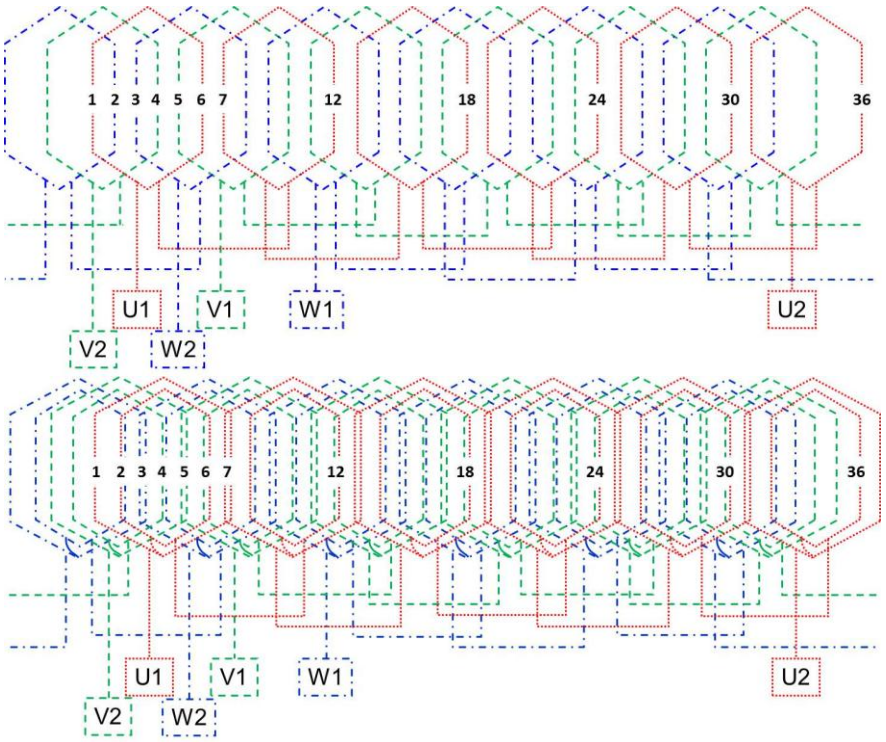

Figure 3.18 Principle sketch of an integer slot 1-6 winding (upper) and a double layer 1-7, 2-6 winding (lower)

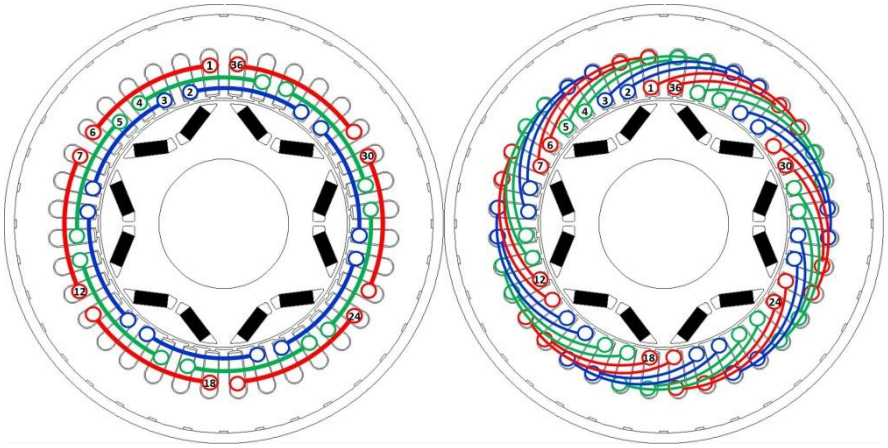

Figure 3.19 Principle sketch of an integer slot 1-6 winding (left) and a double layer 1-7, 2-6 winding (right)

3.6 Skewing

As mentioned previous in the chapter, some focus is directed towards reducing the torque ripple in the machine. The torque ripple is studied by looking at the torque as function of rotor position for a number of different loading points. This can be seen in Figure 3.20 where the colour coding is defined by the load map in the upper right corner (compare with Figure 3.2) The amplitude of the torque ripple is presented in the diagram in Figure 3.21. Although the torque ripple presented in Figure 3.22 is in the range of 5-7% in a major part of the load map, the torque ripple at continuous loads (lower right corner in the graph) still is considered rather high.

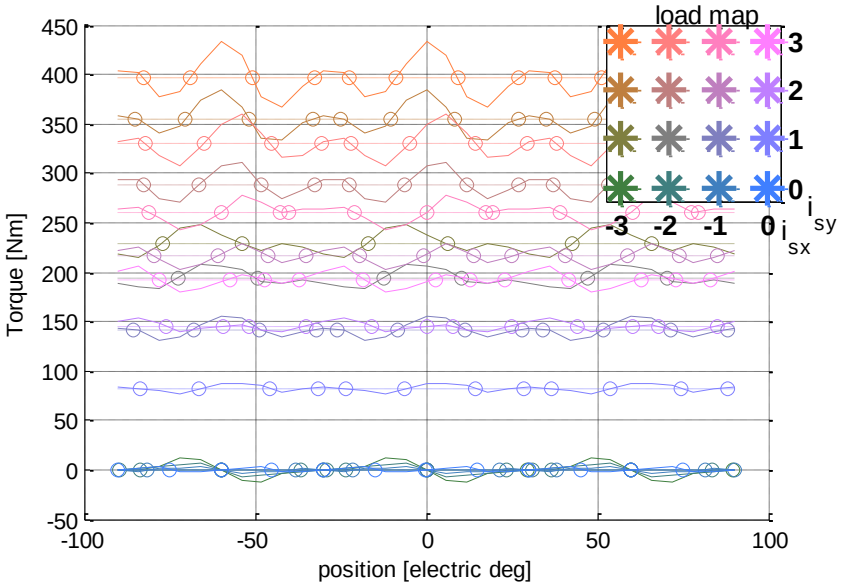

Figure 3.20 Torque as function of rotor position at 16 different loading points as defined in the load map in the upper right corner

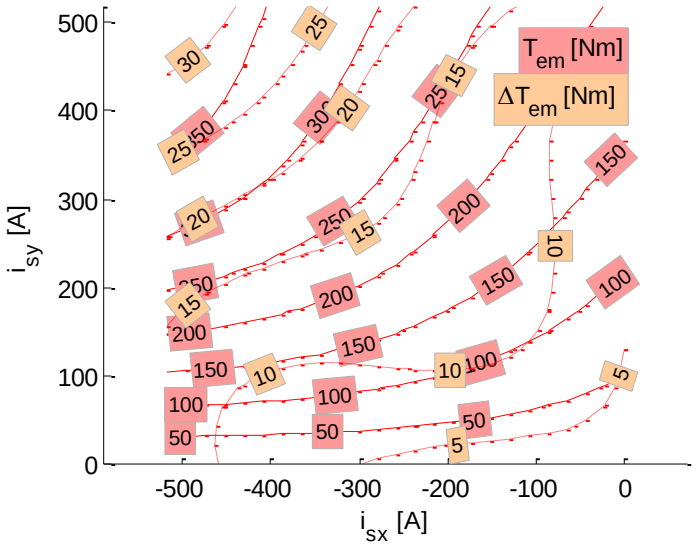

Figure 3.21 Torque T_{em} and torque ripple ΔT_{em} as functions of i_{sx} and i_{sy}

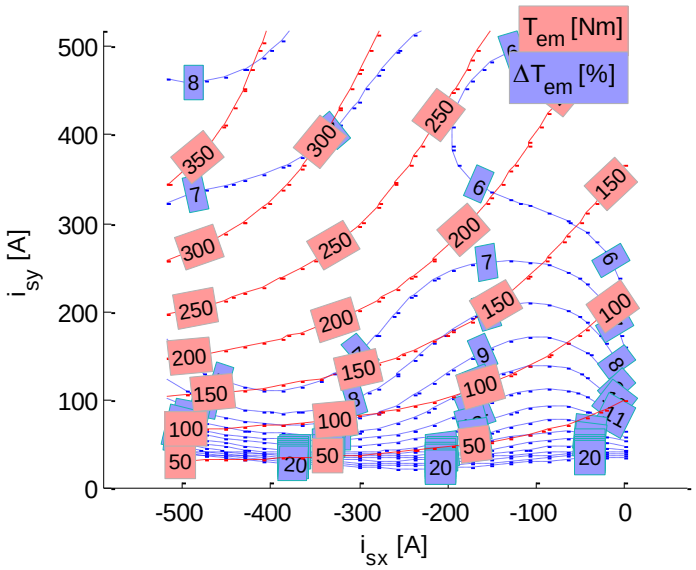

Figure 3.22 Torque T_{em} and torque ripple ΔT_{em} per cent as functions of i_{sx} and i_{sy}

In order to reduce the torque ripple and also noise and vibrations, skewing of the stator is investigated. Skewing means that the stator or rotor is twisted, or skewed by an angle α. Since the magnets have a specific length, skewing of the rotor has to be made in discrete steps for a PM machine. Since this complicates manufacturing even more than skewing the stator, this project only considers skewing in the stator. The angle α is settled by the angle between two adjacent stator teeth according to Figure 3.23. The result is reduced harmonics to the expense of a slightly reduced fundamental signal. The magnitude of the reduced signal can be estimated by assuming that the stator consists of a large number of small sections, each linking with the sinusoidal rotor flux. With skewing, each sine-wave is slightly displaced resulting in a slightly scattered peak. The average of the scattered signal can be used to establish the skewing factor k_{sh} as the reduction of the fundamental signal [23]. This is exemplified in Figure 3.24.

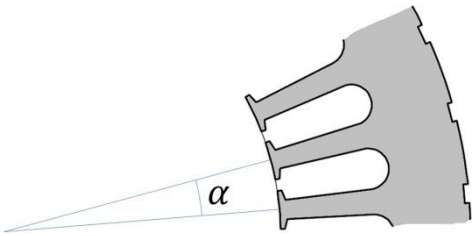

Figure 3.23 Skewing angle α between two adjacent stator teeth

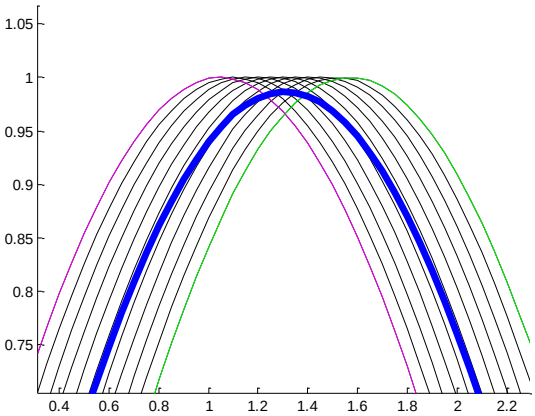

Figure 3.24 Illustration of how the skewing factor can be derived as the peak value of the average of a (infinite) number of shifted sine-waves

The skewing factor for different harmonics can also be obtained with (20) for the h_a^{th} harmonic and the skewing angle α in electrical degrees expressed in radians [2], pp. 87.

$$k_{sh} = \frac{sin\left(\frac{h_a \cdot \alpha}{2}\right)}{\frac{h_a \cdot \alpha}{2}} \tag{20}$$

Due to the rather small torque reduction (1.14% with 30° skewing angle in electrical degrees) together with preliminary simulation results indicating a margin to the peak torque requirement, it is decided to implement skewing on the prototype.

Since the simulations are performed in a 2D FE environment it is not possible to study the effect of skewing directly in the simulations. Instead the post simulation code is modified to further investigate the influence of skewing on the torque and torque ripple. This is done by dividing the machine into a number of sections, each slightly shifted towards the next. An obvious result is that if the rotor magnets are located opposite a tooth in one end of the machine it will be located opposite a slot opening in the other end. Another consequence is that the i_{sx} and i_{sy} currents will not look the same along the machine length. If the current is controlled to a certain combination in the center of the machine, this results in a deviation in the current towards both ends. This is visualized in the diagram in Figure 3.25 where the currents in the center of the machine are set to i_{sx}= -1 and i_{sy}= 2. When moving towards both ends of the machine, the current moves along the sector in the figure. The iso-torque lines plotted in the background of Figure 3.25 help explaining how the torque contribution varies along the machine.

The current vector exemplified in Figure 3.25 (i_{sx}= -1 and i_{sy}= 2) is also plotted as function of rotor position in Figure 3.26. In this graph the dislocation of the magnet in one side of the machine compared to the other side is included as a shift of the torque along the rotor position. This is seen as leaning ridges when moving up in the figure through the different torque curves. Included in Figure 3.26 is also the original torque curve as it would have looked if the stator had not been skewed, as well as the new torque contribution as it looks with skewing. The overall result is presented in Figure 3.27 and when comparing with Figure 3.20 it can be seen that a considerable improvement of the torque ripple is achieved.

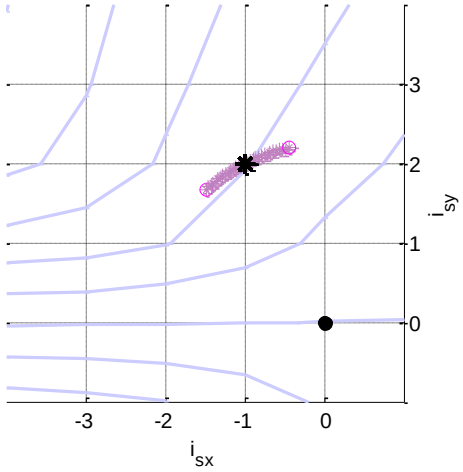

Figure 3.25 Illustration of how skewing affects the applied current vector along the machine with iso-torque curves in the background

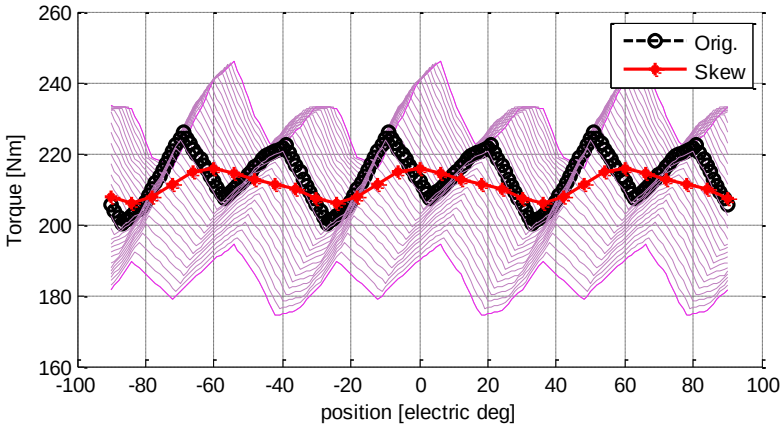

Figure 3.26 Torque contribution from a number of different sections of the machine when skewing applied to the stator including the original torque contribution and the new skewed torque contribution

Another side that needs to be considered with skewing is the manufacturing aspect. Leaning slots might complicate the winding process of the machine hence increase the manufacturing time and therefore cost. In this case however with a rather long and slender machine design the skewing is barely noticeable when working with winding the stator.

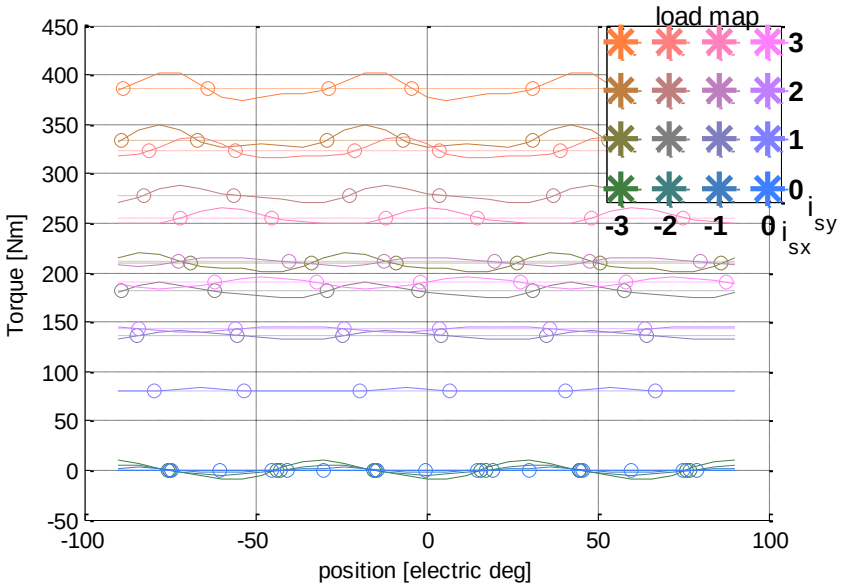

Figure 3.27 Torque as a function of rotor position at 16 different loading points as defined in the load map in the upper right corner with skewing in the stator

3.7 Machine characteristics

This section presents the simulation results from the machine design process taking the input presented in previous sections in the chapter into consideration. Flux and torque are presented as functions of rotor position as well as loading in terms of *x*- and *y*-currents. The simulation results are also used to extract torque-speed maps and a first estimation of the efficiency map with consideration to the stator losses only.

The flux as function of rotor position is presented for one of the phases in Figure 3.28. The different curves all represent a load case, from 0 to 3 times nominal current in *y*-direction and from 0 to -3 in *x*-direction. Hence in total 16 load cases according to the load map in the upper right corner of the figure. As can be seen the four cases when i_{sy} is zero have their peaks when the rotor position is at zero degrees, hence when the PM flux links the most with phase A. In the 12 other load cases where an i_{sy} current is applied, the flux linkage peak is shifted accordingly. Besides giving the induced voltage for different frequencies, the graph in Figure 3.28 is also used later on when comparing the temperature measurements with the simulation results at a number of different temperature inputs.

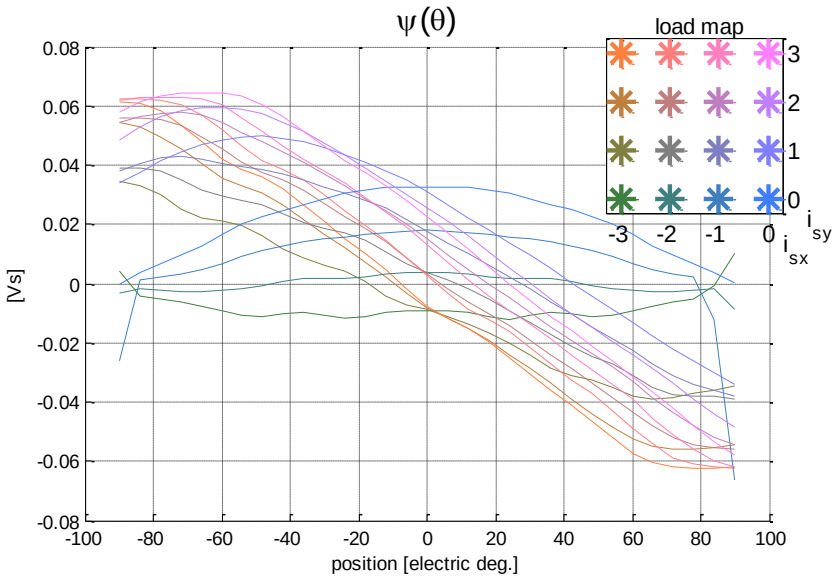

Figure 3.28 Stator flux linkage in phase A as a function of rotor position at 16 different loading points according to the load map in the upper right corner

The flux is divided into *x*- and *y*-components which are presented as functions of i_{sx} and i_{sy} currents in Figure 3.29. The total flux as a function of i_{sx} and i_{sy} is seen in Figure 3.30. The upper half of the typical ellipse shaped iso-flux lines can be seen with epicentre around 325 A in negative *x*-direction. When applying this current the machine is totally field weakened and could theoretically be accelerated to infinite speed. Due to friction and lack of torque producing i_{sy} current this is however not possible in practice.

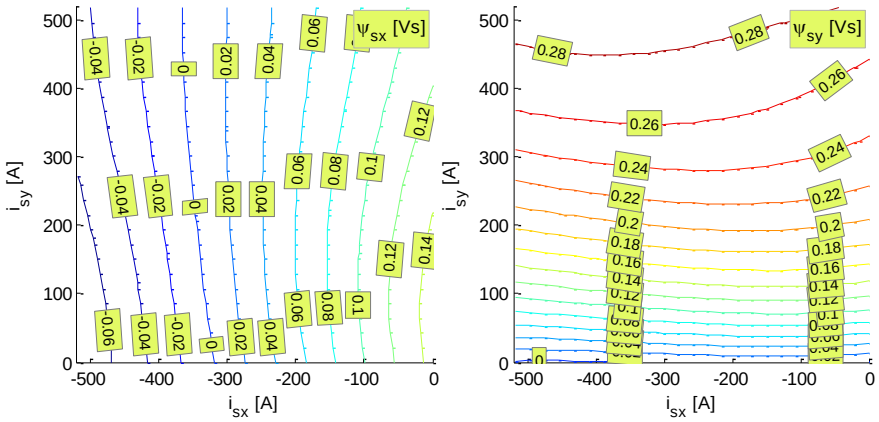

Figure 3.29 Stator flux linkage in the second quadrant in *x*-direction (left) and *y*-direction (right) as function of i_{sx} and i_{sy}

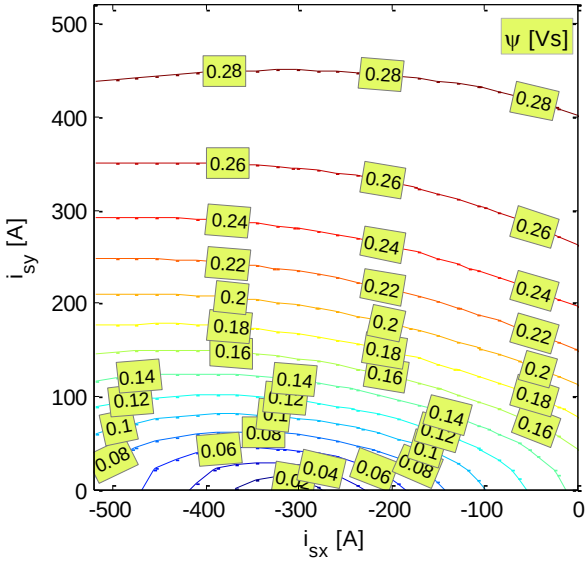

Figure 3.30 Stator flux linkage in the second quadrant as a function of i_{sx} and i_{sy}

Iso-torque curves in the second quadrant as function of i_{sx} and i_{sy} for the machine are presented in Figure 3.31. Based on the information of the torque, the MTPA curve is obtained (compare with Figure 3.2). As can be seen, the MTPA curve makes a slight bend into the second quadrant due to

the reluctance torque in the machine. Besides information of the torque, the figure also has information on the induced flux in terms of constant voltage ellipses for in this case 6000 rpm. Since the induced voltage is proportional to speed, the size of the voltage ellipses decreases with increased speed. Eventually, when the induced voltage reaches maximum available voltage (limited by the dc source) the current control is changed from MTPA to field weakening. In Figure 3.31 this can be seen as sections of circles representing the length of a number of different current vectors. When the voltage ellipses diminish, the current vector moves along the circle segments deeper into the quadrant, hence allowing for increased speed to the expense of reduced torque. Finally, for the current circles large enough to encircle the epicentre of the ellipses the MFPT curve is reached. This occurs at high speeds when the voltage ellipse becomes so small that the maximum current can no longer be applied. Instead, the current is reduced somewhat to obtain the highest possible torque at that speed.

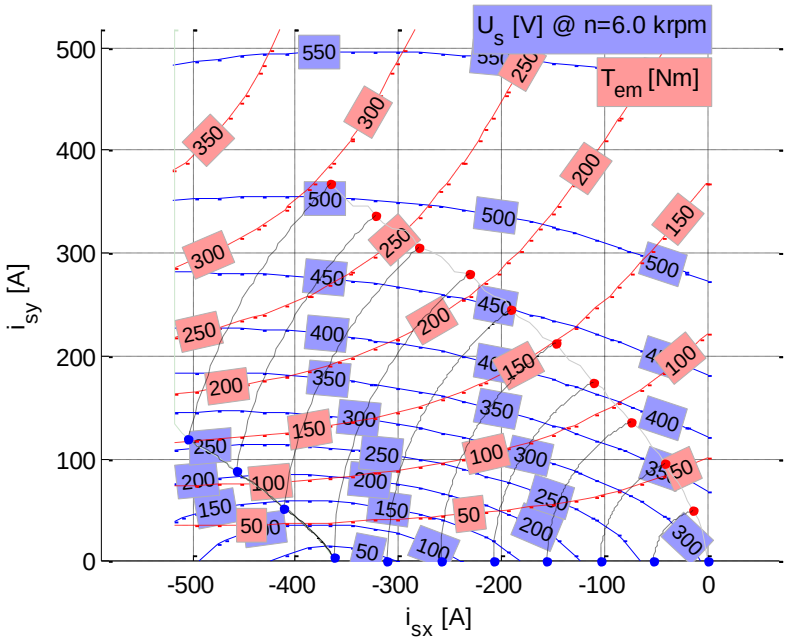

Figure 3.31 Torque and induced voltage at 6000rpm in the second quadrant as function of i_{sx} and i_{sy} with PM at room temperature together with the MTPA curve, maximum current curves and MFPT curve

Based on the information obtained from Figure 3.31 above, a torque speed diagram is derived and presented in Figure 3.32. The different torque curves in the figure originate from the different current vector circles in Figure 3.31. The circle with the smallest diameter corresponds to the lowest torque curve, and so on. The size of each current vector is presented along with the torque lines in Figure 3.32. With the torque and speed known, the matching power is calculated and presented along with the torque. Again, the lowest power line originates from the lowest torque line, and so on. When comparing the simulations with the requirements in Table 1, it is concluded that peak power is only just met around base speed, while peak torque is larger than desired.

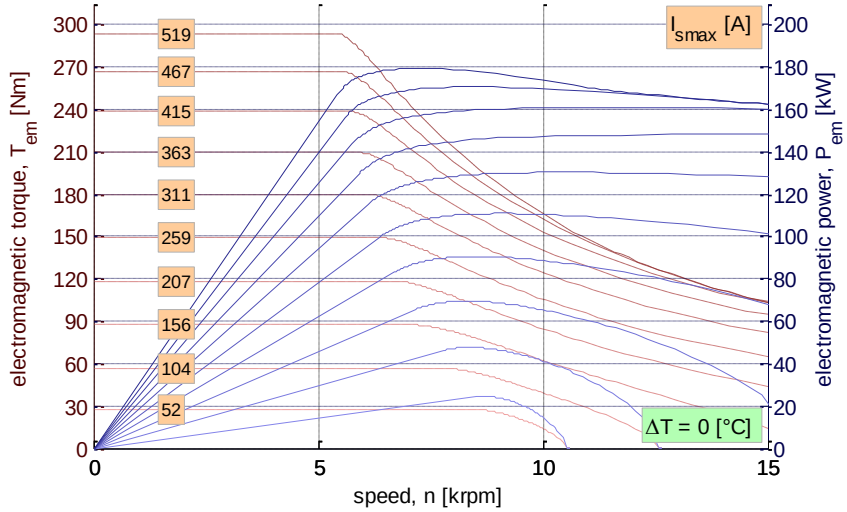

Figure 3.32 Torque- and power-speed diagram with PM at room temperature with the corresponding vector current I_{smax}

The temperature dependence of the machine can be seen in Figure 3.33 where peak and continuous torque and power curves are presented for 20°C and 100°C. As can be seen, the peak power is no longer fulfilled, but reaches around 170 kW around base speed and around 150 kW at top speed. Despite no longer completely fulfilling the power requirements, it is decided to go ahead with the prototype build. The continuous power benefits from the increased temperature since the increased temperature make the magnets slightly weaker. Consequently, the epicentre of the ellipses in Figure 3.31 is shifted slightly to the right and therefore extends the speed range in which the continuous current vector can be used. The peak torque is exceeding the requirements, also at high temperatures.

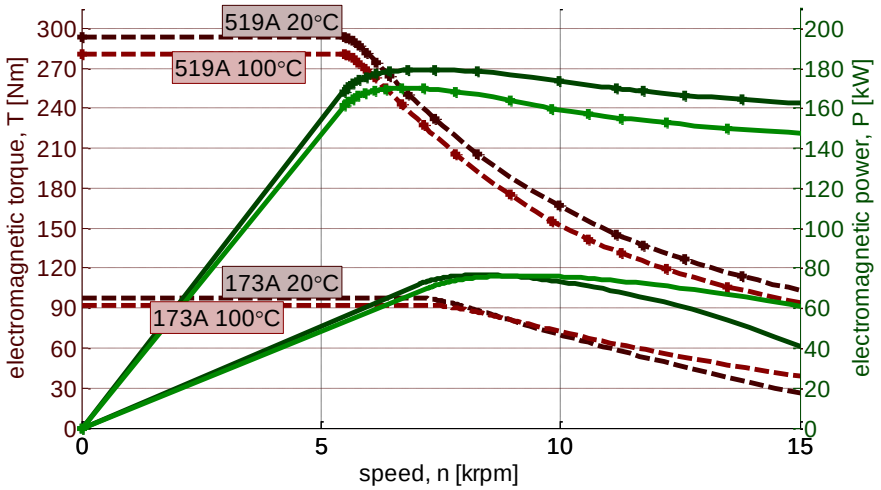

Figure 3.33 Influence of PM temperature on machine characteristics for 20°C and 100°C

An estimation of the power losses is done based on the current density in the windings and the flux density in the stator teeth and yoke. Hence the rotor losses as well as mechanical losses, such as friction and windage, are disregarded at this stage. The result is presented in Figure 3.34 and recalculated as an efficiency map in Figure 3.35.

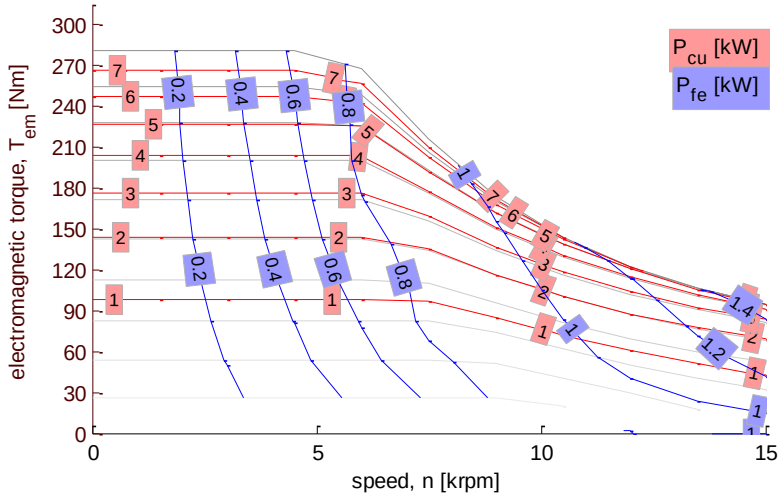

Figure 3.34 Power losses in the windings and the iron core at 100°C PM temperature, excluding mechanical losses

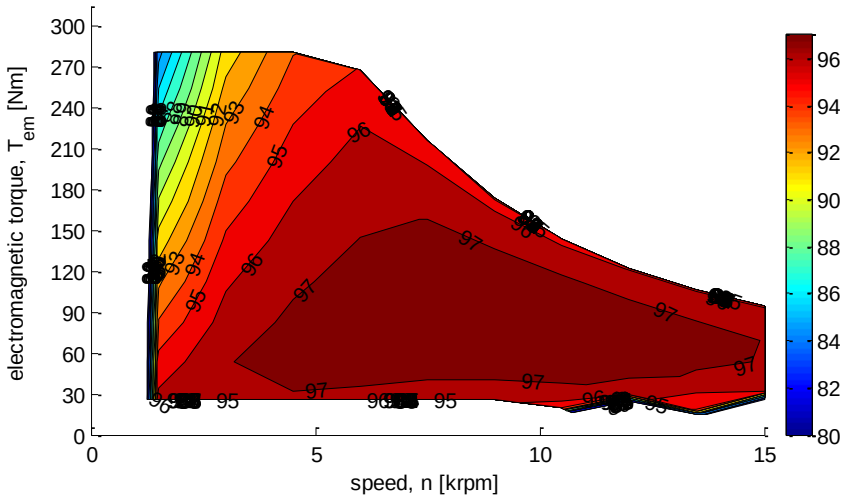

Figure 3.35 Efficiency map at 100°C PM temperature. N.B. rotor losses and mechanical losses not included

The power factor of the electric machine is presented in Figure 3.36. The significant reluctance torque in the machine can be seen on the reduction in power factor with increased torque below base speed. Above base speed, the power factor increases as the angle between voltage and current decreases. At high speed and low torque, the current vector starts to lead the voltage vector and as the angle increases, the power factor drops again.

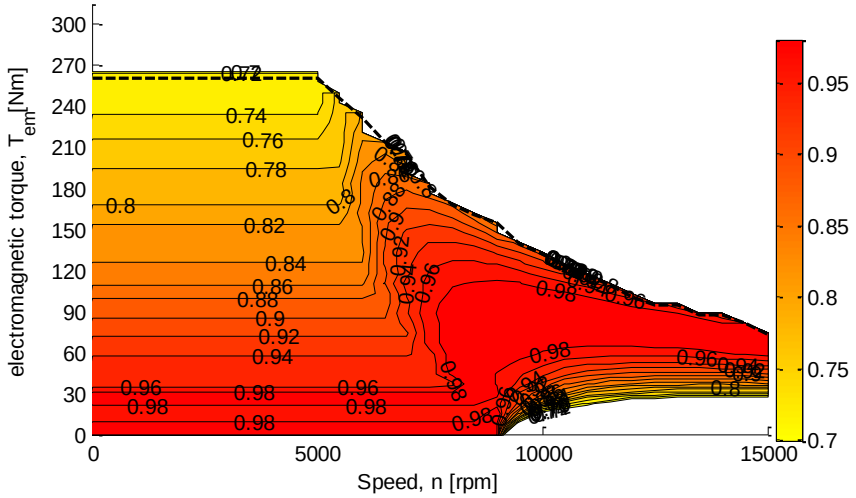

Figure 3.36 Power factor at 100°C PM temperature

Chapter 4

Prototyping

The following chapter describes briefly the manufacturing process of the prototype machine.

4.1 Stator

The stator manufacturing is made in two steps. At first laminations are stacked to form the active length of the machine. After that, the windings are inserted into the slots and connected at the non-driving end (NDE) of the machine.

Laminations

The stator laminations are stacked to form the active machine length. The skewing discussed in section 3.6 is achieved by a guiding bar in the tooling. The beginning of the stator stacking process can be seen in Figure 4.1.

The stacked stator is welded together using some of the oil channels as guiding lines. The welding joint can be seen in Figure 4.2 where the skewing also can be observed as the misalignment to the key groove, machined to prevent the stator from rotating in its housing.

Figure 4.1 Stator lamination stacking at the manufacturing tool

Figure 4.2 Stator laminations stacked and welded together

Windings

The stator windings are pre-wound with the right number of turns in separate coils for each loop in all phases. Once the different loops in each phase are in place, they are clamped together to from the total winding in each phase. To facilitate measurements on the prototype, the neutral point is not connected inside the machine. Instead all six cords are extruded from the machine and the neutral point is achieved in an external connection point. The clamping of the windings and the completed active stator are shown in Figure 4.3 and Figure 4.4. The stator is finally dipped in varnish to provide a protective and insulating layer on the end windings.

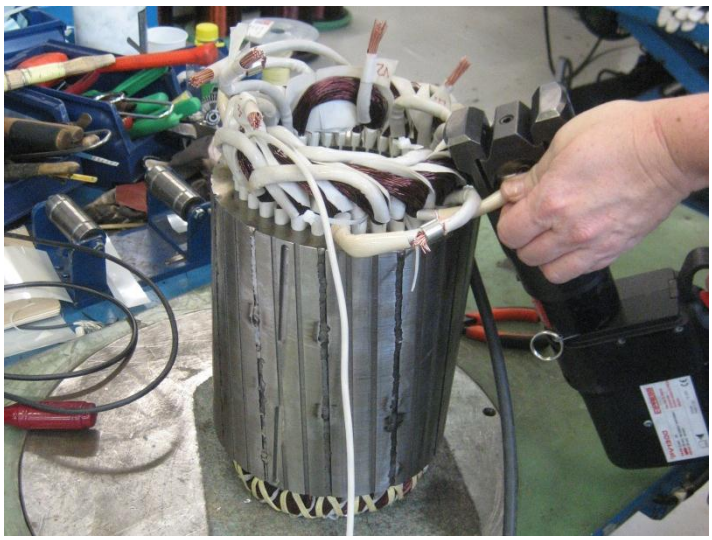

Figure 4.3 Clamping of the end windings

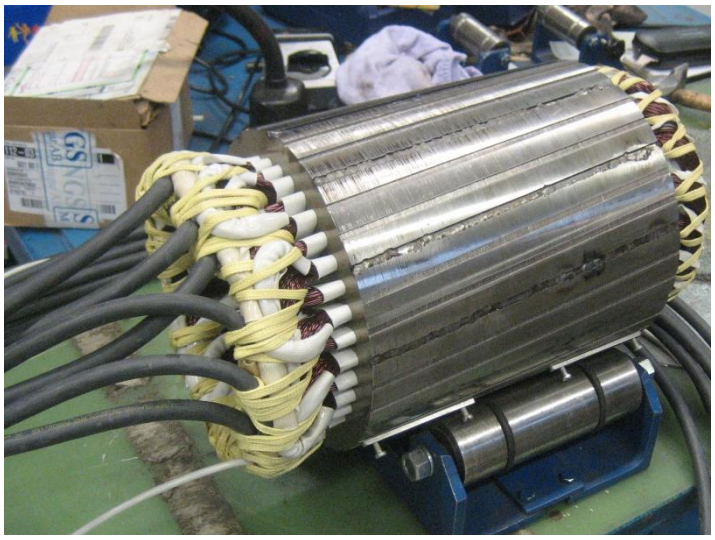

Figure 4.4 The completed active stator with three phase connection cables and three connection cables for the neutral point

Temperature sensors

The prototype is equipped with five temperature sensors of type PT100 RTD located as defined in Table 4 and Figure 4.5 below.

Table 4 Temperature sensors in the prototype machine

Sensor no.	Sensor name	Description
#1	$U_{hotspot}$	Located at the expected hot spot, halfway along the machine in the middle of a slot in one of the phases (phase U)
#2	$U_{statorback}$	Located at the stator back outside the slot containing sensor #1
#3	NDE	Located at the bearing on the non-driving end
#4	DE	Located at the bearing on the driving end
#5	$U_{endwinding}$	Located on the end windings from the slot containing sensor #1 (phase U)

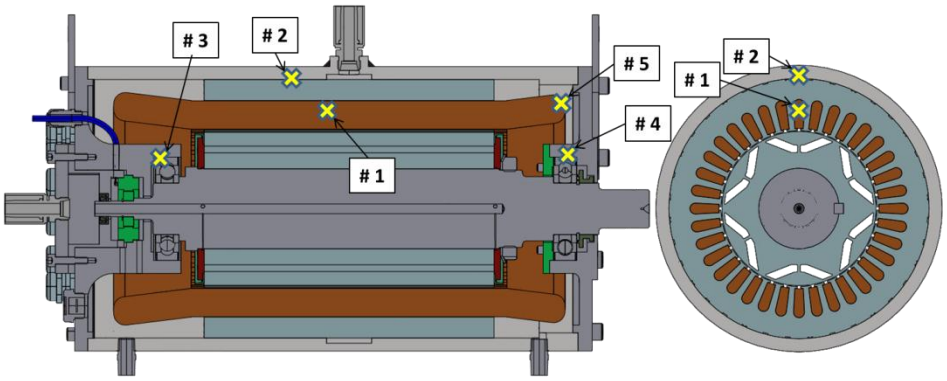

Figure 4.5 Temperature sensor positions in the prototype machine

4.2 Rotor

The rotor assembly is briefly described and shown in figures in the following section.

Lamination and magnet stacking

The laminations in the rotor are stacked directly onto the rotor shaft using a key as guide. The key also prevents the laminations from rotating on the shaft. The laminations are pre heated on a stove and shrink fitted on to the shaft. This provides a tight fit between the shaft and the laminations. The

magnets are inserted gradually as the laminations are stacked. The first section of the stacked rotor laminations on the shaft just before inserting a layer of magnets can be seen in Figure 4.6. Preheating of a couple of laminations on a stove is shown in Figure 4.7.

Figure 4.6 Rotor lamination stacking at the manufacturing tool using the wedge as guide

Figure 4.7 Rotor laminations pre heated on a stove before shrink fitted onto the rotor shaft

The magnet polarity is established and controlled using a stick with a magnet attached to the tip and carefully inserted in the intended rotor cavities. Pieces of iron are placed on the side of the rotor to prevent the magnets from repelling each other in the rotor length direction. The magnetic force holding the iron pieces are stronger than the repelling force from the magnet beside. The polarity check can be seen in the left side of Figure 4.8. The iron pieces keeping the magnets in position can also be seen as the crown of nuts surrounding the rotor. Before filling the cavities in the rotor with epoxy, the laminations are pneumatically pressed tightly together to obtain a high iron fill factor in the rotor. The rotor prepared for epoxy filling is seen in Figure 4.9.

Figure 4.8 Rotor magnets insertion with a crown of iron pieces (nuts) keeping the magnets and checking the polarity of the magnets

Figure 4.9 Rotor assembly being prepared for epoxy filling

4.3 Experiences from the prototyping

The experiences from taking part of building the prototype are very valuable in many ways. For example in terms of gaining understanding of how different details in the design affect the build. When working in FE-environment with the possibility to zoom in and out it is very easy to lose track of the perspective. Sometimes the manufacturing tolerances are larger than the distances fine-tuned in the simulation model.

Although working in the rather long and slender inner periphery of the stator is manageable, it is understood that a longer machine would require a slightly larger diameter to make it possible to work efficiently with the windings. On the other hand, the long machine design means that skewing can be introduced without affecting manufacturing too much. At least, this is the case when the machine is wound by hand. In fact, when working inside the prototype machine it is hard to detect the skewing at all.

The fill factor of 40% is indeed rather conservative. An experienced machine winder could wind the machine without too much effort. Should

the fill factor on the other hand be higher, it will increase the time and effort to wind the machine. This could increase the manufacturing cost as well as the risk of damaging the windings when working with them. Therefore, if considering serial production the advantages with a high fill factor must also be weighed against manufacturability.

Regarding the end windings it is understood that a certain extruding length is required just to bend the windings. Furthermore, with distributed windings all phases are sharing the same volume making it even more difficult to obtain compact end windings.

Working with the magnets gives a good understanding of the magnetic strength and how brittle they are. If not being careful, dropping two magnets together easily results in cracks in the corners. The tolerances introduced in the Design for manufacturability section in chapter 3.2 make it easy to insert the magnets. The tolerances in the prototype manufacturing of the magnets as well as the laminations is however often better than in serial production.

Chapter 5

Measurements

The electric machine is tested in no load as well as loaded conditions. The following chapter describes the tests performed and the results from the measurements.

5.1 No load tests

Tests at no load are done to investigate the induced voltage and drag torque as well as the temperature dependence of the electric machine.

Induced voltage and no load torque

No load tests are performed to investigate the induced voltage wave form and harmonic content. Drag torque is also recorded but due to no oil cooling circuit in connection to the test bench this is done without oil only.

Test setup

The electric machine (test object) is mounted in a test bench consisting of an in-line torque transducer (Vibro-meter TG5), a rig gear and a dynamometer. Rotation of the test object is done with the rig machine. Induced voltage on each phase is measured with an oscilloscope (Tektronix TPS 2024), connected via voltage probes (Tektronix P5200) scaling the signals to a level suitable for the oscilloscope. The oscilloscope is also providing the rms (root mean square) value on each phase. The torque transducer is calibrated with a number of known masses on the end of a bar with known length. The temperature dependence of the torque transducer is however not investigated. The purpose of measuring the torque is to investigate no load losses due to friction, windage, magnetic losses etc.

Alignment of the electric machine (test object) to the test rig is fine-tuned with an analogue distance indicator mounted on the shaft before securing the machine to the test bench. The test is commenced at low speeds, gradually increasing up to 6428 rpm and then gradually reduced back to stand still. The top speed is limited by the rig gear and the dynamometer. Measurements are recorded during both the accelerating phase and the decelerating phase. The test setup can be seen in Figure 5.1 with the connection to the torque transducer to the left and the rig gear and dynamometer in the background to the right.

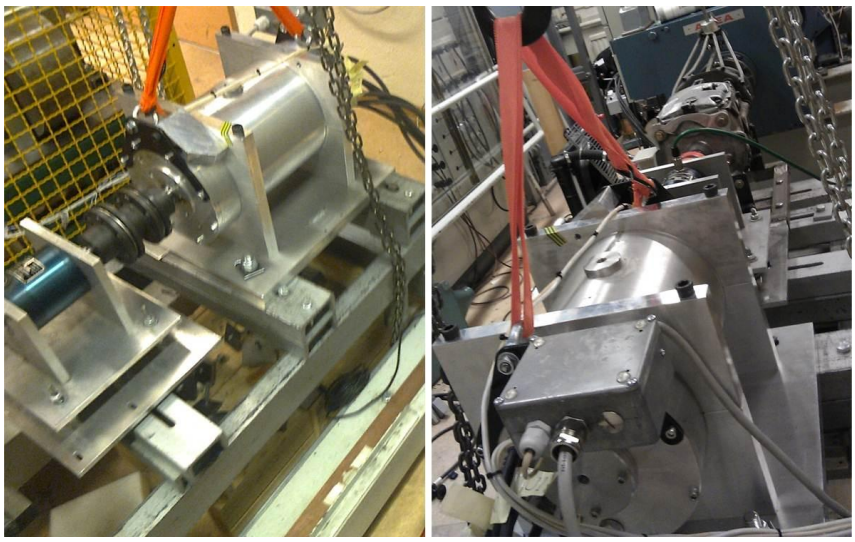

Figure 5.1 Test set up for the induced voltage and drag torque measurements

Test results

Measured voltage and harmonic content for all phases are presented in Figure 5.2. The flat top is caused by the skewing of the stator. Looking at the harmonics the effect of skewing can be seen on the low harmonic content.

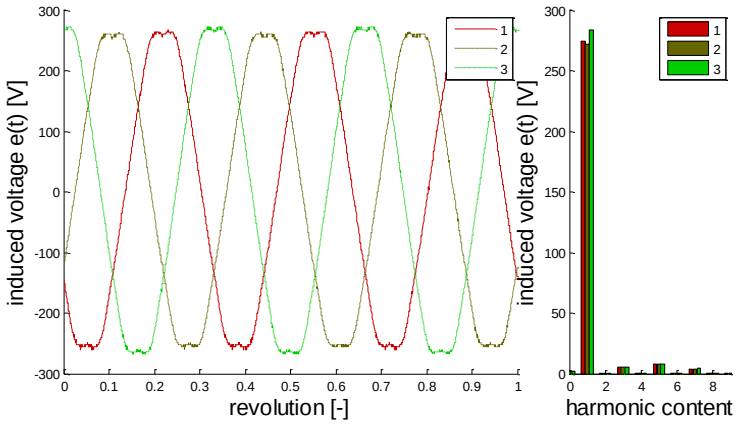

Figure 5.2 Induced voltage wave form and harmonic content for all phases

The linked flux and no load torque as functions of rotational speed are presented in Figure 5.3. As can be seen, the torque makes an unexpected leap at around 4000rpm during the acceleration phase. This is possibly due to thermal effects in the torque transducer but is not noticed until after the completion of the experiment. It can also be related to a slight misalignment of the machine. Despite being calibrated before starting the measurements, vibrations from the rig gear might have dislocated the EM slightly. During the deceleration phase, the torque behaves more as expected. The deviation of phase three (Ψ 3) compared to phase one and two (Ψ 1 and Ψ 2) is caused by the voltage probe at phase three.

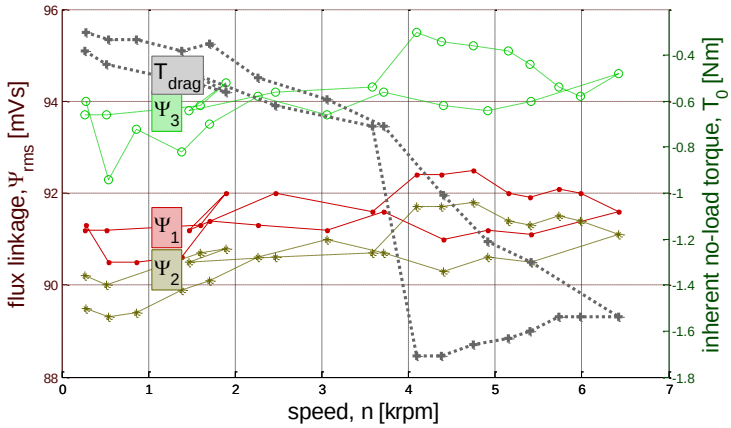

Figure 5.3 Stator flux linkage (rms) and torque as function of speed during no-load operation

The resulting no load losses are presented in Figure 5.4. When comparing the result with the speed dependent iron losses in Figure 3.34 it is noticed that the measured losses are higher than those predicted by the simulations. This is expected since the simulations do not include the mechanical losses in terms of friction and windage. However, due to the strange behaviour of the torque transducer, all conclusions drawn from the no load loss test result should be considered with care.

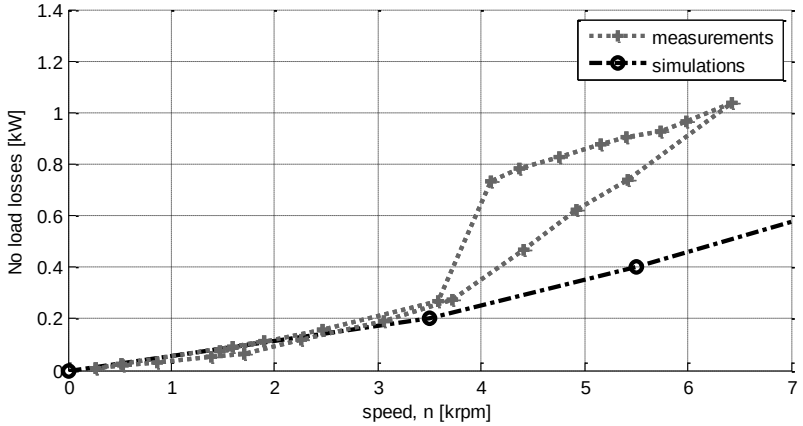

Figure 5.4 No load losses from the torque measurements and simulations

Temperature dependence measurements

The temperature dependence of the electric machine prototype is also investigated by measuring the induced voltage at a range of different machine temperatures.

Test setup

The flux linkage as function of PM temperature is investigated by preheating the electric machine in a heat cabinet. The heat cabinet temperature is gradually increased up to just below 100°C and then decreased back to ambient. This sequence is repeated twice. After at least three hours at each temperature, thermal equilibrium is assumed to be reached in the machine. This assumption is used to establish the PM temperature by reading the PT100 temperature sensors in the stator and at the bearings (see Table 4 and Figure 4.5). The temperature is established by reading the resistance in the sensors with a Multimeter (Fluke 88V).

The induced back emf-voltage (electro-motive force) on each phase is measured with an oscilloscope (Yokogawa DL708E with plug-in input

module 701853HR) at a number of different rotating speeds up to around 2000 rpm (equivalent to around 100 electrical hertz). The raw data from the oscilloscope is post-processed to give the rms voltage as well as the frequency. The frequency and voltage are used to calculate the flux linkage.

In order to gain access to the machine, the heat cabinet is opened during each set of voltage measurements. A hand held drilling machine with a custom made fork designed to fit the shaft groves in the EM is used to rotate the machine. This makes it possible to rotate the machine without removing it from the heat cabinet which would give time for the machine to cool down. A picture of the test set up with the machine attached to the oscilloscope can be seen in Figure 5.5 where the custom made fork is seen in the inset picture.

Figure 5.5 Test set up for temperature dependence measurements with the custom made fork connected to the shaft in the small picture

The temperatures are read before and after each voltage measurement. This is done to make sure that the PM temperature can be considered constant even if the heat cabinet is opened during the measurements. Each set of measurements is completed within approximately ten minutes.

During the first temperature reading, before the voltage measurements, the mutual difference in temperature between all five temperature sensors is less than 0.5°C throughout all measurements in the entire experiment. This indicates that the PM temperature also can be considered to be in the same range. Hence, that the assumed thermal equilibrium is accomplished.

The temperature difference before and after each set of measurements varies partly depending on the sensor position and partly on the different temperatures. This correlates to a higher difference to ambient temperature which results in a faster temperature decrease. It is also noticed that the temperature sensors at the bearings (#3 and #4 in Table 4 and Figure 4.5) are affected slightly more than the sensors buried inside the machine. Since the magnets are also buried, the PM temperature should coincide better with temperature sensor #1 and #2 rather than #3 and #4. The fact that the heat cabinet is opened on the driving end (DE) of the machine is also noticed in the temperature readings since the difference before and after each measurement is slightly larger for sensor #4 at the driving end than #3 at the non-driving end.

For temperature sensor #1 and #2, the largest difference before and after a measurement is 0.5°C. The largest temperature decrease for a single temperature sensor during a measurement is less than 3°C, noticed in sensor #4. Both these cases are observed during the 95°C measurement, hence, with a high difference to ambient temperature. These results support the assumption that the PM temperatures can be considered constant throughout each set of measurements.

Test results

The flux linkage as function of temperature for each phase is presented in Figure 5.6. As can be seen, all phases are close together indicating a good balance between the phases. In Figure 5.7 the simulation results are included. The results differ with around 4% at room temperature and around 3% at 100°C. This deviation is potentially caused by small deviations in the magnet size and position compared to the simulations. The small airgap introduced around the magnets due to manufacturing tolerances might have made it possible for the magnets to be slightly dislocated in the rotor. Finally, the deviation could also be affected by the inherited simplifications made when modelling a 3-dimensional component using a 2D FE-simulation model. The conclusion from the measurements is that the implemented temperature dependence in the simulation model is adequate.

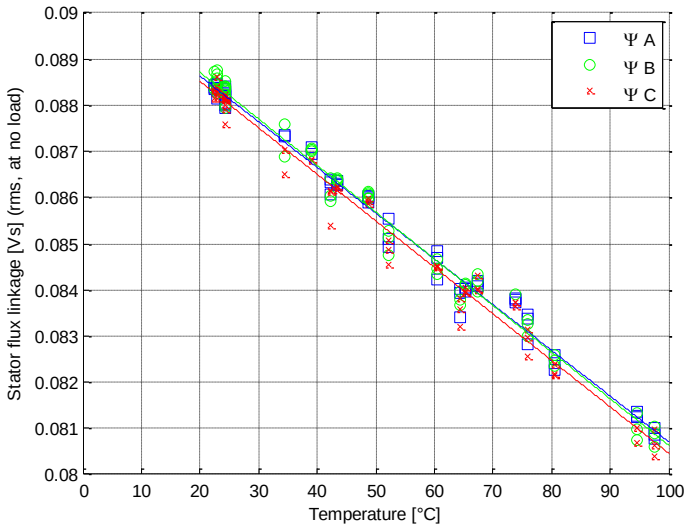

Figure 5.6 Measured stator flux linkage (rms) as function of machine temperature in all phases

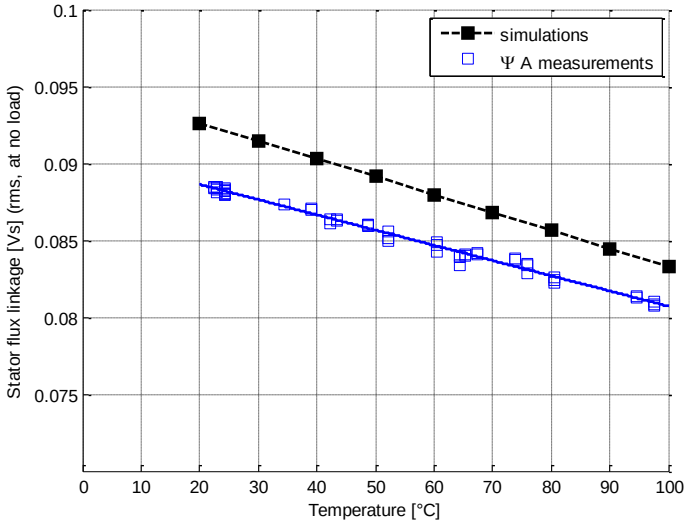

Figure 5.7 Stator flux linkage (rms) in phase A from measurements and simulations as function of machine temperature

5.2 Load test

The machine testing at loading conditions is described in the following section. The machine characteristics are obtained with dynamic loading. Due to limitations in the test facility, the machine is not tested up to full rated current. The intention is to also test the machine in a system test rig connected to a gearbox and combustion engine. This test suffers from problems with the test rig and is therefore performed to a limited extent only.

Dynamic loading

The machine characteristics during loaded operation are obtained from intermittent load points. The applied electromagnetic torque within each load point is ideally kept constant. This means that the machine is accelerated to different set speeds a number of times with different i_{sx} and i_{sy} currents. When performing dynamic loading, the test object is mounted in a test stand and the shaft is connected to a disc or flywheel with a known inertia. This inertia is used, together with an estimation of the rotor inertia, to derive the torque from the acceleration time. The theory behind the dynamic testing can be seen in [24]. The validity of the dynamic loading is also investigated in [25] and [26].

Test setup

The electric machine is mounted in a test bench and connected to the dynamic loading test equipment, built at IEA. Currents, voltage and frequency are recorded internally in the test equipment. To improve accuracy, the three phase voltages are also measured with external probes (Tektronix P5200A) and fed into the control unit. Limitations in the test facility and dynamic loading test equipment prevent the machine from being tested up to the expected peak torque and power. The available dc-voltage source is limited to 300 Vdc due to problems with stability in the thyristor rectifier control. The current measurements in the dynamic loading equipment are recorded on two phases and scaled with a transformation rate of 2000. The scaled current is measured over an 82 ohm resistance with an analogue input that can handle ±10 V. This means a limitation of 10 divided by 82 multiplied by 2000 (10/82·2000), hence 243.9 A in peak current. With power invariant transformation to the *xy*-reference frame (described briefly in the part of section 2.2 covering the electric machine), this means a maximum vector current of 243.9 multiplied by square root of 3/2 ($243.9 \cdot \sqrt{3/2}$), hence 298.7 A. Since the current seen by the dynamic loading equipment is cut at that level,

exceeding this limit might result in losing the control of the EM. A safety margin is added to the current references by limiting the current vector length to 280 A. This can be compared with the 519 A used as peak in the simulations (see, e.g., Figure 3.31). The resulting maximum available rated electric power is therefore 300 V multiplied by 280 A divided by square root of 2 ($300 \cdot 280/\sqrt{2}$) hence just below 60 kW. The electric machine mounted at the test bench can be seen in Figure 5.8 with a yellow section on the flywheel to facilitate visual observations of the accelerations.

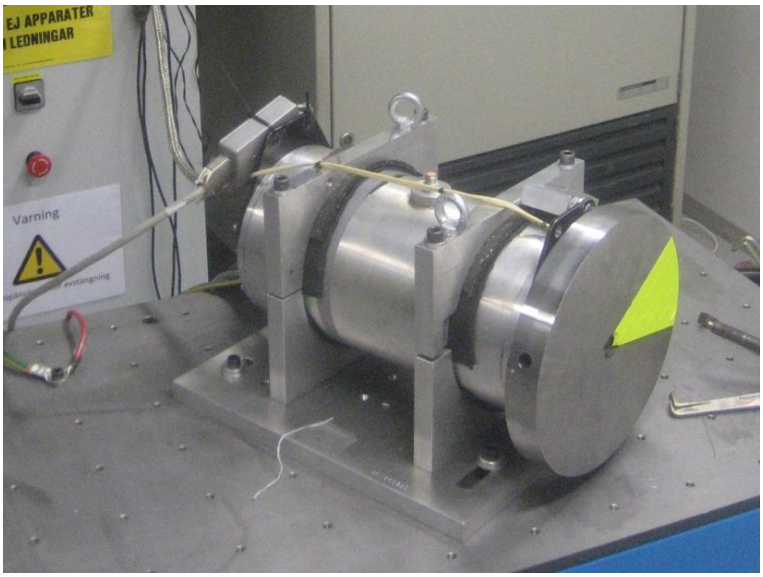

Figure 5.8 The test object mounted at the test bench with the attached flywheel for the dynamic testing to the right

The test object is accelerated by applying currents in the xy-rotor reference frame. When the maximum speed is reached, limited by either the available voltage or a set top speed, the machine is decelerated back to zero and then a new sequence is commenced with another current combination. Eventually a matrix similar the left side of Figure 3.2 is created. Based on the acceleration time and the inertia, the torque (T) is derived according to (21) where J is the total inertia of the rotating parts and ω is the rotational speed in radians per second. The stator flux linkage is derived from the voltage- and speed differences during each acceleration sequence. This way, the winding resistance can be disregarded since it not is speed dependent. Torque can also be derived from the flux and currents together with the number of pole pairs.

$$T = J \cdot \frac{d\omega}{dt} \tag{21}$$

Test results

The measured torque is presented in Figure 5.9 together with the current limit. A comparison with the simulation result is presented in Figure 5.10. When comparing the torques a small deviation can be seen. Except for in the lower left corner, this deviation seems to be rather constant. Possible reasons for the deviation could be related to the accuracy in the combined inertia J of the flywheel and the rotor, cf. equation (21). It could also be related to the simplifications regarding mechanical losses in the simulation model, especially in the test points where a higher rotational speed is reached. Finally, the actual magnetic strength compared to the data used in the simulations could deviate slightly, which could affect the result. The irregular shape visible at high field weakening currents i_{sx} and low torque producing currents, i_{sy} in the lower left corner of the plot might be caused by the use of a different external inertia in that area. The reason for using a different flywheel is that this area coincides with the epicentre of the ellipses described in Figure 3.31. Hence, the currents applied in this area allow higher top speed before reaching the voltage limit. Therefore, a smaller flywheel is used for safety reasons.

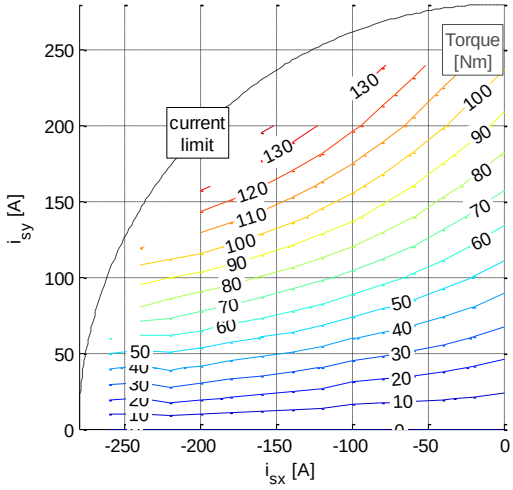

Figure 5.9 Torque as function of i_{sx} and i_{sy} based on dynamic loading with the current limit form the test equipment

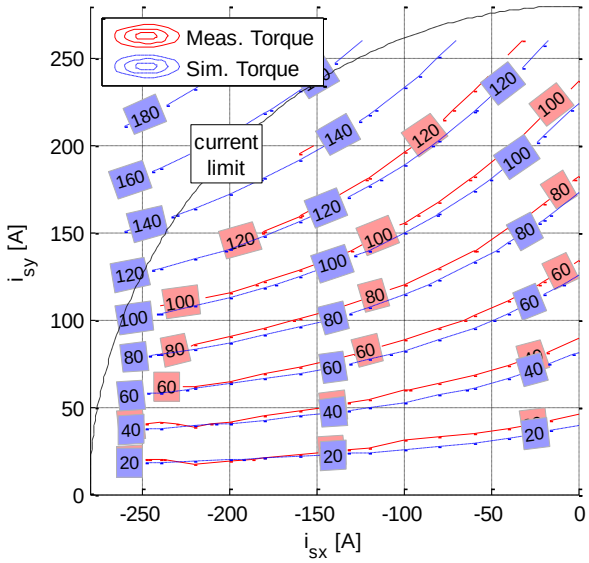

Figure 5.10 Torque from measurements and simulations as function of i_{sx} and i_{sy}

The stator flux linkage as a function of i_{sx} and i_{sy} current is presented in Figure 5.11. In the topmost and middle graphs, the stator flux linkage is divided in *x*- and *y*-components, respectively. In the graph at the bottom the total stator flux linkage in the machine can be seen. The expected elliptic shape of the stator flux linkage can be seen with epicentre just outside the measuring range, at approximately -280 Amps along the *x*-axle.

The conformity between the measured stator flux linkage and the simulation result is examined in Figure 5.12. When doing the comparison it can be seen that the measured *x*-directed stator flux linkage ψ_{sx} is lower than the simulations predict. For the *y*-directed stator flux linkage ψ_{sy}, the measurement readings are higher than the simulations. In order to better study the differences between measurements and simulations, ψ_{sx} is plotted as function of i_{sx} only and similar for ψ_{sy} as function of i_{sy}. This is done in Figure 5.13 where i_{sy} is 20 A for the *x*-directed stator flux linkage and i_{sx} equal to zero for the *y*-directed stator flux linkage. The reason for applying 20 A in *y*-direction, is that the measurements depend on the acceleration of the machine. Thereby, an accelerating current is required in order to give a result.

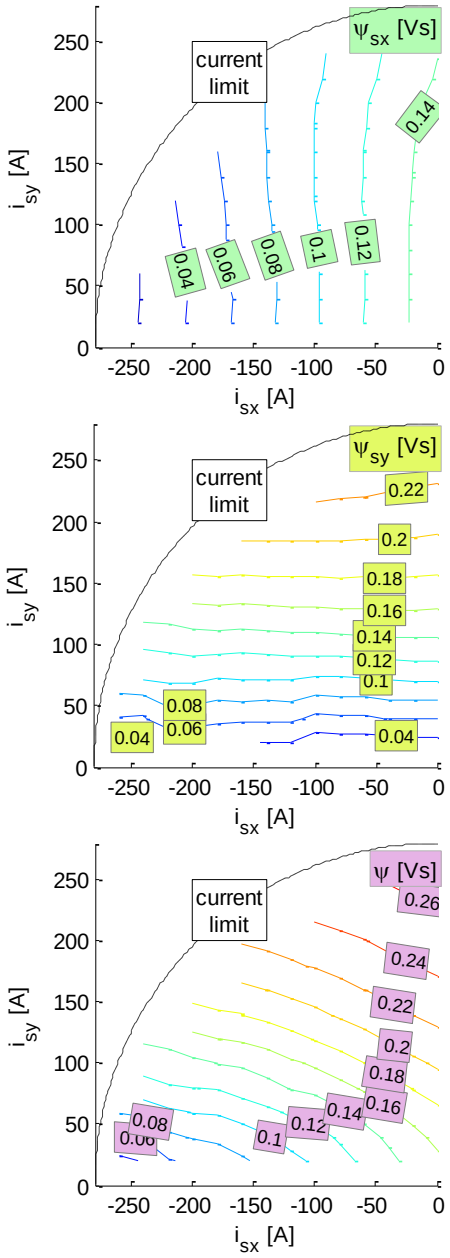

Figure 5.11 Stator flux linkage in *x*-direction (top), *y*-direction (middle) and in total (bottom) as function of i_{sx} and i_{sy} with the current limit from the test

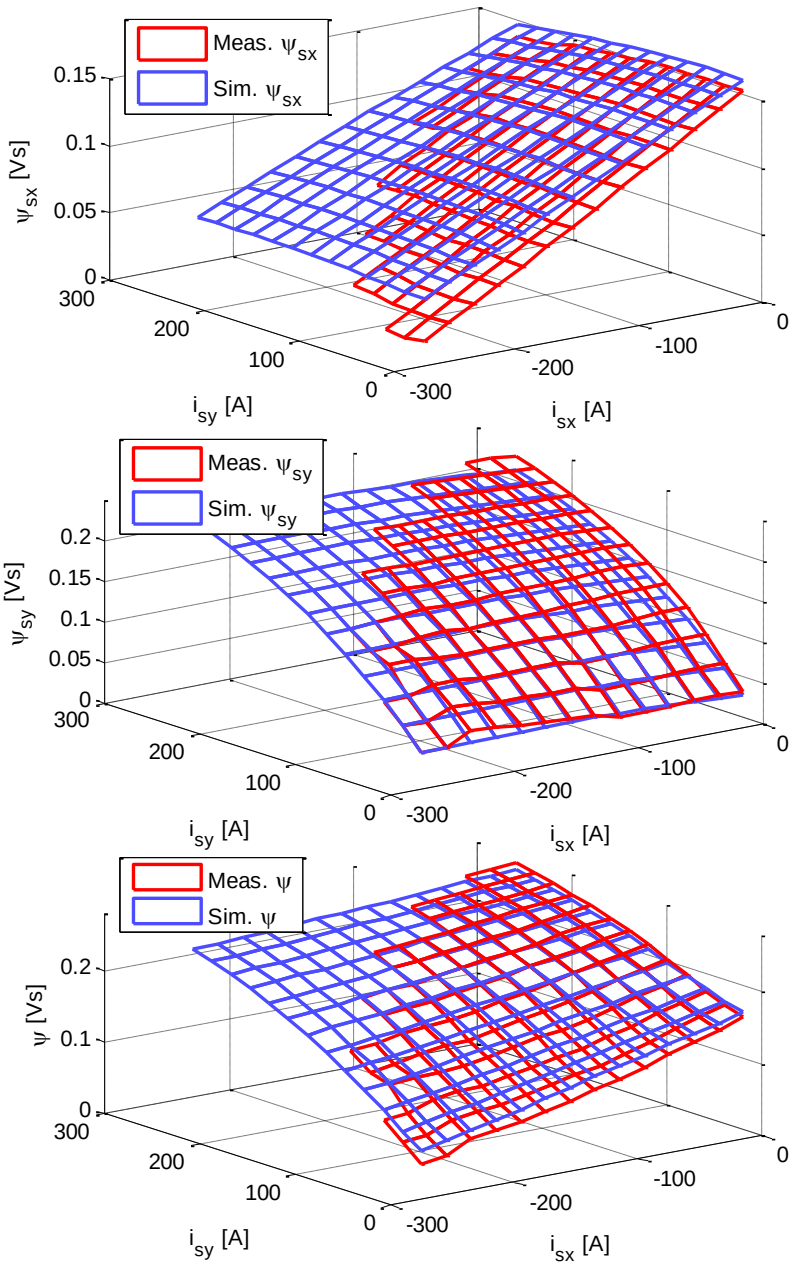

Figure 5.12 Stator flux linkage in *x*-direction (top), *y*-direction (middle) and in total (bottom) from measurements and simulations as function of i_{sx} and i_{sy}

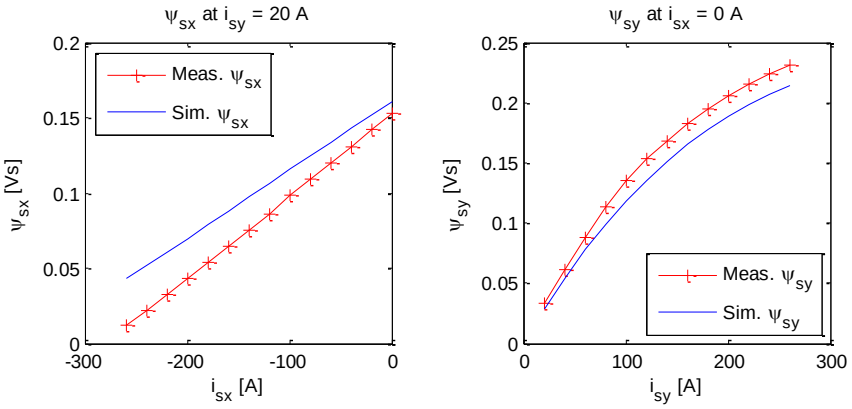

Figure 5.13 Stator flux linkage in *x*-direction as function of i_{sx} (left) and in *y*-direction as function of and i_{sy} (right) from measurements and simulations

When looking at ψ_{sx} in the left graph in Figure 5.13, it is partly noticed that the measured *x*-directed stator flux linkage is somewhat lower than predicted at zero i_{sx}-current. This coincides with the fact that the measured torque along the vertical axle in Figure 5.10 is smaller than the simulations. It is also noticed that the trend at increasing negative i_{sx} differs from the measurements. The effect of applying a field weakening current is higher than predicted. The stator flux linkages in *x*- and *y*-direction are expressed in (22) and (23), respectively. In (22), it can be seen that ψ_{sx} consist of a constant contribution from the magnets ψ_{PM} together with the current multiplied by the *x*-inductance L_x. As the deviation between simulations and measurements consists of a constant offset as well as a current dependant part, both ψ_{PM} and L_x needs to be investigated.

$$\psi_{sx} = \psi_{PM} + L_x \cdot i_{sx} \tag{22}$$

$$\psi_{sy} = L_y \cdot i_{sy} \tag{23}$$

Since the simulations are performed in a 2D-FE environment, all effects related to the end windings are excluded. In order to investigate the influence of the end winding inductance L_{EW}, (24) [27], pp. 212, is used in combination with the assumption described in Figure 5.14. Here, A is the enclosed area, determined by the extruding end winding lengths on each side of the machine together with the distance between six stator slots (cf. Figure 3.19). The length l of the coil is estimated to approximately half the

stator slot depth. Although the area is shared by three phases in radial direction, it is assumed that the end windings propagate a bit over the stator back. N is the number of stator turns per coil. Since each phase contains six sets of separate coils, the total inductance per phase is obtained by multiply the result in (24) by six. With the given assumptions, the resulting end winding inductance becomes L_{EW} = 70 µH per phase.

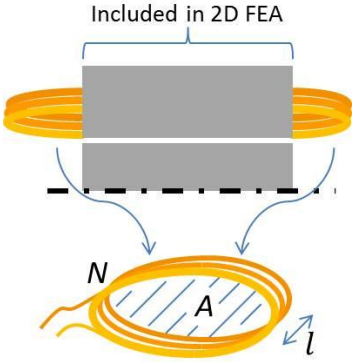

Figure 5.14 Derivation of the end winding inductance

$$L = \mu_0 \frac{N^2 \cdot A}{l} \tag{24}$$

Equation (22) is solved for L_x by using numbers from the left graph in Figure 5.13. The resulting inductance from the simulations is L_x^{sim} = 450 µH compared to L_x^{meas} = 540 µH from the measurements. The influence of L_{EW} could be investigated by implement it in the simulation postprocessor. A more thorough way to complete the investigation would be to set up a 3D FE simulation. This is however not included in this thesis. Instead, the estimated end winding inductance L_{EW} is added to the inductance obtained in Figure 5.13 and plotted again in Figure 5.15. Here, ψ_{sx}^{EW} is a result of replacing L_x^{sim} with the sum of L_x^{sim} and L_{EW}, hence, L_x^{EW} = 520 µH. This should at least indicate how the influence of the end windings should affect the result.

Another aspect that could be considered to investigate is the iron core. By manipulating with the relative permeability and saturation curve of the laminations and study the influence on the simulation result, a conclusion could be drawn on whether it also might contribute. This is not included in the present work, but needs to be further investigated in the future.

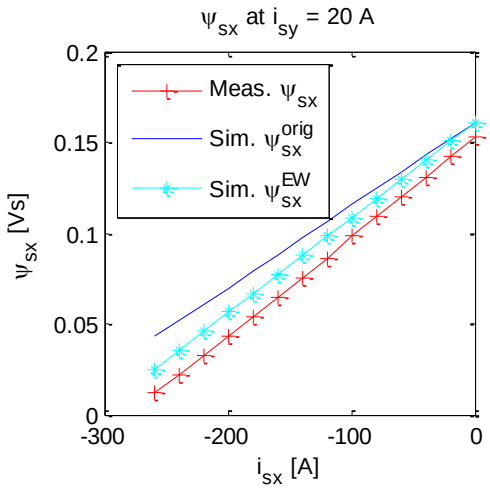

Figure 5.15 Stator flux linkage in *x*-direction as function of i_{sx} from measurements and simulations with- and without an estimation of the end winding inductance

The deviation at zero i_{sx}, still seen in Figure 5.15, ought to be related to the modelling of the permanent magnets. Both in terms of PM material properties and actual PM size in the prototype compared to the simulation model. The test protocol from the manufacturing of the magnets are used as input in the simulations to obtain an as good estimation as possible of the magnets. The physical size might differ from the simulation model due to tolerances and radii at the edges and corners. The PM, as it is defined in the simulation model, is a perfect cuboid, while the real magnet has rounded edges. Also, the exact location of the magnets could affect the result. The tolerances present around the magnets might have shifted the magnet position slightly, resulting in a change in the amount of flux leakage.

Another, perhaps less decisive, reason could be the influence of different PM temperature. This is further investigated by looking at the studies made on the temperature dependence in section 3.4 and section 5.1. By comparing ψ_{sx} at i_{sx} equal to zero in Figure 5.15, with the total stator flux linkage in Figure 5.7, it can be seen that the deviations in percentages between measurements and simulations are in the same order, around 4%. Since the underlying temperature measurements in Figure 5.7 are considered rather accurate, the present deviation should be imposed by a difference when modelling the magnets, rather than the temperature. Another comparison with Figure 5.7 can be done by looking at Figure

5.16. Here the *x*-directed stator flux linkage from the dynamic measurement is presented together with the corresponding values from the simulations at a number of different temperatures. At i_{sx} equal to zero, the measurement seems to agree with the simulation results with a PM temperature of 60°C-70°C. This coincides well with Figure 5.7, where the measured stator flux linkage at room temperature has similar value as the simulation model at around 60°C.

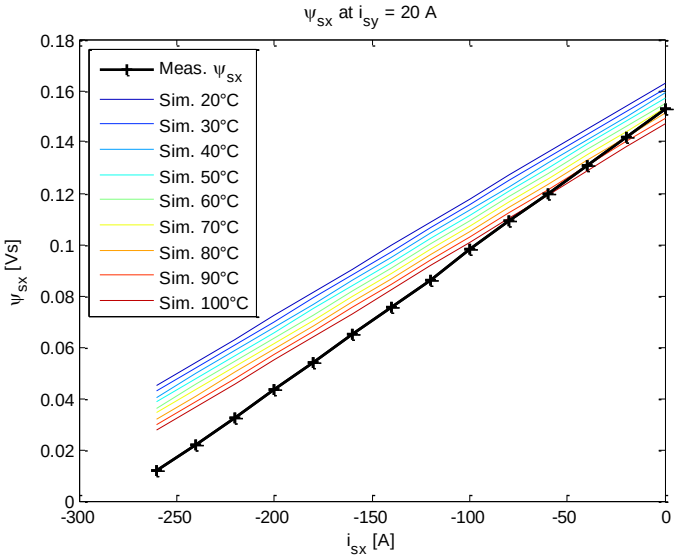

Figure 5.16 Stator flux linkage in *x*-direction as function of i_{sx} from measurements and simulations with different temperatures

Looking at the *y*-directed stator flux linkage, seen to the right in Figure 5.13, the deviation seems to diminish as the current approaches zero. This is expected since the only stator flux linkage at zero current is that of the PM, which according to the definition should be linked to the stator in x-direction only. This means that the only flux linkage available in *y*-direction is that coming from the inductance L_y in (23). A quick investigation of the influence of L_{EW} (derived earlier) on the *y*-directed inductance L_y is done by manipulating with ψ_{sy} in a similar way as for ψ_{sx} previously. The result is plotted in Figure 5.17. As can be seen, the influence at lower currents is rather marginal. This is a consequence of less current, which means less saturation of the iron core and therefore a higher inductance. At higher currents, when the iron core starts to saturate and L_y decreases, the influence of L_{EW} is higher.

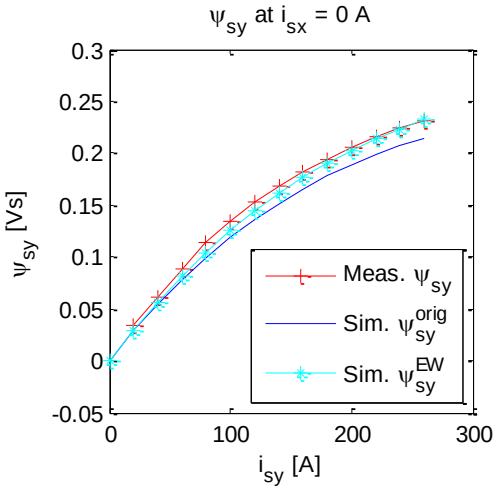

Figure 5.17 Stator flux linkage in *y*-direction as function of i_{sy} from measurements and simulations with- and without an estimation of the end winding inductance

Another possible explanation to the deviation in ψ_{sy} could be related to simplifications when deriving the stator flux linkage from the measured voltage. Although the winding resistance is accounted for, the speed dependent equivalent iron loss resistance, described in [28], is not. According to [28], a way to include this equivalent iron loss resistance is to perform the measurements at both positive and negative rotational speed. This has been done in [26] where ψ_{sy} agrees well with the simulation result. The deviation in ψ_{sx}, observed earlier in Figure 5.12 and Figure 5.13 is also observed in [26]. This supports the theory that the deviation in *y*-directed stator flux linkage, at least partly, is caused by the speed dependent iron loss effects. A way to establish this is to perform additional measurements according to [26], something not included in this thesis.

Besides the previously mentioned possibilities for the deviation between measured and simulated stator flux linkage, inaccuracy in the voltage measurements might also have an influence on the test result.

5.3 System testing

The electric machine is tested in a larger system together with an AMT gearbox (described further in section 2.1) and an internal combustion engine. The system testing is used to evaluate the interaction with the

gearbox and ICE and to some extent the continuous EM operation with oil cooling in operation. The system testing is done to a limited extent due to problems with the test rig.

System test set up

A setup similar to that explained in Figure 2.6 is built up. Instead of a rear axle, a large fly wheel is connected to the gearbox output. The intention is to simulate part of the inertia found in a vehicle during accelerations and decelerations. The flywheel is not used due to problems when decommissioning the test rig. Loading of the electric machine is instead achieved by rotating the ICE through different gears and with/without the engine exhaust brake. An oil system with a feed pump, filter, external cooler and a distribution block supplies gearbox oil to the PTO gear drive and the electric machine. A drain pump is used to return the oil to the gearbox. Since the oil system does not include any sensors, it is not possible to measure oil flow rate, pressure drop or inlet/outlet temperature.

Control of the electric machine is done with a CompactRIO (CRIO) controller from National Instrument[8]. The user interface is built in Labview environment by PhD student Yury Loayza [29]. Current references are sent via Profibus to the frequency converter that controls the gate signals. The intention is to implement torque and speed control in CRIO but due to problem with delays in the communication time, the machine is controlled by setting current references only. Hence no higher level of control such as MTPA or field weakening is implemented other than manually during the testing.

A picture of the test rig can be seen in Figure 5.18 with the flywheel in the lower left corner. The prop shaft is resting to the floor leaving the companion flange on the gearbox in the middle of the picture unattached. The horizontal black cylinder at the top of the picture is the air intake and the exhaust gases are evacuated to the ventilation system through the chimney to the left of the air intake. The ICE is seen in green underneath the air intake. The small picture focuses on the gearbox, PTO gear drive and EM, seen as the cylinder in the far right side of the picture. The numerous black hoses are for lubricating and cooling of the prototype PTO gear drive and for cooling of the electric machine. The oil supply to the EM is done with two hoses connected according to the two concepts described earlier in Figure 3.14 and Figure 3.16.

[8] http://www.ni.com/compactrio

Figure 5.18 Test facility for the system testing with the gearbox, gear drive and electric machine focused in the inset picture

System test result

All test results from the system testing is recorded with the control system since no external measurement equipment is available. Torque is estimated based on the EM rotational speed and electric power, calculated from the current and voltage vectors in the xy- or dq- plane. The intention with the torque estimation is not to achieve an accurate torque reading but rather to get a rough estimation on the EM operation point. Therefore the efficiency is disregarded in the transformation from electric to mechanical power. The temperature in the EM is recorded with the internal temperature sensors described earlier in Figure 4.5. This makes it possible to determine when thermal equilibrium is reached. An indication of the oil temperature is obtained via a temperature sensor in the gearbox oil sump. This temperature is read visually from the separate gearbox control program and manually added to the test data after the test. The applied current during one of the system tests is presented in Figure 5.19. The limit set in the control code can be seen as the radius of the arc shaped by the current readings.

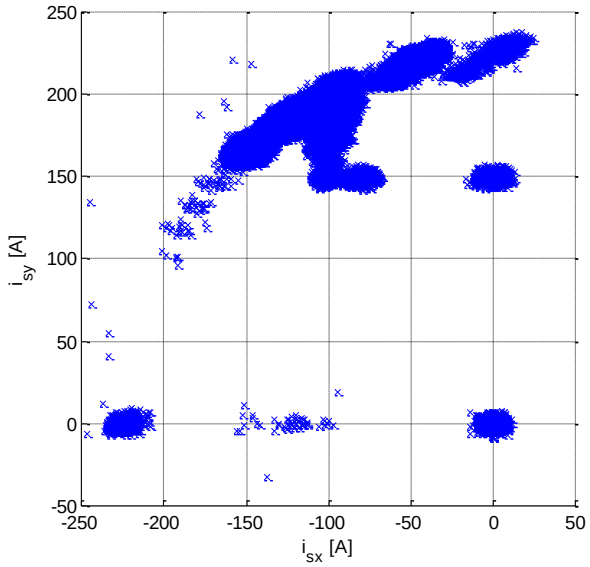

Figure 5.19 Applied current during one test sequence of the system testing, limited in the control code

Power, speed, corresponding torque and EM temperatures from the test are presented in Figure 5.20. The gearbox oil sump temperature during this test is around 80°C. This means that the oil inlet temperature into the EM is lower than 80°C due to the external cooler between the gearbox and the EM. The sudden leaps in the hotspot temperature sensor seem to be related to the switching in the drive, hence caused by electromagnetic interference. The power level of approximately 70 kW and the stable hotspot temperature during almost 10 minutes indicate that thermal equilibrium is reached. It is also observed that the hotspot temperature has a rather large margin to being overheated. This means that a higher continuous power, reaching the 80 kW stated in the requirements is expected to be reached. Due to limitations in controlling the mechanical load (exhaust brake on/off) no tests are performed to verify this.

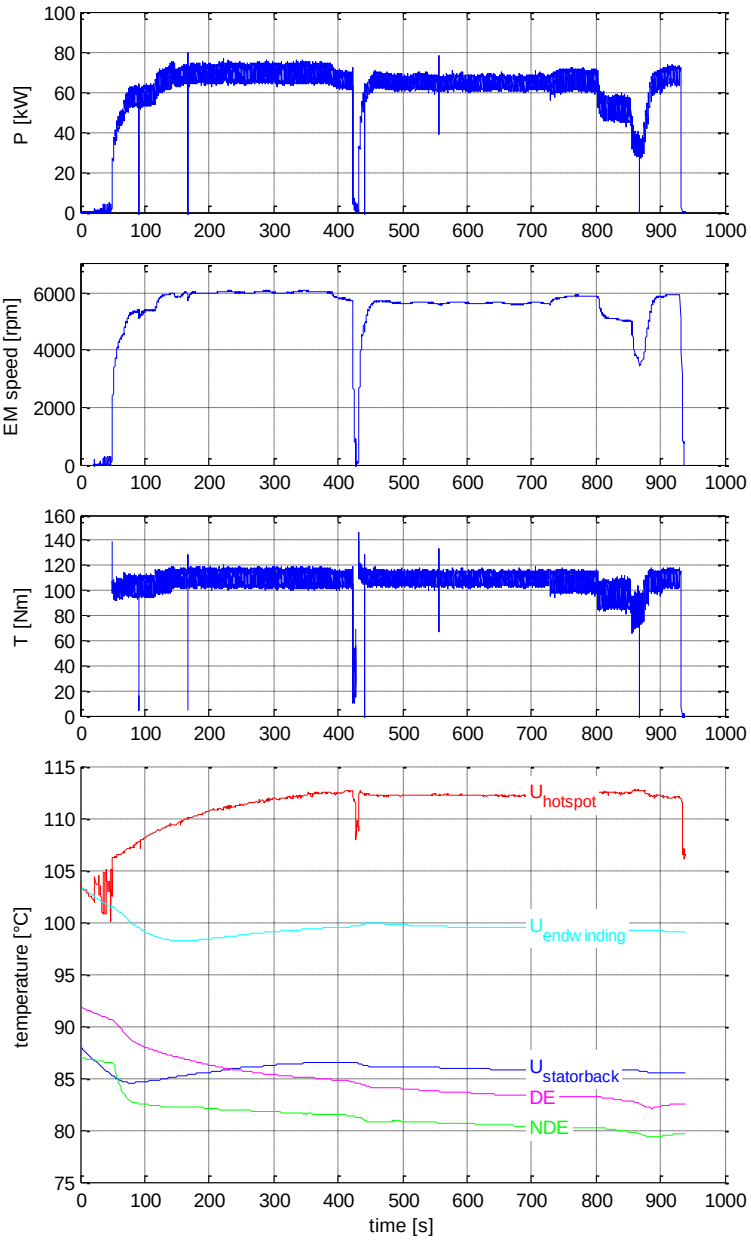

Figure 5.20 Electric power, EM speed, EM torque and temperature readings from the EM during one test sequence of the system testing

Torques from all measurements in the system test are recorded and used to create a torque map similar to Figure 5.10. This is presented in Figure 5.21. As can be seen, the result correlates rather well with the simulations up to around half the applied current in the lower right corner. In the lower left corner with high i_{sx} currents, torque is produced despite i_{sy} set to zero. This indicates an offset in the resolver angle. The measured torque map should therefore be rotated somewhat to coincide better with the actual result. At higher currents the measured torque is somewhat lower than the simulation result. This is to some extent caused by the method with which the torque is extracted from the speed and electric power, hence current and voltage. At higher currents the current ripple is escalating which results in less accurate torque estimation. Another aspect is the temperature difference in different parts of the torque map. The temperature is typically higher at higher currents, which affects the result slightly. Finally the measurements are done with oil cooling. This means that oil is present in the rotor department which might affect the torque slightly. Due to the limitations in the test rig and equipment this is not further investigated.

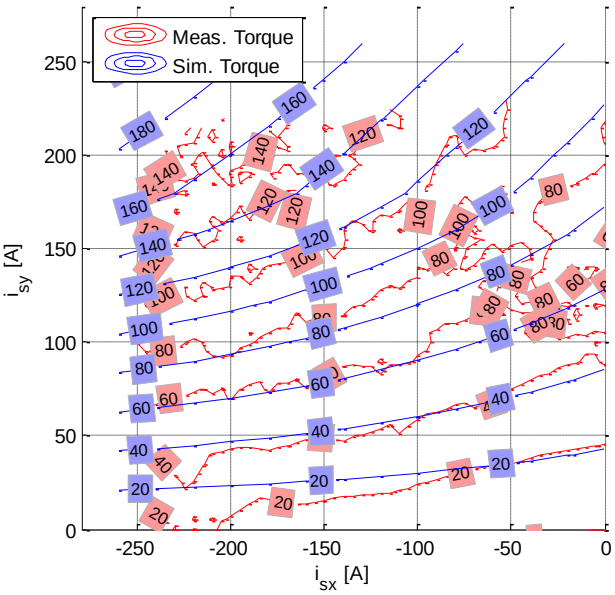

Figure 5.21 Torque extracted by EM speed and electric power during the system testing compared to torque from the simulations

Utilization of the EM for aiding synchronization of the gearbox during gearshifts is studied separately in a master thesis project and presented in [30]. The outcome is that a considerably higher deceleration rate is reached compared to the conventional countershaft brake. The requirement on the countershaft brake is to handle up to 2000 rpm/s. When using the EM instead, a deceleration rate of more than 3300 rpm/s is reached.

5.4 Experiences from the measurements

The different machine tests performed prove the importance of performing tests not only in securing the simulation model, but also in obtaining a good understanding of an EM. Many experiences during the testing have helped improving the overall knowledge in electric machine design, control and general behaviour.

The system testing described in section 5.3 ended with a bang. Due to problems with the communication time the speed control did not seem to work. When finally introducing compensation for this in the control, the field weakening current was forgotten. As the frequency converter tried to protect itself by compensating for this, the control freaked out resulting in four out of six half bridges and a set of capacitances burned out together with an unintended over speed test in excess of 28000 rpm. Although not recommended, a bang is a solid insurance for *never* forgetting the importance of field weakening.

In the following investigations on the electric machine the induced voltage seemed somewhat lower than in early measurements when the machine was new. As the log file from the fault case indicated extremely high field weakening currents, the possibility of partly demagnetized magnets have been investigated. By replicating the fault currents in FEMM, the field strength in the magnets is studied in Figure 5.22. In consultation with the PM manufacturer[9] the possibility of locally demagnetized magnets is investigated. New simulations with demagnetized regions according to Figure 5.23 are performed. This indeed resulted in lower induced voltage. However, when evaluating the measurements two different oscilloscope have been used before (Tektronix) and after (Yokogawa) the fault case. To eliminate the effect of this, a final set of induced voltage measurements is performed with the two different oscilloscopes at the same occasion. The result is presented as rms flux linkage in Figure 5.24. The outcome is that the difference is related to the accuracy in the oscilloscopes rather than

[9] Weickhmann, Michael, (Vacuumschmelze GmbH & Co. KG)

damaged magnets. This proves the importance of having reliable equipment with well-defined accuracy. It is also preferable to use the same measuring equipment when performing the measurements.

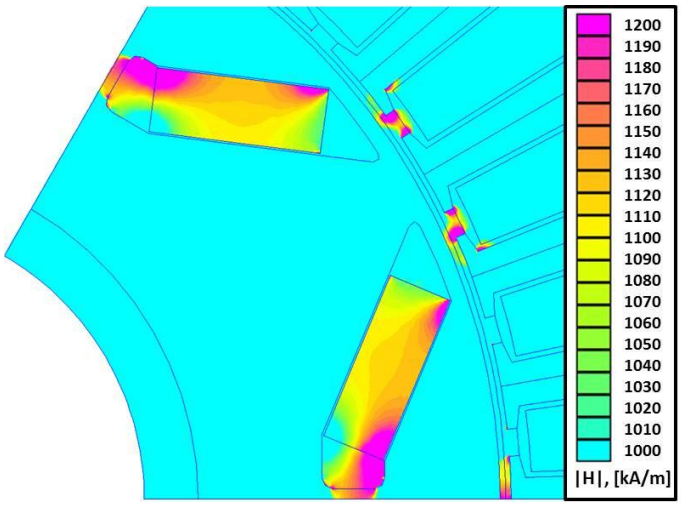

Figure 5.22 Magnetic field strength during fault case

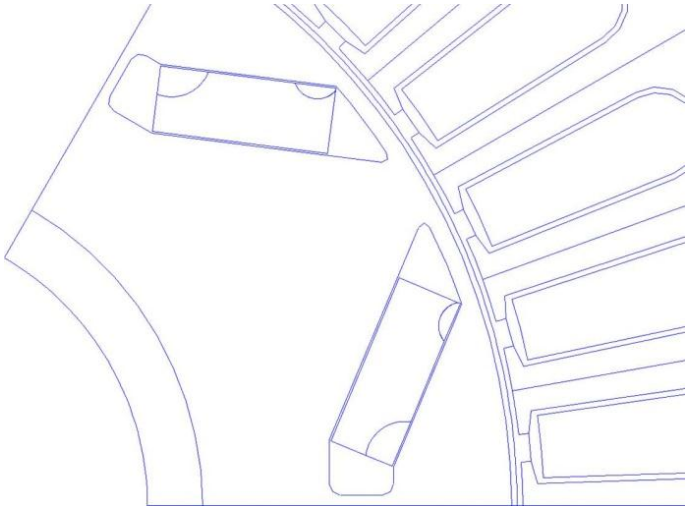

Figure 5.23 Locally de-magnetized regions in the magnets

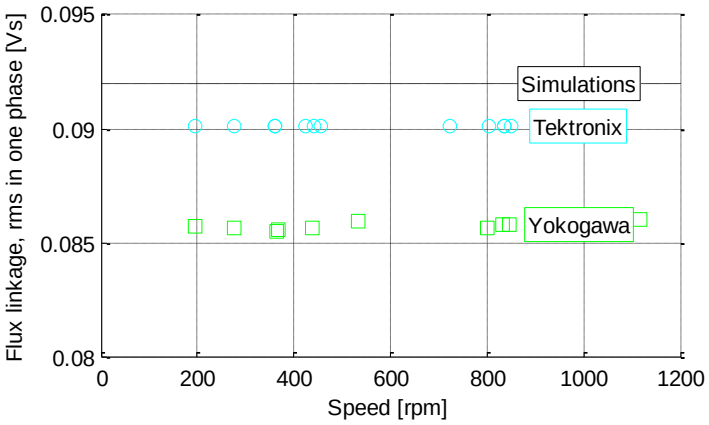

Figure 5.24 Flux linkage based on induced voltage measurements with different oscilloscopes

The thermal measurements described in section 5.1 first resulted in a deviation in temperature dependence from the simulation results compared to the measurements. The attempts to explain the difference included the previously mentioned demagnetization theory. After thoroughly investigating the validity of the measurements and the theory behind the simulation model, a fault was discovered in the model. Rather than keeping the permeability constant as discussed around Figure 3.11 in section 3.4, the reversible temperature coefficient of H_{cI} had been used on H_{cB}. This proves the importance of always validating the models with measurements. After all, the models try to replicate reality, while measurements show the fact. At least as long as the accuracy of the measurement equipment is decent enough.

Chapter 6

Conclusions

6.1 Conclusions

The main project goal is to make a design of a PMSM traction machine according to specifications for a heavy commercial vehicle, and in doing the related design work, educating the author to the level of Licentiate of Technology in the field of electrical machine design.

The prototype meets the design goal and is during testing able to provide a continuous tractive torque of around 110 Nm at a speed of 6000 rpm, hence around 70 kW. This is achieved under the intended cooling conditions, using transmission oil from the gearbox. The oil temperature in the gearbox during the measurement is at normal operating temperature, around 80°C and the flow rate is approximated to around 15 l/min. Limitations in the test rig prevents the machine from being tested in the entire intended torque and power range. However, the match between simulations and the performed measurements is considered sufficient to conclude that the specifications of requirements are fulfilled based on the simulation results. Altogether this gives a machine design with a peak power to weight ratio of 2.7 kW/kg which is comparable to, or higher than many of the competing machines intended for similar applications.

System design in deciding where in the drive train, from the ICE to the wheels, to connect the intended traction machine is performed. In the context of the traction system studied, the so called PTO-port on the transmission is selected as the connection point of the machine. This is based on the conclusion that a possibility to introduce a gear ratio from the machine to the PTO, minimizes the traction machine size. It is also possible to use part of the existing gearbox to shift gear to the electric

machine which can be beneficial when recuperating brake energy. A suitable gear ratio in the PTO mounted gear is determined to 6:1.

One conclusion from the work performed is that the specifications on the EM can vary rather much depending on the location in the vehicle. A position where no speed reduction is possible will impose different torque and speed demands and thereby probably a different machine design compared to what is presented in this thesis. Also the geometrical aspects can vary rather much. When mounted side parallel to the gearbox as suggested in this thesis, the outer diameter is crucial, while the total length is less of a concern. This opens for the possibility to implement distributed windings acquiring more space, despite the otherwise strict limitations in machine size. Since the machine is cooled using transmission oil applied to the end windings, the longer extrusion could instead be seen as an advantage. The larger end winding means larger area to cool which should impose a more efficient cooling.

Aspects of importance when designing an electric traction machine found during the writing of this thesis are:

- The dedicated space claim for the machine, both in terms of total volume, but also in terms of the total maximum length and diameter. Two different shapes sharing the same size in absolute volume gives completely different aspects of importance for the machine designer to consider. A long and slender design with smaller rotor diameter can possibly operate at a higher rotational speed without challenging the limits of a too high peripheral speed. A shorter total length could instead reach higher torque, but suffer from large end windings. The optimal machine design is therefore highly dependent on the implementation in the vehicle. Something that makes it hard to do fair comparisons between different machine types.

- Torque speed and power expectations on the machine and also how the different requirements are weighted against each other. Almost every aspect in an electric machine design is a trade-off between different pros and cons. In the machine design presented in this thesis, a lot of effort is put on reaching the desired peak power without saturating the stator back. To achieve this, less effort is directed towards fulfilling the continuous power requirement. It is desired to minimize the torque ripple, which is achieved to the expense of a small reduction in torque and a

potentially more complex winding process.

- A good knowledge in the adjacent areas and components in the drivetrain is also important in order to find an optimal design. This goes for the electrical as well as the mechanical point of view. The fundamental frequency of the machine must be handled by the switching frequency in the drive. A higher switching frequency might reduce the iron losses in the machine, but increase the total amount of losses in the system and so on. On the mechanical side, limitations imposed by bearings or gear steps are equally important to consider, preferably already when working with the machine design.

- Unless the machine designer is very experienced in building machines, a close cooperation with the machine manufacturer is recommended. Both in terms of what is possible to implement and also in how different manufacturing tolerances affects the machine design. A machine design performing slightly better can instead suffer from a more complex manufacturing process. One example is the slot fill factor. If the increased performance of a higher fill factor comes with an additional hour at the manufacturing line, it might not be worth it. This means that the designer again often faces a series of trade-offs, in this case between an optimal design and the manufacturability.

Finally, at least during the learning phase, it is concluded that lots of knowledge is lost if the associated prototype testing not can be done. This makes the participation in the verifying machine tests especially important. It is also considered beneficial if the designer can have the possibility to participate in the prototype build to better understand the connection between the simulation environment and reality.

6.2 Reflections

A lot of experience in electric machine design and difficulties with performing accurate tests are obtained along the way. A very useful experience is a week spent by the author at the machine manufacturer. When working in a computer based design tool, the grip of reality is easily lost. Therefore, the pieces of iron and copper in the prototype build are invaluable in terms of building understanding of an electric machine.

The fact that the requirements at the project start was rather vague imposed

a number of pre studies all very valuable in terms of gaining knowledge and understanding on the adjacent components. This embraces packaging space and interfaces, cooling media properties, transmission ratios, bearing requirements etc. In order to evaluate the different motor locations in the drivetrain, a good understanding is required in the possibilities and limitations of mechanical gear drives.

The majority of the work on implementing the machine control in the project is performed by others. Nevertheless, due to the problems with the time delay during the system testing much time is spent on getting the control up and running. The meaning of MTPA and field weakening and why and how to implement it, is understood and applied. The declining voltage ellipses with increased speed and how it affects the control at high speed and power and why this makes MFPT necessary are also made clear.

The effect of different temperatures in the machine is investigated. The reduced performance with increased temperature indicates the importance and benefits of efficient cooling. In combination with keeping the complexity in the vehicle at a minimum, the direct cooling approach seems to be a suitable solution. The limited experiences from the system testing described in section 5.3 indicate it to be an efficient cooling method. This must be more thoroughly investigated before a final conclusion is drawn. Also the need for a feed pump as well as a drain pump in the system test setup needs to be considered. A large benefit would be if the drain pump is replaced by gravity drain back to the gearbox sump. An even neater solution would be to feed the oil with the existing mechanical pump in the gearbox. This would require a thorough investigation as this makes the oil flow rate speed dependent. While the gearbox losses are speed dependent, lots of losses can occur also at low speeds in an electric machine. Another aspect is the temperature reduction obtained during standstill with an electric pump. This might make it possible to increase the torque and power output during the remaining operation time.

The difference in how the machine is used and setting the requirements in a vehicle compared to conventional industrial applications is realized. Different background for the machine manufacturer and the vehicle manufacturer makes the risk of misunderstanding imminent. For example the definition of peak operation as this is a more or less continuous operating point for the conventional combustion engine. In an electric machine it is highly dependent on the time at which the peak is required. Also in terms of packaging, the demands can differ rather much. The most efficient and cheap machine is still rendered useless if it is too large for the

intended application. In the strictly limited space in a vehicle this is made clearer than ever.

The simulation model gains further validation as the expectations from the design work agrees well with the test result performed. Also the dynamic test method is further evaluated in the backwash of the project. The match between measurements and simulations is considered very good. The importance of planning prior a test and the analysis done afterwards is also made obvious throughout the project.

6.3 Future work

The major part of future work is related to further testing of the prototype machine. This includes implementing power electronics with the suggested MTPA, field weakening and MFPT control methods. This is needed to verify the torque speed map generated in the simulation model (Figure 3.33). The continuous power level needs to be further investigated with better control of the oil flow rate and inlet/outlet temperature. The machine is intended for vehicle operation where cold starts are an option. As the viscosity of oil is highly dependent of temperature, cold starts might result in a too high back pressure preventing the oil from circulating in the machine. This could paradoxically lead to overheating the machine when operating in too cold ambient temperatures.

Related to the oil cooling circuit is also to establish whether oil in close connection to the airgap influences the no load losses. This is obtained with comparing measurements with and without connecting the oil cooling. The distribution of heat dissipation through oil spray on the end windings and the channels in the stator back also needs to be established. This would open for a possibility to develop a cooling model able to predict the heat dissipation via the oil spray. That would allow for a more precise temperature prediction when designing the machine, e.g., less safety factors when choosing magnet rating and winding insulation class. Since the two oil cooling circuits are connected separately it is possible to run tests on the two systems individually.

Measuring the power losses and efficiency is interesting both in terms of evaluating the machine design but also in order to improve the loss model. Especially when operating at high rotational speed, wind and roll resistance contributes to a substantial part of the losses. This makes it worthwhile to implement such a loss model in the simulation procedure. It should also be investigated whether rotor losses should be included in the

loss model. This is perhaps more relevant in designs with surface mounted magnets.

A continuation in the investigation of temperature dependence would be to carry out load tests at different temperatures. The dynamic loading procedure opens for a possibility to completely map the machine without affecting the machine temperature too much. The temperature difference in the winding hot spot sensor is for example 17°C during the test sequence described earlier in section 5.2 while the stator back temperature sensor differs less than 10°C. This despite disconnected cooling during the test. The magnet temperature is therefore considered rather constant within less than approximately 10°C temperature increase throughout a test sequence. By preheating the machine the test could be commenced at a number of different magnet temperatures. Another improvement in the post-processing code is to look at the temperature increase in the different sensors during a single acceleration.

The deviation in flux between simulations and measurements must also be further investigated. A proposed action is to look further into how the end winding inductance influences the result. Also thermal effects and how the reduction in remanence and coercivity influences the stator flux linkage in the machine should be investigated. The simulation tool might have to be reviewed in terms of how the parameters for the different materials are implemented. This goes especially for the magnets, but also for how the stator iron behaves at increased flux densities. The simulation tool is already considering saturation due to the flux density in the iron core, but this can perhaps be fin tuned even further. Also the consequence of a slight deviation in the resolver angle can be further investigated. The accuracy when determining the voltages and how it affects determining the flux might also be an aspect worth to consider.

Another interesting investigation not yet performed would be to evaluate the scalability of the design. The torque and thereby power level could rather easily be reduced by reducing the active length of the machine. If the power level instead should become higher in the future, a more thorough investigation would have to be performed. The length versus diameter ratio in the rather long and slender machine is already on the limit of what is conventional to work with when for example winding the machine. This limits the possibility to scale up the machine by just increasing the length. Instead the diameter would have to be increased, something considered more complicated. A larger diameter would for example mean higher peripheral speed on the rotor surface, hence tougher

demands on the mechanical strength. This could potentially lead to higher flux leakage etc. all needed to be investigated and evaluated. An alternative way of increasing the power could be to do re-wind the machine for an increase DC-voltage range. This would on the other hand affect a number of other components in the drive train.

Abbreviations

2D	Two dimensional
3D	Three dimensional
ac	Alternating current
AMT	Automated Manual Transmission
AP	Axial field die pressed
CoG	Centre of Gravity
CPSR	Constant Power Speed Range
CRIO	Compact Reconfigurable Input/Output
dc	Direct current
DE	Driving End
EM	Electric Machine
Emf	Electro-motive force
FE	Finite Element
FEA	Finite Element Analysis
FW	Field Weakening
HEV	Hybrid Electric Vehicle
HR	High Range gear
HS	High Split gear
ICE	Internal Combustion Engine

IEA	Div. Industrial Electrical Engineering and Automation
IPM	Internal Permanent Magnets
LR	Low Range gear
LS	Low Split gear
LTH	Lund Institute of Technology, Lund University
MFPT	Minimum Flux Per Torque
MTPA	Maximum Torque Per Amp
NDE	Non-Driving End
OD	Outer Diameter
PM	Permanent Magnet
PMSM	Permanent Magnet Synchronous Machine
PTO	Power Take Off
rms	Root mean square
rpm	Revolutions per minute
RTC	Reversible Temperature Coefficient
SAE	Society of Automotive Engineers
TP	Transvers field Die pressed
WEG	Water Ethylene Glycol

References

[1] Reinap, A., Hagstedt, D., Márquez, F., Loayza, Y., Alaküla, M., "Development of a radial flux machine design environment". *International Conference on Electrical Machines (ICEM2008)*, Vilamoura, Portugal, pp. 1-4, Sept. 6-9, 2008.

[2] Lipo, T.A., "Introduction to AC Machine Design", 4th edition, University of Wisconsin, Madison Wi, 2000.

[3] Miller, T.J.E., "Brushless Permanent-Magnet and Reluctance Motor Drives", Oxford : Clarendon, 1989, ISBN 0-19-859369-4.

[4] Harnefors, L., "Control of Variable-Speed Drives", Mälardalen University, Västerås, Sweden, 2002.

[5] Jonasson, K.., "Control of Hybrid Electric Vehicles with Diesel Engines". PhD thesis, Department of Industrial Electrical Engineering and Automation, Faculty of Engineering, Lund University (LTH), 2005.

[6] Alaküla, M., Johansson, K., Andersson, C., Simonsson, B. and Marksell, S., "Hybrid drive systems for vehicles, part 1". Course material, Department of Industrial Electrical Engineering and Automation, Faculty of Engineering, Lund University (LTH). Website accessed on 6th of October 2014. http://www.iea.lth.se/hfs/

[7] Huang, Z., Nategh, S., Lassila, V., Alaküla, M., Yuan, J., "Direct Oil Cooling of Traction Motor in Hybrid Drives", *IEEE International Electric Vehicle Conference (IEVC)*, Greensville, South Carolina, USA, pp. 1-8, March 4-8, 2012.

[8] Márquez-Fernández, F.J., "Electric traction machine design for an E-RWD unit". PhD thesis, Div. Industrial Electrical Engineering and Automation, Faculty of Engineering, Lund University (LTH), 2014.

[9] Soong, W.L., Miller, T.J.E., "Field-weakening performance of brushless synchronous AC motor drives", IEE Proc.-Electr. Power Appl., Vol. 141, pp. 331-340, No. 6, November 1994.

[10] Bianchi, N., Bolognani, S., “Unified Approach and Design of an AC Motor Drive for Flux-Weakening Operations”, *IEEE Industry Applications Conference*, Thirty-Third IAS Annual Meeting, pp. 95 - 102 vol.1., 1998.

[11] Vagati, A., Pellegrino, G., Guglielmi, P., “Comparison between SPM and IPM motor drives for EV application”, *International Conference on Electrical Machines (ICEM2010)*, Rome, Italy, pp. 1-6, Sept. 6-8, 2010.

[12] Andersson, R., Gillström, A., “Sensorless Control of a Permanent Magnet Synchronous Machine using Signal Injection” Master of Science Thesis, Chalmers University of Technology, TeknologTryck, Göteborg, Sweden, 2008.

[13] Buschow, K.H.J., "Concise Encyclopedia of Magnetic and Superconducting Materials", Second edition, University of Amsterdam, The Netherlands, 2005, ISBN: 978-0-08-044586-1

[14] Sundström, B., (ed), “Handbok och formelsamling i Hållfasthetslära” 7th edition, Instant book AB, Stockholm, Sweden, 2010.

[15] Saabye Ottosen, N., Ristinmaa, M., Ljung, C., ”Hållfasthetslära Allmänna tillstånd”, Pozkal, Poland, 2007, ISBN: 978-91-44-05032-4.

[16] Stone, G.C., Boulter, E.A., Culbert, I., Dhirani, H., “Electric Insulation for rotating machines, Design, Evaluation, Aging, Testing and Repair”; *IEEE Press; Wiley- Interscience, UISA*; ISBN 0-471-44506-1, Chapter 6.1.10.

[17] Krings, A., Mousavi, S.A., Wallmark, O., Soulard, J., “Temperature Influence of NiFe Steel Laminations on the Characteristics of Small Slotless Permanent Magnet Machines”; *IEEE Trans. Magn., vol 49, no. 7*, pp. 4064-4067, July 2013.

[18] Takahashi, N., Morishita, M., Miyagi, D., Nakano, M., “Comparison of Magnetic Properties of Magnetic Materials at High Temperature”; *IEEE Trans. Magn., vol 47, no. 10*, pp. 4352-4355, October 2011.

[19] Gieras, J.F., “Advancements in Electric Machines”. 2009. e-ISBN: 978-1-4020-9007-3.

[20] Hsu, J., Ayers, C., Coomer, C., “Thermal control for power electronics and motors”, Oak Ridge National Laboratory, FY 2006 progress report.

[21] German patent application DE 3120394 A1, 1982.

[22] Sundén, B., “Introduction to Heat Transfer”, Lund, Sweden, 2008, ISSN 0282-1990.

[23] Deodhar, R.P., Staton, D.A., Miller, T.J.E, ”Modelling of skew using the flux MMF diagram (of PM machines)”, *IEEE Transactions on Industry Applications*, pp. 1339-1347, Nov/DEC 1996.

[24] Loayza, Y., Reinap, A., Alaküla, M., “Performance and efficiency evaluation of FPGA controlled IPMSM under dynamic loading”. *8th IEEE International Symposium on Diagnostics for Electrical Machines, Power Electronics and Drives (SDEMPED)*, pp. 550-555, Bologna, Italy, September 5-8, 2011.

[25] Hall, S., Loayza-Vargas, Y., Reinap, A., Alaküla, M., “Consistency analysis of torque measurements performed on a PMSM using dynamic testing”. *International Conference on Electrical Machines (ICEM14)*, pp. 1523-1529, Berlin, Germany, 2-5 September, 2014.

[26] Marquez-Fernandez, F., Hall, S., Alaküla, M. (2014), “Dynamic Testing Characterization of a HEV Traction Motor”. *International Conference on Electrical Machines (ICEM14)*, pp. 1563-1569 Berlin, Germany, 2-5 September, 2014.

[27] Norling C, Österman J: “Physics Handbook for Science and Engineering”, 6th edition, Studentlitteratur, Lund, Sweden, 2002, ISBN: 91-44-00823-6.

[28] Kellner, S.L., Seilmeier, M., Piepenbrier, B., ”Impact of Iron Losses on Parameter Identification of Permanent Magnet Synchronous Machines”. *1st International Electric Drives Production Conference (EDPC)*, pp. 11-16, Nuremberg, Germany, Sept 28-29, 2011.

[29] Loayza, Y., PhD student at Div. Industrial Electrical Engineering and Automation, Faculty of Engineering, Lund University (LTH).

[30] Reinholds, M., Andreasson, S., “Dynamic gear shifting of an automated manual transmission”. Master of Science Thesis. Div. Industrial Electrical Engineering and Automation, Faculty of Engineering, Lund University (LTH), 2013. TEIE-5309.